João Paulo Perbiche
Head Organizer

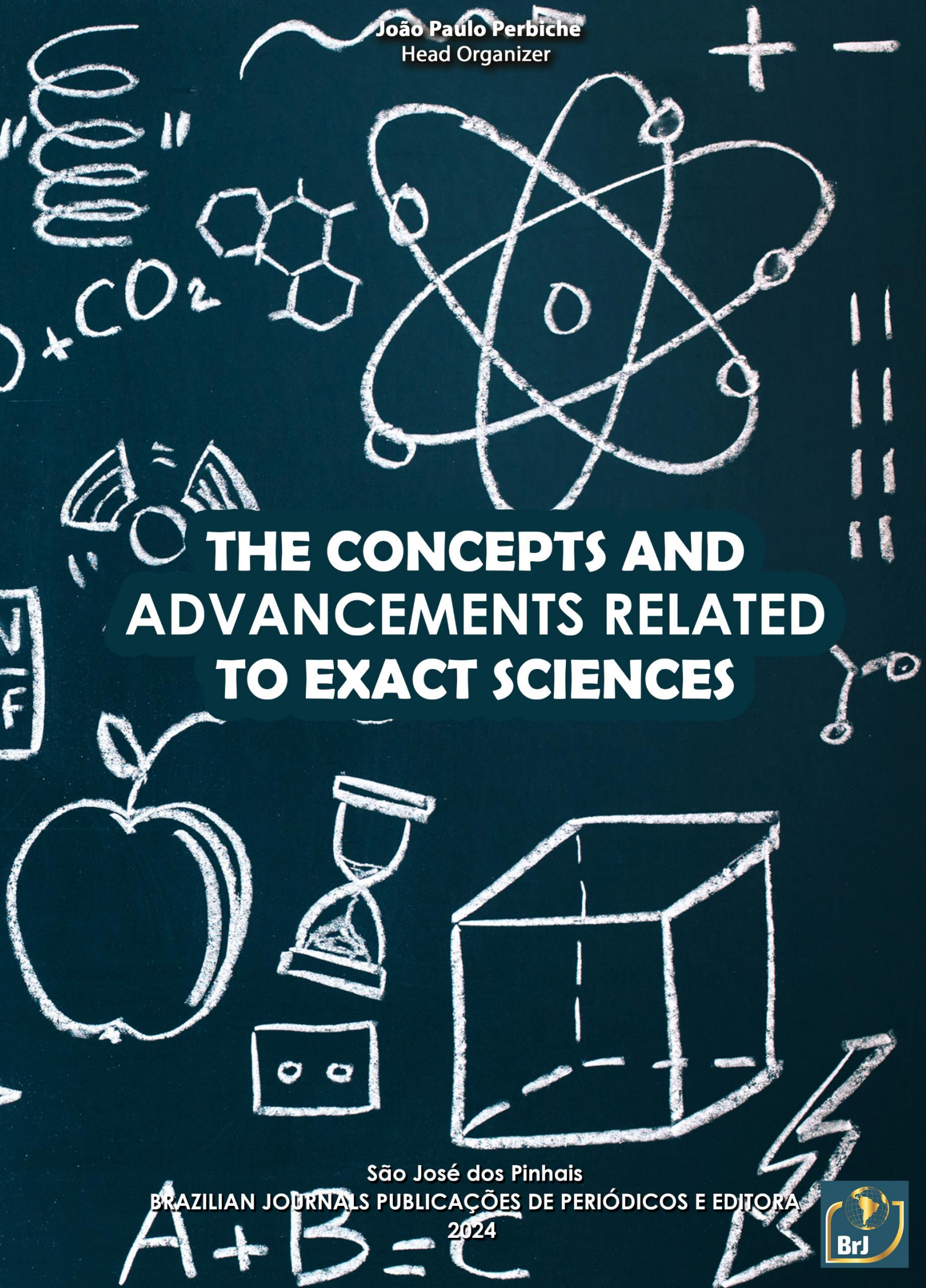

THE CONCEPTS AND ADVANCEMENTS RELATED TO EXACT SCIENCES

São José dos Pinhais
BRAZILIAN JOURNALS PUBLICAÇÕES DE PERIÓDICOS E EDITORA
2024

João Paulo Perbiche
Head Organizer

The concepts and advancements related to exact sciences

Brazilian Journals Editora
2024

Diagramação: Editora
Edição de Arte: Editora
Revisão: Os Autores

Editorial Board:

Dados Internacionais de Catalogação na Publicação (CIP)

P427c Perbiche, João Paulo

The concepts and advancements related to exact sciences / João Paulo Perbiche. São José dos Pinhais: Editora Brazilian Journals, 2024.

Formato: PDF
Requisitos de sistema: Adobe Acrobat Reader
Modo de acesso: World Wide Web
Inclui: Bibliografia
ISBN: 978-65-6016-072-9

1. Exatas. 2. Matemática.

Brazilian Journals Editora
São José dos Pinhais – Paraná – Brasil
www.brazilianjournals.com.br
editora@brazilianjournals.com.br

PRESENTATION

The Concepts and Advancements Related to Exact Sciences offers a deep dive into the fascinating universe of exact sciences, exploring the fundamental concepts that shape our understanding of the world and the recent advances that have transformed the frontiers of knowledge. In an era marked by rapid technological and scientific development, mastery of exact sciences is essential to understanding everything from the most basic phenomena to the complex innovations that directly impact our society.

In this work, the reader will find an accessible and comprehensive analysis of topics that encompass areas such as physics, chemistry, mathematics and astronomy. The book discusses both the classical concepts that underpin these disciplines and the cutting-edge discoveries and technologies that have revolutionized fields such as artificial intelligence, nanotechnology and space exploration. With an approach that balances scientific rigor and clarity, this reading is an invitation to explore the universe of natural laws that govern the cosmos and the intellectual tools that allow us to decipher them.

We recommend this book to anyone interested in scientific knowledge, whether they are professionals, students or just naturally curious. The Concepts and Advancements Related to Exact Sciences not only deepens our understanding of the principles that underpin science, but also highlights the practical implications of these discoveries for the future of humanity. Prepare for a journey that combines tradition and innovation, revealing how the exact sciences continue to expand our boundaries and open up new possibilities for understanding the world.

SUMMARY

DOI: 10.55905/edicon.978-65-6016-072-9_7

CHAPTER 1

EDUCATIONAL REFRIGERATION SYSTEM PROJECT FOR THE GENERATION OF AN ICE RINK: PART 1

Wertson da Silva Resende
Institution: Universidade Federal do Rio Grande do Norte (UFRN)
Address: Campus Universitário Lagoa Nova, Caixa Postal 1524, Natal, RN, Brasil, CEP 59078-900
E-mail: wertson.resende.012@ufrn.edu.br

Cleiton Rubens Formiga Barbosa
Universidade Federal do Rio Grande do Norte (UFRN)
Address: Campus Universitário Lagoa Nova, Caixa Postal 1524, Natal, RN, Brasil, CEP 59078-900
E-mail: cleiton.formiga@ufrn.br

Sandi Itamar Schafer de Souza
Institution: Universidade Federal do Rio Grande do Norte (UFRN)
Address: Campus Universitário Lagoa Nova, Caixa Postal 1524, Natal, RN, Brasil, CEP 59078-900
E-mail: sandi.souza@ufrn.br

Álvaro Augusto Soares Lima
Institution: Universidade Federal do Rio Grande do Norte (UFRN)
Address: Campus Universitário Lagoa Nova, Caixa Postal 1524, Natal, RN, Brasil, CEP 59078-900
E-mail: alvaro.augusto@ufrn.br

Cleiton Rubens Formiga Barbosa Júnior
Institution: Universidade Federal do Rio Grande do Norte (UFRN)
Address: Campus Universitário Lagoa Nova, Caixa Postal 1524, Natal, RN, Brasil, CEP 59078-900
E-mail: cleitonformiga@gmail.com

Ângelo Roncalli Oliveira Guerra
Institution: Universidade Federal do Rio Grande do Norte (UFRN)
Address: Campus Universitário Lagoa Nova, Caixa Postal 1524, Natal, RN, Brasil, CEP 59078-900
E-mail: angelo.roncalli@ufrn.br

ABSTRACT: Among the refrigeration cycles most frequently discussed in the literature and studied in courses related to Thermal Systems in mechanical engineering are the simple vapor compression refrigeration cycles. These systems have numerous applications in homes, businesses, and industries, and beyond the most common uses, their application in *ice rinks* draws attention due to the diverse possibilities for

knowledge application and technique implementation concerning the production of “cold.” Ice rinks are primarily designed for sporting activities such as figure skating, hockey, speed skating, and other *indoor* activities like recreational skating. This work is divided into two parts: the first aims to develop the heat exchanger sizing calculations – specifically, the evaporator of the system – for the construction of a small-scale ice rink for educational purposes within the mechanical engineering program at UFRN. It includes brief fundamentals associated with each component of the system. The starting point is the simple vapor compression refrigeration cycle with direct expansion and its controls, with the initial capacity defined by a ¼ HP commercial condensing unit available in the laboratory. The final result of this part includes the definition of the construction parameters for the heat exchanger – the coil used to generate the rink, and in the second part, we will define the models of the selected components to complete the entire system of this ice rink.

KEYWORDS: Design, Sizing, Refrigeration System, Ice Rink, Didactic.

RESUMO: Dentre os ciclos de refrigeração mais abordados nas bibliografias e estudados ao longo das disciplinas relacionadas a Sistemas Térmicos na engenharia mecânica estão os ciclos de refrigeração a compressão de vapor simples. São inúmeras as aplicações destes sistemas em residências, comércios e indústrias, e além das mais comuns, a sua aplicação em pistas de gelo – *Ice-rinks* – chama a atenção pelas diferentes possibilidades de abordagem de conhecimentos e implementação de técnicas no que diz respeito à produção do “frio”. As pistas de gelo destinam-se basicamente à realização de atividades esportivas, tais como: patinação artística, hóquei, corridas sobre patins e outras atividades *indoor* como a pura e simples patinação recreativa. Este trabalho está dividido em duas partes: a primeira tem como objetivo geral desenvolver cálculos de dimensionamento do trocador de calor – Evaporador do sistema - para construção de uma pista de gelo em escala reduzida para fins didáticos no âmbito da engenharia mecânica da UFRN. Nele encontramos breves fundamentos associados a cada componente do sistema. O ponto de partida é o ciclo de refrigeração a compressão de vapor simples com expansão direta e seus controles, cuja capacidade inicial foi delimitada pelo modelo de unidade condensadora de ¼ HP comercial disponível no laboratório. Como resultado final, neste, apresentamos a definição dos parâmetros construtivos para o trocador de calor – serpentina geradora da pista, e na segunda parte, definiremos os modelos dos componentes selecionados para composição de todo o sistema desta pista de gelo.

PALAVRAS-CHAVE: Projeto, Dimensionamento, Sistema de Refrigeração, Pista de Gelo, Didático.

1. INTRODUCTION

According to ASHRAE (2014), ice rinks are considered any leveled layers of ice generated by refrigeration systems, primarily intended for sporting activities such as figure skating, hockey, speed skating, acrobatics, and others, as well as simple recreational skating. These activities can take place in outdoor environments, exposed to the weather, or in enclosed spaces such as arenas, auditoriums, coliseums, and, more commonly nowadays, shopping centers.

These artificial rinks, generated through refrigeration, emerged precisely from the need to perform the listed activities in various locations, regardless of ambient temperatures or the season of the year. This development made it possible to skate in any external temperature, not only in regions with temperatures well below freezing and naturally frozen rivers and/or lakes.

The first recorded artificial ice rink was set up at the end of the 19th century in London, England. This record is found in Littell's Living Age, published in 1844. Referring to an ice rink built that same year in the then-called "The Glaciarium," it stated: "The artificial ice area is extremely convenient for those who wish to engage in the graceful and manly pastime of skating." This artificial ice rink, considered innovative at the time, quickly became a popular attraction, and since then, the popularity of artificial ice rinks worldwide has grown significantly.

1.1 THE PHENOMENA INVOLVING SKATING

Friction is often considered a negative force due to its resistance to motion, however, in ice skating, it plays a crucial role. The frictional force between the skate blade and the ice allows the skater to start, maintain, or stop their movement: the skater transfers body weight to one foot while pushing the other foot backward and outward, using the inner or outer edge of the skate blade. This initial thrust is important for accelerating the body and initiating the glide. Once the initial thrust is given, the skater glides across the ice surface and must distribute their weight evenly between both legs and keep the center of gravity low to maintain balance. While gliding, the skater alternates between pushing and sliding. This is done by pushing with the back foot and then moving the foot forward to slide across the ice. The correct propulsion technique

can vary depending on the skating style (e.g., figure skating, speed skating). Skaters use the inner and outer edges of their blades to control direction and stability and tilt their bodies inwards or outwards, allowing the blade edge to make contact with the ice, which is essential for maneuvering and performing specific moves. In addition to basic gliding, skaters can perform a variety of movements and maneuvers, such as turns, spins, jumps, and twists. Each of these movements requires a specific combination of propulsion techniques, balance, and edge control.

Overall, the interaction between the skate blades and the ice involves a series of complex physical processes, including localized melting, recrystallization, formation of melted ice, and reduced friction. The behavior of water under these conditions is crucial, as it allows movement during skating. It is known that at temperatures below -29°C, water tends to freeze almost instantaneously. The idea of having liquid water at negative temperatures is not always accepted by everyone. However, in particular cases like that of water, the pressure effect is inversely proportional to the melting point; that is, the higher the pressure applied to it, the lower the melting point, and therefore, water can more easily transition from a solid to a liquid state. This means that liquid water can be found below 0°C and at the temperatures of the rink.

For this process to occur, it is crucial that the ice temperature on the rink is sufficiently low and uniform to allow the melting to be adequate for gliding without causing cracks or the formation of pockets of liquid water across the entire surface of the rink.

1.2 THE PHENOMENA INVOLVING SKATING

Among the refrigeration cycles most frequently covered in the literature and studied throughout the Thermal Systems courses in the undergraduate mechanical engineering program are the simple vapor compression cycles. These systems have numerous applications in residences, businesses, and industries. Aside from the more common uses, the application in the construction of ice rinks represents a significant opportunity to demonstrate and address various topics and knowledge, with the implementation of techniques related to the development of "cold". The freezing of the water forming the rink is typically achieved by a fluid that absorbs heat from the water through its circulation in a network of pipes located beneath the surface on which the

ice rests. This fluid is predominantly a secondary refrigerant, such as glycol, methanol, or calcium chloride. However, it is also possible to construct rinks using a simple vapor compression refrigeration system without a secondary fluid, meaning with direct expansion in the network of pipes, and consequently, direct heat exchange between the refrigerant fluid of the system and the structure forming the rink.

Figure 1. Condenser unit, model TCM2020E

Source: Authors

The design of this ice rink (for educational purposes) is exclusively intended to provide practical experience with the study of such a system - specifically, a simple vapor compression refrigeration cycle with direct expansion - and its controls for a small-scale ice rink, with subsequent use of the equipment in the Energy Laboratory classes of the Department of Mechanical Engineering at UFRN. The first part of this work aims to present the development of heat exchanger sizing calculations, while the second part focuses on the selection of ancillary components along with the specifications for construction, assembly, and start-up of the small-scale rink. Furthermore, each step will include a brief explanation of the components of the refrigeration circuit, with the initial capacity defined by the condenser unit model available in the laboratory, TCM 2020E from Elgin, with a commercial reference of 1/4HP, as shown in Figure 1.

It is anticipated that specific topics and issues may be later addressed through practical exercises in sizing, component selection, field measurements, and comparisons of the equipment after its assembly and start-up, such as: fundamental concepts of heat transfer by conduction; overall heat transfer coefficients; applications of the heat equation, Newton’s Law, in solving temperature fields and heat transfer

rates in one-dimensional steady-state problems; refrigeration fundamentals; refrigeration cycles and circuits; refrigeration plants; refrigeration equipment; refrigerants; thermal load calculations; among others.

2. BASIC COMPONENTS OF THE SYSTEM

After the heat exchanger has been sized, the basic components that will make up the system will be selected in Part 2. Below, we describe some of the main characteristics of these components, with the aim of consolidating their specific functions and important aspects in the selection process.

2.1 CONDENSING UNIT

The condensing unit is composed of a compressor, condenser, liquid receiver, service valves, condenser, and their interconnecting piping.

The compressor in the refrigeration system is responsible for drawing in the gaseous refrigerant at low pressure from the evaporator and compressing it to the high pressure required for discharge into the condenser.

The unit employs a hermetic reciprocating compressor, which is enclosed or hermetically sealed. The compression mechanism is directly coupled with the electric motor, both enclosed in a welded factory casing that does not allow internal maintenance access. In these compressors, the refrigerant comes into direct contact with both the electric motor and the compression mechanism. If any failure or internal damage occurs in either the electrical or mechanical parts, they cannot be accessed without cutting open the casing. Manufacturers typically recommend a complete replacement in such cases. Reciprocating compressors operate by moving the refrigerant volume through pistons that work in conjunction with a connecting rod and the motor’s crankshaft.

As presented by Costa (1982), the condenser is the component in the refrigeration circuit where the refrigerant, in the gaseous phase at high temperature and pressure, is condensed into a liquid by releasing the heat removed from the process in the evaporator, suction line, and added by the compression work, through the surface of its coil to the surrounding air. In commercial segments, it is generally a

heat exchanger made of a thin-walled copper coil combined with aluminum fins, housed in a painted or unpainted steel casing, where the air blowers (fans) are commonly mounted and operated in parallel with the compressor.

A liquid receiver or tank is a simple device used to store the liquid refrigerant in a refrigeration system. Its function is to accommodate fluctuations in refrigerant flow due to varying thermal loads, absorb some of the vibrations from the reciprocating compression process, drain refrigerant freely from the condenser, allow for a refrigerant return method for controlling discharge pressure, and provide partial refrigerant storage during extended periods of shutdown.

Service valves, in addition to allowing or blocking fluid flow, also provide access for measurement instruments to the system's internal pressures during operation. They also facilitate various start-up and commissioning procedures, such as flowing nitrogen through the piping during brazing processes, performing leak tests, evacuation and dehydration, and refrigerant charging.

2.2 DRYER FILTER

The drier filter combines the functions of filtering out solid impurities and moisture that may be present in the refrigerant. It is designed to protect expansion devices (capillary tubes or expansion valves) and the compressor from foreign particles, such as construction and assembly debris, solder residues, oxidation, and metal shavings. The desiccant element retains any remaining moisture after the dehydration process, preventing it from circulating and degrading system components, including the lubricating oil.

2.3 LIQUID SIGHT GLASS

Sight glasses are used primarily to indicate the state of the refrigerant in the piping and to show the level of moisture in the system, as some models feature chemical indicators that change color in the presence of moisture. They guide the system maintenance technician during performance adjustments.

2.4 SOLENOID VALVE

Solenoid valves commonly used in commercial refrigeration are mostly either direct-acting or servo-operated. They are employed to block the flow of liquids, vapor, or hot gas in systems that use halogenated refrigerants. The valve consists of two basic parts: the body and the solenoid coil. The coil is made of wire wound around a cylindrical surface. When an electric current passes through the wire, it generates an electromagnetic force in the center of the coil, which moves a ferromagnetic plunger. This mechanical movement opens or closes the refrigerant passage, thereby opening or closing the valve.

2.5 EXPANSION DEVICE - THERMOSTATIC EXPANSION VALVE

It is well established in the literature (Wirz, 2011) that the most commonly used type of expansion device in medium-sized installations is the expansion valve controlled by superheat, known as the thermostatic expansion valve (TEV). The superheat expansion valve regulates the flow of liquid refrigerant entering the heat exchanger based on the evaporation rate. It is essentially composed of a sensing bulb, capillary tube, orifice, and valve body. The superheat action on the thermostatic expansion valve is achieved through the sensing bulb, which is partially filled with the same refrigerant liquid as in the system, known as the sensing fluid. This bulb is installed and fixed to the evaporator outlet pipe so that the temperature of the sensing fluid is close to the temperature of the suction gas at that point. Due to this superheat, the TEV will open or close, varying the mass flow rate into the heat exchanger, the system's evaporator.

In systems where the evaporator has a large heat exchange area with high pressure drop, if the TEV is of the internal equalization type, the pressure acting on the lower side of the diaphragm will be higher than that in the suction pipe at the bulb's mounting point. This condition requires a higher superheat for the valve to open, thereby reducing efficiency. To correct this discrepancy, an external equalizer is used. This consists of a small diameter tube connecting the system's suction line to a small chamber on the lower side of the diaphragm, allowing the suction pressure to act on

the lower surface of the diaphragm, "compensating" for the effects of the significant pressure drop.

2.6 COOLANT FLUID

The refrigerant fluid is the substance responsible for absorbing and rejecting heat as it vaporizes and condenses while circulating in the system. The most commonly used fluids for refrigeration in ice rink systems with secondary fluid circulation have long been ammonia (NH^3) and R22, although R12 and R502 were also frequently used. Due to the implementation of phase-out programs for CFCs and HCFCs (a class of fluids primarily composed of Hydrogen, Chlorine, Fluorine, and Carbon), which are harmful to the ozone layer and contribute to the greenhouse effect, these fluids are no longer recommended for use. In Brazil, in compliance with Decision XIX/6 of 2007 of the Montreal Protocol, the Brazilian Program for the Elimination of HCFCs (PBH) was established. This program outlines the strategy for controlling, reducing, and eliminating HCFCs, including R22. The program specifies that for new systems, the replacement of R22 and other fluids in this class should be evaluated based on their status and availability when the equipment is being designed.

3. DEVELOPING THE SYSTEM

Refrigeration systems for ice rinks are commonly applied in an indirect expansion configuration, which means they use a secondary fluid. However, for this project, we will use a direct expansion circuit for the refrigerant, with the prospect of a future design for a system with indirect expansion. In direct expansion systems, the refrigerant expands directly in the coil installed below the ice.

The advantage of a direct expansion application is the ability to achieve an even ice temperature without the need for a circulation pump, thus minimizing some losses and consequently providing greater energy efficiency compared to an indirect expansion system. The main disadvantages still include the cost of the refrigerant, which must be in sufficient quantity to fill the entire coil under the ice rink, as well as limitations related to the selection of the refrigerant according to PBH.

According to ASHRAE (2014), the estimated thermal load should consider common requirements for this type of system. Data from installations of various rinks with covered piping indicate that the most common configuration for the heat exchanger involves applying no more than approximately 25 mm (1 inch) of sand or concrete over it, and no more than approximately 38 mm (1.5 inches) of ice layer formed on top. This results in a block of up to 63 mm in height encompassing the refrigerated base and the ice surface (tubes and concrete, and ice block), as exemplified in Figure 1, below.

Figure 2. Example of ice-rink construction form (Adapted, ASHRAE:2014).

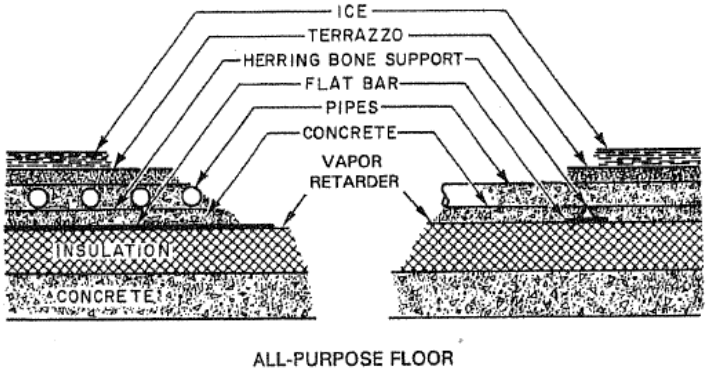

Source: ASHRAE, 2014.

It is often recommended to install vapor barriers, at least beneath the concrete layer, to prevent moisture transfer from the ground into the concrete in systems built directly on the floor. The material used beneath the rink floor should not have properties that facilitate the capillary transfer of moisture from the ground to the ice. If this happens, there is a risk that the moisture could reach the floor structure, causing damage to the structure.

This work will not focus on surrounding thermal load factors such as the type of use, duration of usage seasons, type of environment where it will be installed, radiant thermal loads from the roof and lights, as well as associated wet and dry bulb temperatures beyond the rink. These parameters will be limited due to the educational nature of the rink and its extremely reduced scale.

Thus, the thermal load can be estimated by: (1) calculating the amount of heat required to freeze the ice and bring it to the conservation temperature; (2) calculating the amount of heat needed to lower the temperature of the concrete to the process

temperatures; and (3) calculating the possible heat flow to the evaporator coil to achieve the surface temperatures suitable for the rink's nominal conditions.

Table 1. Condensing Unit Data

Manufacturer:	Elgin	**Rated Current:**	2.5A
Model:	TCM2020 E	**Consumption:**	480W=0.48kW (cosφ=0.87)
Fluid:	R22	**Commercial Reference:**	1/4HP
Power supply:	220VAC	**Application:**	MBP, de -15°C a 0°C
Frequency:	60Hz	**Refrigeration Capacities:**	430kcal/h@-15°C; 550kcal/h@-6.7°C; 780kcal/h@0°C

Source: Condensing Unit Data

To carry out the calculations, we started with the application data of the available condensing unit, table 1, and it is also worth reviewing and defining some important parameters, such as:

3.1 EVAPORATION TEMPERATURE

The lowest evaporation temperature for the range of application of the condensing unit will be applied, as it represents, according to catalogs and state of the art, the lowest corresponding cooling capacity of the unit, placing the system in the most severe operating condition considering the application range, MBP (Medium Back Pressure). Therefore, the evaporation temperature will be $T_{evaporation}$=-15°C which corresponds to a saturation pressure for R22 $P_{evaporation}$= 28.6psig= 42.96psia= 1.95bar G= 2.96bar ABS.

3.1.1 Condensation Temperature

Although the indicated condensing temperature for testing the machine is 55°C, which is a quite severe condition, we will use the local ambient temperature as specified by the ABNT NBR16401-1:2008 standard for the city of Natal/RN. The dry bulb temperature (TBS) indicated is 32.2°C for an annual frequency of 0.4%. Based on this, to define the condensing temperature, the temperature difference between the condensing temperature and the surrounding air is usually between 10 and 15K, with the most extreme condition being 15K. This leads us to consider an extreme

condensing temperature of 47.2°C, which corresponds to a saturation pressure for R22 in condensation of $P_{condensation}$ = 249.4psig = 264.1psia = 17.2bar G = 18.21bar ABS.

3.1.2 Degrees of Superheating and Subcooling

Considering that the test conditions for the condensing unit are severe, with superheating of 41.7K and subcooling of 9K being considered extremely high for medium commercial/industrial applications (with typical ranges being 11 up to 22K for total superheating and 4 up to 8K for subcooling), we will use the average values of these ranges for the project. Thus, we will adopt a system superheating of 16K and a subcooling of 6K.

3.2 CYRCLE OF REFRIGERATION BY VAPOR COMPRESSION SIMPLE

With the preliminary information, it is possible to plot the ideal refrigeration cycle, which will serve as the basis for the entire dimensioning and selection process using Coolpack Software. From this cycle, we can obtain various parameters that describe the cycle's behavior during ideal operation, allowing us to adjust the states of the fluid at the key points of the system.

Considering the simple vapor compression refrigeration cycle, single stage, we can generate the following states for the refrigerant R22 at each point indicated in the ideal cycle using Coolpack:

Figura 3. (a) Cycle on Pressure vs. Enthalpy Diagram, (b) Points on Simple Refrigeration Cycle.

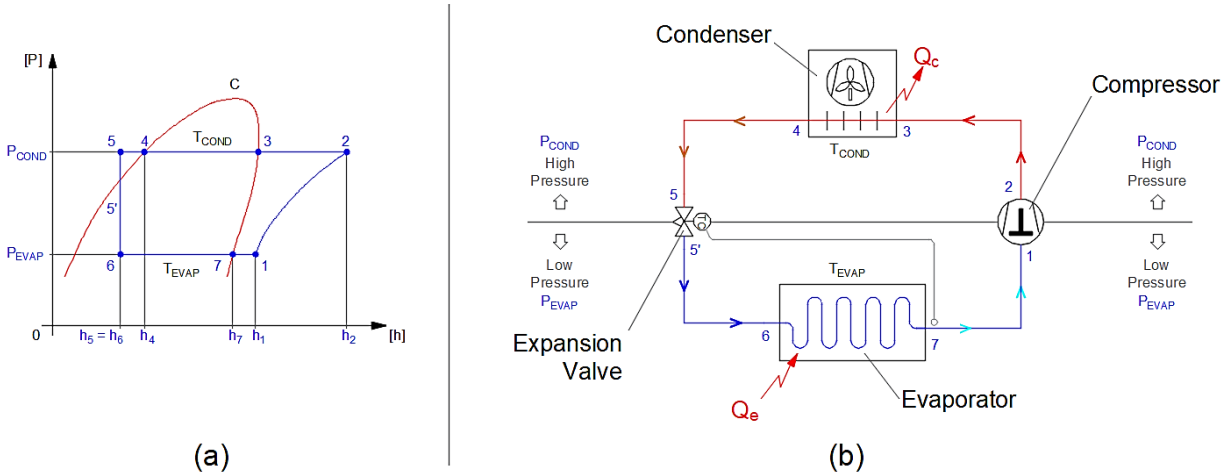

Source: Adapted, Costa (1982)

In summary, we have:

Tabela 2. Data obtained from COOLPACK software, 2010

Parameters	Point 1	Point 2	Point 3	Point 4	Point 5	Point 6	Point 7
Pressure (P_n) [bar ABS]	2.957	18.2067	18.2067	18.2067	18.2067	2.957	2.957
Temperature (T_n) [°C]	1.0	93.9	47,2	47.2	41.2	-15.0	-15.0
Specific volume (υ_n) [m³/kg]:	0.08378 0	0.00166 2	0.01255 0	0.00290 0	NA	0.02800 0	0.007762
Enthalpy (h_n) [kJ/Kg]:	410,284	460,59	417,58	259,4	251,26	251,26	399,55
Enthalpy (s_n) [kJ/kg.K]:	1.8154	1.8154	1.69	1.69	1.172	1.201	1.775
Title (x_n):	NA	NA	1	0	NA	0,316	1

Source: The authors

3.3 MASS FLOW CALCULATION

Considering that the condenser unit already has its capacity defined, we can calculate the necessary refrigerant mass flow rate to achieve this capacity, knowing that the heat flow to be absorbed by the condenser unit must include both the system's evaporator and the suction line, which encompasses the respective superheating. Thus, we can write (ÇENGEL, 2012):

$$\dot{q}_t = \dot{m}(h_7 - h_6) + \dot{m}(h_1 - h_7) \rightarrow \dot{q}_t = \dot{m}(h_1 - h_6) \qquad (1)$$

where:

$\dot{q}_t$ is the total heat flux,

$\dot{m}$ is the required mass flow,

h_7 is the enthalpy of the fluid at the end of the evaporator,

h_6 is the enthalpy of the fluid at the evaporator inlet,

e h_1 is the enthalpy of the fluid at the compressor inlet.

Furthermore, knowing that 430kcal/h is equivalent to 1799,12kJ/h ≅ 0.4998kW, we can obtain the mass flow value as:

$$\dot{m}_{R22} = \frac{\dot{q}_t}{(h_1 - h_6)} = \frac{1779{,}12kJ/h}{(410{,}284kJ/kg - 251{,}26kJ/Kg)} \cong 11{,}1878kg/h \cong 0{,}00311kg/s \qquad (2)$$

3.4 HEAT FLUX IN THE EVAPORATOR

The theoretical heat flux in the evaporator for sizing purposes should be the product of the system's mass flux by the difference in enthalpy between the points representing the evaporator outlet and its inlet, respectively. h7 e h6, as follows:

$$\dot{q}_{t_6}^{7} = \dot{m}(h_7 - h_6) = 0{,}4611819kJ/s \cong 0{,}4612kW \cong 396.56\text{kcal/h} \qquad (3)$$

The evaporator will be internally housed in a concrete block (cement, sand, and gravel in a specific mix) with a maximum thickness of 25 mm. The water, initially in liquid form, will be stored in a tank, the volume of which will correspond to the product of the base surface area and the height of the ice layer to be formed, which will not exceed 38 mm. Given the educational purpose of the rink, we will use reduced dimensions for the system to occupy as little space as possible.

The basic dimensions are defined as a width of 0.3 m and a length of 0.5 m, allowing us to determine the height for the possible water volume, considering that the thermal load should not exceed the capacity of the machine, taking into account the processing time to reach the operating regime, i.e., to function for the heat removal necessary only to maintain the surface temperature plus losses.

For ice block production, we assume that the sides and the bottom surface of the assembly will be adequately insulated so that the heat transfer from the external environment to the "concrete" blocks and ice is negligible.

We need to lower the temperature of the water (distilled), with a density of $\rho \cong 1000kg/m^3$, from the equilibrium temperature with the environment, T_{amb}=32.2°C, to

the freezing temperature of water under atmospheric pressure, T_{cong}=0°C. Since the specific heat varies with the fluid temperature but considering that this variation is not significant for the procedure, we will adopt the average specific heat of water for this range, $cp_1 \cong$1.0kcal/kg°C.

After the entire volume of water reaches a temperature of 0°C, it will be necessary to continue removing heat from the volume to promote its freezing at a constant temperature, using a latent heat of solidification for water of L≅80kcal/kg. Subsequently, the volume of water, now in the solid state – ice at 0°C, will be cooled from the freezing temperature to the conservation and application temperature of the ice rink, considering the specific heat for this temperature range, $cp_2 \cong$0,505kcal/kg.°C. This conservation temperature usually depends on the rink's application, with commonly applied ranges as follows: -2°C up to -3°C for recreational skating; -3°C up to -4°C for figure skating; and -5°C up to -6°C for hockey and other sports like speed skating.

Considering that the system must ensure operation to achieve the lowest temperature within the application ranges, we opted to adopt -6°C for the ice block, as this is the most critical.

Considering that initially the concrete will also be at ambient temperature, we must add the amount of heat required to lower the temperature of the concrete block to the operating temperature of -9°C.

Knowing that its specific heat is cp≅ 0.2102kcal/kg.°C, the volume will be $\forall_{concrete} \cong$0.00375m³ (considering 0.3m × 0.5m × 0.025m), and its density is $\rho \cong$2300kg/m³,, we can define the initial load (Stoecker, 2002) knowing that:

$$Q = m.cp.\Delta T \qquad (4), \text{ and}$$

$$Q = m.L \qquad (5)$$

Where:

Q is the amount of heat to be removed in kcal,
m is the mass of the material in kg (kilogram),
cp is the specific heat of the material in kcal/kg°C,
ΔT is the temperature difference for the calculated range in °C,

And *L* is the latent heat of solidification of the material, in kcal/kg, when applied.

We will have:

$$Q_{t,conc} = m_{conc}.cp_{conc}.\Delta T_{conc} \therefore Q_{t,conc} = \rho_{conc}.V_{conc}.cp_{conc}.\Delta T_{conc} \cong 74{,}6946kcal \quad (6)$$

We need to define the height of the water sheet, that is, the height of the ice block, considering the initial capacity of the evaporator subtracting the amount of heat to be removed from the concrete. Assuming a process time equivalent to 1 hour of operation, that is:

$$Q_{t,Concreto} + Q_{t,H_2O} = Q_{TOTAL};\ Q_{t,H_2O} = 321{,}8654kcal \quad (7)$$

therefore:

$$Q_{t,H_2O} = m_{H_2O}\ (cp_1.\Delta T_1 + L + cp_2.\Delta T_2) \therefore m_{H_2O} \cong 2{,}7932kg \cong 2{,}8kg \quad (8)$$

This mass, considering the density of water, gives us a volume:

$$\forall = \frac{m_{H_2O}}{\rho_{H_2O}} = \frac{2{,}8kg}{1000\frac{kg}{m^3}} \cong 0{,}0028m^3 \approx 2{,}8l \quad (9)$$

Considering the processing time, we will freeze 2.8 liters of water. For the given area dimensions, the height of the water layer would be 18.6 mm, which is too low for the application. Therefore, we have decided to double the processing time, considering twice the volume of water, i.e., $\forall_t = 0{,}0056m^3$.

$$\forall = A_{base}.h \therefore h = \frac{\forall}{A_{base.}} = 0{,}037333m \cong 37mm \quad (10)$$

where:

h is the height of the water sheet from the “concrete” base.

Therefore, from this volume we determine the height of the reservoir, considering the base at 0.3m x 0.5m, Abase=0.15m² reaching 37mm.

The system's evaporator will be fabricated using flexible copper tubing with 99.9% purity, having a commercial outer diameter of 3/8” (9.52mm) and an indicated wall thickness of 1/8” (0.79mm). This tubing is sold in "pancakes" or rolls approximately 15 meters long and has a linear weight of about 0.193kg/m. This material and form were chosen to facilitate the construction of the evaporator coil using the smallest bender available in the local market, a manual bender for flexible copper tubes with diameters of ¼”, 5/16”, and 3/8”, which has a bending radius of approximately 25mm, allowing for the maximum number of passes within the volume of the rink.

Figura 4. a) Flexible copper tube bender ∅1/4”, 5/16” e 3/8”, e b) Flexible copper coil type evaporator.3/8”.

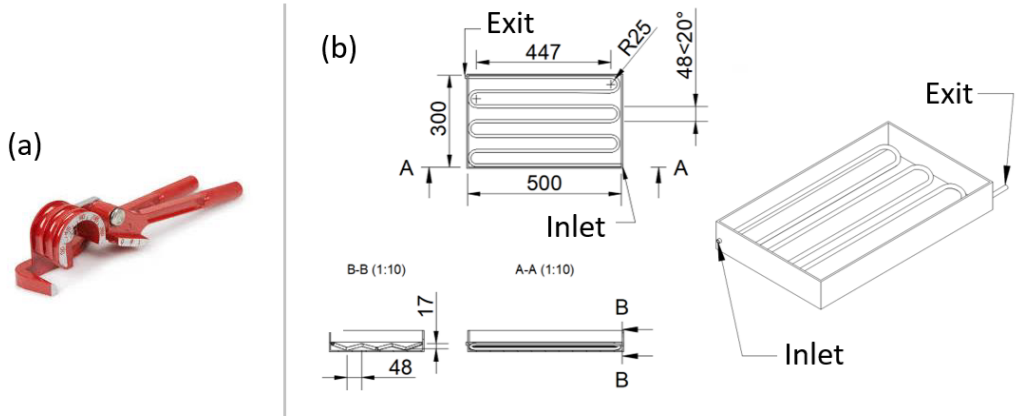

Source: The authors

Thus, assuming the maximum length of tubing distributed in the area of 0.3 m x 0.5m inside the tank, with 5 passes of 450mm, 6 bends of 180° each with a length of 78.54mm, and two passes (inlet and outlet) of 475mm, the total length of the heat exchanger coil (evaporator) will be 3.67 meters.

To determine the heat flux in the evaporator coil of the system, knowing that the refrigerant fluid will absorb the heat that reaches the walls of the tubing, we can apply Fourier's law for heat conduction:

$$\dot{Q} = -k.A.\frac{dT}{dx} \qquad (11)$$

where:

$\dot{Q}$ is the heat flow,

k is the thermal conductivity coefficient of the material,

A is the heat exchange surface area,

and $\frac{dT}{dx}$ is the difference in temperature in relation to the variation in the thickness of the material.

Figura 5. Cross section of a) a copper tube and b) a wall with specific material

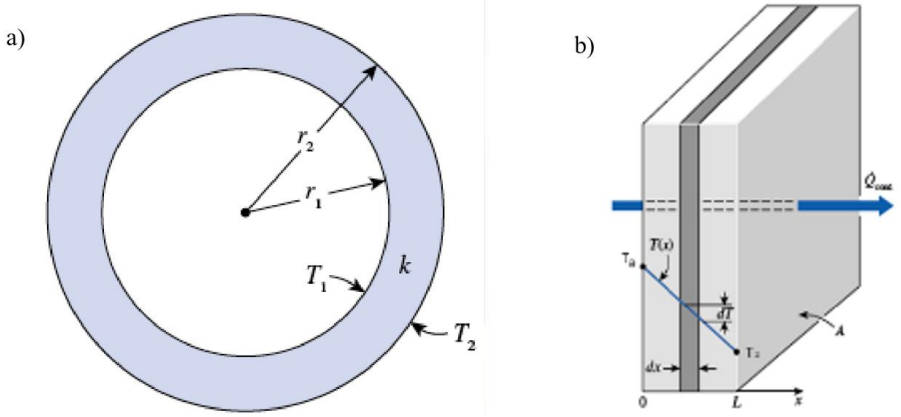

Source: Çencel, 2012.

Knowing that the heat flow through the walls of the copper tube will depend on the exchange area and that this varies according to the radius of the pipe, with A=2. π..r.L, being the radius and L the length of the pipe, we develop equation (11) applying integration intervals in r^1 to r^2 and T^1 to T^2, considering that the heat flow is towards the interior of the pipe:

$$\frac{\dot{Q}}{A}dx = -kdT \therefore \int_{r_1}^{r_2} \frac{\dot{Q}}{A}dr = -\int_{T_2}^{T_1} k\,dT$$

$$\dot{Q} = -2.\pi.L.k.\frac{(T_1 - T_2)}{(\ln r_2 - \ln r_1)} \qquad (12)$$

where:

$\dot{Q}$ is the heat flux through the thickness of the tube,

k is the thermal conductivity coefficient of copper,

A is the heat exchange surface area,

L is the length of the tube,

T_2 is the external temperature in the tube,

T_1 is the internal temperature of the tube,

r_2 is the outer radius of the tube,

and r^1 is the inner radius.

For the layers of concrete and ice, the heat flux passing through these portions can be simplified by considering conduction in flat walls. To this end, we assume that the material constituting the layers is uniform and that the temperature variation within the wall is uniform throughout its thickness.

We will write the Fourier's Law equation (5) applying the integration limits from 0 to *L* for dx and from T^a to T^2 for d^T:

$$\dot{Q}dx = -kAdT \;\; \therefore \dot{Q}\int_0^L dx = -kA\int_{T_a}^{T_2} dT$$

$$\dot{Q} = -\frac{kA}{L}(T_2 - T_a) \qquad (13)$$

where:

$\dot{Q}$ is the heat flow through the concrete wall,
k is the thermal conductivity coefficient of concrete ranging from 0.54 to 1.80W/m.K,
A is the heat exchange surface area of the track base,
and L, in this case, it is the linear dimension of concrete thickness equal up to 0.00774m,
T_2 is the temperature corresponding to the external surface of the tube,
T_a is the temperature of the surface of the concrete, at the interface with the ice.

Assuming that there will be no heat flux to the isolated sides of the track when in steady state, the heat flux passing through the ice and concrete should be equal to the heat flux that must be absorbed by the coil. Thus, we can adopt the evaporator capacity value, calculated as $\dot{q}_{t_6}^{\,7} \cong 396.56\text{kcal/h} \equiv 0.4612kW$, as the maximum heat flux to be absorbed by the coil walls.

$$\dot{q}_{t_6}^{\,7} = \dot{Q}_{evap} = -2.\pi.L.k.\frac{(T_1 - T_2)}{(\ln r_2 - \ln r_1)} \qquad (14)$$

By writing L as a function of T, in this configuration it is possible to estimate the temperature on the external surface of the pipe, coil:

$$L.(T_1 - T_2) = \frac{\dot{Q}_{evap}(\ln r_2 - \ln r_1)}{-2.\pi.k} \rightarrow T_{set} = T_2 = -14{,}99582179°C \qquad (15)$$

For the model in question, the definitions of the ice surface temperature, maintained at -6°C, and the concrete temperature, set around -9°C, are crucial. The refrigerant has a pre-defined temperature of -15°C due to the application of the available condenser unit, so that all the refrigeration capacity required for the process will be fully met by the refrigerant in direct expansion circulating through the coil.

Figura 6. Heat transfer model in heat exchanger.

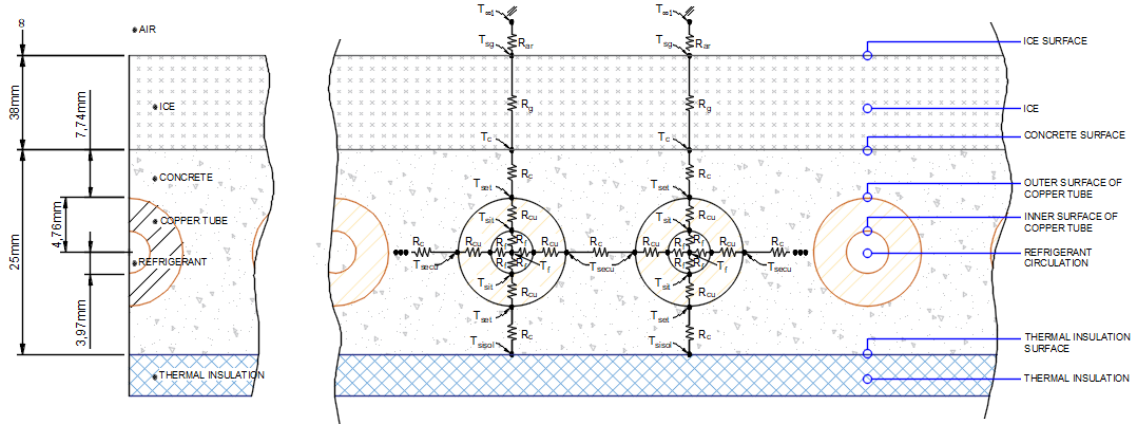

Source: The authors

In Figure 6, the analysis of a pair of tubes from the coil demonstrates the association of the system's thermal resistances. The total heat transfer ($\dot{Q}_{total}$) to the fluid can be divided into three parts: the heat flow from the ice surface to the refrigerant ($\dot{Q}_{g-t}$); the heat flow from one inlet tube pass to an adjacent outlet tube pass ($\dot{Q}_{te-tr}$); and the heat flow from the insulation to the refrigerant ($\dot{Q}_{t-isol}$). Therefore, the total cooling required can be expressed as:

$$\dot{Q}_{total} = \dot{Q}_{g-t} + \dot{Q}_{te-tr} + \dot{Q}_{t-isol} \qquad (16)$$

Assuming that the fluid flow inside the evaporator is completely turbulent and that, from this, we can consider the saturation temperature of the fluid as equal to the temperature of the internal surface of the copper tubing, and further, that we can maintain the ice surface temperature constant, we can neglect the terms involving convective coefficients of the regime. It should also be noted that the heat flow between the tubes, on both sides, will be zero ($\dot{Q}_{te-tr} = 0$), because the temperatures of the internal copper surfaces will be equal, making the temperature differential null ($\Delta T = T_{sit}^{entrance} - T_{sit}^{exit} = 0$).

Defining each component separately:

$$\dot{Q}_{g-t} = \frac{\Delta T}{R_{total}} = \frac{T_{\infty 1} - T_f}{R_{ar} + R_g + R_c + R_{cu} + R_f} \quad (17)$$

where:

$T_{\infty 1}$ is the temperature at the ice surface,
T_f is the temperature of the fluid inside the tube,
and R_{ar}, R_g, R_c, R_{cu} and R_f are the thermal resistances to heat flow through the air, ice, concrete, copper wall, and refrigerant fluid, respectively.

Therefore, the total heat flow to be considered will be:

$$\dot{Q}_{total} = \dot{Q}_{g-t} = \frac{\Delta T_{g-t}}{R_{g-t}} = \frac{T_{sg} - T_{sit}}{R_g + R_c + R_{cu}} \quad (18)$$

where:

L_g is the thickness of the ice layer,
$L_g = 0.038m$; k_g is the thermal conductivity coefficient of ice for the temperature range considered,
$k_g = 1.62W/m.°C$;
L_c is the thickness of the concrete layer, considering from the interface with the ice to the top of the copper pipe,
$L_c = 0.00774m$; k_c is the thermal conductivity coefficient of concrete,
$k_c = 0.74W/m.°C$; A_s is the surface area of the blocks,
$A_s = 0.15m^2$;
r_2 is the external radius of the adopted pipe,
$r_2 = 0.00476m$;
r_1 is the inner radius,
$r_1 = 0.00397m$; L_t is the length of the copper pipe,
$L_t = 3.67m$; e k_{cu} is the thermal conductivity coefficient of copper,
$k_{cu} = 414.7W/m.°C$.

With all the indicated values in hand, we obtained:

$R_g = 0{,}1563786\,\frac{^\circ C}{W}$; $R_c = 0{,}069729729\,\frac{^\circ C}{W}$; $R_{cu} = 0{,}0000189781\,\frac{^\circ C}{W}$; e $R_{total} = R_{g-t} = 0{,}226127307\,\frac{^\circ C}{W}$ (19)

Then applying equation (11):

$$\dot{Q}_{total} = \dot{Q}_{g-t} = \frac{\Delta T_{g-t}}{R_{g-t}} = 39{,}80058897W \cong 34{,}2223\text{kcal/h} \quad (20)$$

The heat load from the ice surface at -6°C to the inner surface of the pipe at the refrigerant saturation temperature, -15°C, is 34.2223kcal. The nominal capacity of the condensing unit, 430kcal/h, corresponds to the sum of the water and concrete loads, considering 1 hour of process time, and a given flow rate:

$$\dot{Q}_{nominal} \cong 321{,}8kcal/h + 74{,}6kcal/h + 34{,}2\text{kcal/h} \cong 430{,}6kcal/h \quad (21)$$

4. CONCLUSION

As presented, the machine to be constructed shows, within the considerations made, a thermal load adjusted to the nominal capacity of the condensing unit for a processing time of up to two hours.

Disregarding the thermal loads from the environment in which the machine will be placed, the Elgin condensing unit, operating in conjunction with the components specified by the manufacturer Danfoss and the proposed control system, will validate the estimated thermal load calculation procedure, the selection of cycle components, and the proposed startup, configuration, and adjustment procedures.

The total thermal load will be 430 kcal/h, compatible with the capacity of the allocated condensing unit, applied at an evaporation temperature of -15°C in a 3.67-meter-long copper coil surrounded by 25mm thick concrete, as shown in Figure 4.b. This setup supports a volume of distilled water of 0.0056 m³ or 5.6 liters in an appropriate reservoir, configuring the ice of the ice rink floor, with thermal insulation on the sides and bottom being a prerequisite.

5. CONCLUSION

There are several possible combinations for the complete assembly of a system based on the initial parameters, including the determination of the geometry of the ice rink tubing. In this work, the theoretical modeling was proposed to simplify practical reproduction from the construction of the calculated and sized equipment.

It should be noted that for future work, a more comprehensive modeling could further approximate the results obtained from practical application through the construction of the machine. Considerations such as fixed physical allocation could allow for the inclusion of estimates for load due to infiltration, radiation, humidity variations, and convection from the environment in contact with the rink surface.

The specification of the accessory components for the construction and assembly of the machine is proposed as the subject of the second part, the continuation of this work, which will also define the basic procedures for commissioning, balancing, and adjustments for the startup of the real machine to be built.

REFERÊNCIAS

_____, *Littell's Living Age*, Vol. 1: From 11 April to 3 August, 1844 (Classic Reprint), 782 páginas, editora Forgotten Books,

ASHRAE. 2014. *ASHRAE Handbook - Refrigeration.* Atlanta: American Society of Heating, Refrigeration, and Air-conditioning Engineering, Inc. Atlanta: GA, 2014.

BRASIL. Ministério do Meio Ambiente. *Uso de refrigerantes naturais em sistemas de refrigeração e ar-Condicionado*. Seminário de Difusão – ANPRAC. Brasília, 2008.

CALISKANA, H.; HEPBASLIB, A. *Energy And Exergy Analyses Of Ice Rink Buildings At Varying Reference Temperatures.* Saudi Arabia:Energy and Buildings, 2010.

ÇENGEL, Yunus A.; GHAJAR, Afshin J. *Transferência de Calor e Massa: uma abordagem prática*. 4. ed. New York: McGraw-Hill, 2012.

COOLPACK VERSION 1.50. *Software COOLPACK*. 2000-2010. Disponível em: < https://www.ipu.dk/products/coolpack/>. Acesso em: 12 abril.2024.

Coolselector®2 Version 5.4.5.758. Banco de dados 110. *Software* Coolselector®2. 1990-2024. Disponível em: <https://www.danfoss.com/pt-br/service-and-support/downloads/dcs/coolselector-2/>. Acesso em: 12 abril.2024.

COSTA, E.C. *Refrigeração*. São Paulo: Edgard Blücher, 1982.

DANFOSS. *Catálogo de válvulas e controles*. São Paulo: Danfoss, 2015.

ELETROBRAS. *Eficiência energética em sistemas de refrigeração industrial e comercial*. Rio de Janeiro: Eletrobras, 2005.

ELGIN. Catálogo Unidades Condensadoras ELGIN. Março-2024. Disponível em: < https://content.elgin.com.br/assets/arquivos/download-center-refrigeracao/Cat%C3%A1logo%20-%20Comercial%20Leve%20-%20Mar%C3%A7o%202024%20-%20EN.pdf> Acesso em: 12 abril.2024.

KARAMPOUR, MAZYAR. *Measurement and Modelling of Ice Rinks Heat Loads - Master of Science Thesis*. Stockholm: KTH Industrial Engineering and Management, 2011.

NASA Earth Observatory. 2012. *Watching the Ozone Hole Before and After the Montreal Protocol*.

STOECKER, W. F.; SAIZ JABARDO, J. M. *Refrigeração industrial*. São Paulo: McGraw-Hill, 2002.

TUTUMLU, HAKAN.; YUMRUTAS, RECEP.; YILDIRIM, MURTAZA. *Investigating termal performance of an ice rink cooling system with an underground termal storage tank.* Turkey: Energy Exploration & Exploitation, 2018.

WIRZ, D. *Refrigeração comercial para técnicos em ar-condicionado*. São Paulo: Cengage Learning, 2011.

ZHOU, W.; GAN, Z.; HAN, L. *Simulation of the Optimal Refrigerated Floor Design for Ice Rinks.* China: Energies, 2021. Disponível em: https://doi.org/10.3390/en14061535. Acesso em 09 abril.2024.

CHAPTER 2

EDUCATIONAL REFRIGERATION SYSTEM PROJECT FOR THE GENERATION OF AN ICE RINK: PART 2

Wertson da Silva Resende
Institution: Universidade Federal do Rio Grande do Norte (UFRN)
Address: Campus Universitário Lagoa Nova, Caixa Postal 1524, Natal, RN, Brasil, CEP 59078-900
E-mail: wertson.resende.012@ufrn.edu.br

Cleiton Rubens Formiga Barbosa
Universidade Federal do Rio Grande do Norte (UFRN)
Address: Campus Universitário Lagoa Nova, Caixa Postal 1524, Natal, RN, Brasil, CEP 59078-900
E-mail: cleiton.formiga@ufrn.br

Sandi Itamar Schafer de Souza
Institution: Universidade Federal do Rio Grande do Norte (UFRN)
Address: Campus Universitário Lagoa Nova, Caixa Postal 1524, Natal, RN, Brasil, CEP 59078-900
E-mail: sandi.souza@ufrn.br

Álvaro Augusto Soares Lima
Institution: Universidade Federal do Rio Grande do Norte (UFRN)
Address: Campus Universitário Lagoa Nova, Caixa Postal 1524, Natal, RN, Brasil, CEP 59078-900
E-mail: alvaro.augusto@ufrn.br

Cleiton Rubens Formiga Barbosa Júnior
Institution: Universidade Federal do Rio Grande do Norte (UFRN)
Address: Campus Universitário Lagoa Nova, Caixa Postal 1524, Natal, RN, Brasil, CEP 59078-900
E-mail: cleitonformiga@gmail.com

Ângelo Roncalli Oliveira Guerra
Institution: Universidade Federal do Rio Grande do Norte (UFRN)
Address: Campus Universitário Lagoa Nova, Caixa Postal 1524, Natal, RN, Brasil, CEP 59078-900
E-mail: angelo.roncalli@ufrn.br

ABSTRACT: This work, as Part 2, aims to compile the information presented in Part 1, select the accessory components defining the configuration of the ice rink refrigeration system – pista de gelo – in its refrigeration circuit, present details of construction and assembly, and propose procedures for startup, commissioning, and adjustments, highlighting the reference parameters for efficient equipment operation.

It includes the cycle of simple vapor compression with direct expansion and its controls, using a commercial ¼ HP condensing unit, determining the parameters and their intensities for Operation Testing, Adjustment, and Balancing – TAB – of the system.

KEYWORDS: Components, Construction and Assembly, Refrigeration System, Ice Rink, Educational.

RESUMO: Este trabalhao, como parte 2, objetiva compilar as informações dispostas na Parte 1, selecionar os componentes acessórios definindo a configuração do sistema de refrigeração da pista de gelo – *ice-Rink* – em seu circuito frigorífico, apresentar alguns detalhes de construção e montagem, e propor os procedimentos para realização do *start-up* (partida), comissionamento e ajustes ressaltando os parâmetros de referência para que o equipamento opere de forma eficiente. Nele encontram-se constituídos o ciclo a compressão de vapor simples com expansão direta e seus controles, aplicando uma unidade condensadora comercial de ¼ HP determinando quais serão os parâmetros e suas intensidades para Teste de operação, Ajuste e Balanceamento – TAB - do sistema.

PALAVRAS-CHAVE: Componentes, Construção e Montagem, Sistema de Refrigeração, Pista de Gelo, Didático.

1. INTRODUCTION

The ice rink project (educational), as detailed in Part 1, is designed for educational purposes and aims to facilitate the study of such systems, applying a simple vapor compression refrigeration cycle with direct expansion and its controls. It is presented on a reduced scale and will be part of the Mechanical Engineering Department's Energy Laboratory at UFRN for practical classes.

Ice rinks are considered any level layers of ice, whether natural or artificially created through refrigeration systems, intended for recreational and sporting activities such as recreational skating, artistic skating, hockey, speed skating, acrobatics, and even Olympic competitions like biathlon, bobsled, Nordic combined, curling, and other possible events.

Artificial ice rinks can be installed in open environments or enclosed spaces such as gyms, shopping centers, arenas, auditoriums, and coliseums. In these, the refrigeration system assumes various configurations, with the most common being indirect expansion systems using secondary fluids. However, considering the objectives of this work, a simple vapor compression system with direct expansion and a flexible copper tubular evaporator embedded in a concrete block, through which the R22 fluid circulates directly, is initially developed here.

Figure 1. Example of a sustainable ice arena, IIHF (International Ice Hockey Federation).

Source: IIHF (International Ice Hockey Federation)

2. SYSTEM COMPONENTS

2.1 CONDENSING UNIT

The system will be composed of the previously selected condenser unit, which has a commercial reference power of ¼ HP for the working fluid R22 and a single-phase electrical supply of 220VAC/60Hz. This unit has a standard composition, consisting of a hermetic reciprocating compressor, a copper tubular condenser with aluminum fins, a fan, a carbon steel liquid receiver tank, 3-way service valves for inlet (suction) and outlet (liquid line), and copper interconnection piping.

2.1.1 Compressor

The compressor is a hermetic reciprocating type for R22 refrigerant, with a power supply of 220VAC/60Hz, and has a nominal current of 2.5A. The compressor type is CSIR. It features an amperometric relay 9660-C-3018-138 (Klixon manufacturer) and a thermal protector MRP-36AMN-5508 (Texas manufacturer). The maximum operating current is 3.9A, with a locked rotor current of 13.0A. The starting capacitor ranges from 161 up to 193µF at 110VAC. The electrical power consumption is 480W (0.48kW) with a power factor of 0.87. It has a commercial reference of 1/4HP and is designed for a Medium Temperature Range (-15°C up to 0°C). It is charged with Alkylbenzene Oil ISO 32 with a nominal volume of 690ml. The cooling capacity is 430kcal/h at -15°C. The dimensions of the dome are Ø195mm, with a total height without mounts of 193mm. The suction port height is 122mm, the service port height is 153mm, and the discharge port height is 141mm. The diameters of the ports are as follows: suction Ø3/8” (9.52mm), service Ø1/4” (6.35mm), and discharge Ø1/4” (6.35mm).

Figure 2. 1/4HP compressor, manufacturer Elgin.

Source: Manufacturer Elgin.

2.1.2 Condenser

The system's condenser operates with forced air convection, consisting of a copper tubular coil arrangement with aluminum fins and a galvanized steel sheet casing. It includes a fan, also referred to as an air blower, with a single-phase universal motor ref. 1/40 – 8mHP, powered by 220VAC/60Hz, a nominal flow rate of approximately 550m³/h, and an 8” (19 cm diameter) exhaust blade.

Figure 3. 1/4HP condenser, manufacturer Elgin.

Source: Adapted Manufacturer Elgin.

2.1.3 Liquid Reservoir or Liquid Tank

The reservoirs in the system are not mandatory for the proper operation of certain refrigeration cycles and should only be installed when necessary. In such cases, their use is recommended when the systems operate with thermostatic or electronic expansion valves. The unit is equipped with an Elgin liquid tank, reference model 259110 1/4, made of carbon steel, with a volume of 700ml, an inlet connection of ¼” SAE weldable tube, and a 7/8” SAE male thread outlet for service valve installation.

Figure 4. 700ml liquid tank, reference 259110 1/4, manufacturer Elgin.

Source: Manufacturer Elgin.

2.1.4 Service Valves

The service valves, used to provide access to the internal pressures of the circuit and perform start-up, commissioning, and adjustment procedures, are positioned in the suction line, at the unit's inlet, and in the liquid line, at the unit's outlet. Both are made of steel with 3 access ports operated by a screw-type actuator driven by a ¼" ratchet wrench (a specific tool for the area). The suction line valve has a ½" SAE male thread with a ¼" SAE service port. The liquid line is equipped with a 3-way valve directly connected to the liquid tank, with a 7/8" female thread, and service and line ports of ¼" SAE.

Figure 5. Service valve, manufacturer Elgin. a) For liquid tank, b) For suction line.

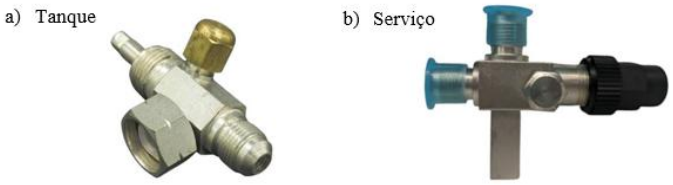

Source: Manufacturer Elgin.

2.2 LIQUID LINE

The liquid line will be constructed using flexible copper tubing with 99.9% purity, having a commercial outer diameter of ¼" (6.35 mm) and a recommended wall thickness of 1/32" (0.79 mm), sold in 'pancakes,' which are rolls approximately 15 meters in length. To select the accessory components for the liquid line, the software Coolselector®2 version 5.4.5.758 was used, applying the sizing and selection data obtained in part 1 of this study. We will now present each component.

2.2.1 Dryer Filter

The selected filter drier is a hermetic type, model DML 032, manufactured by Danfoss, with the commercial reference code 023Z5035, steel body, 1/4" SAE threaded inlet and outlet connections, solid core, desiccant substance 100% Molecular Sieve, solid core surface area of 59 cm^2, solid core volume of 21 cm^3, housing volume of 0.07 l, maximum working pressure of 667 psig, temperature range from -40°C to 70°C.

Figure 6. Filter drier in cross section, manufacturer Danfoss.

Source: The authors

2.2.2 Liquid Sight Glass

Liquid sight glasses are used primarily to indicate the state of the refrigerant in the piping and to check the moisture level in the system. To perform these functions, the SGP 6s model from the manufacturer Danfoss, reference code 014L0007, was selected. It features a type N moisture indicator that works with color coding based on the mixture content: dry (green) <50ppm, intermediate from 50 to 200ppm, and wet (yellow) >200ppm. It is compatible with HC, HFC, and HCFC fluids, has 1/4" SAE external thread inlet and outlet connections, a nominal diameter (ND) of 6, a temperature range of -40°C to 80°C, a maximum working pressure of 52bar/754psig, an inlet and outlet velocity of 0.22m/s, and operates with a pressure drop of 0.001bar under design conditions.

Figure 7. Liquid sight glass with humidity indicator, manufacturer Danfoss.

Source: Manufacturer Danfoss.

2.2.3 Solenoid Valve

The solenoid valve used for on-off control of refrigerant flow in the liquid line is a straight-through model EVR 3 v2 from the manufacturer Danfoss, commercial reference code 032F8107, with a nominal diameter (ND) of 6, 1/4" SAE male thread inlet and outlet connections, NF (Normally Closed) function, Kv value of 0.27m³/h, temperature range from -40°C up to 105°C, maximum working pressure of 45.2bar, inlet and outlet velocity of 0.22m/s, and a pressure drop of 0.002bar under design conditions. The actuating coil operates with a supply voltage of 220VAC at 60Hz frequency.

Figure 8. Details of solenoid valve EVR 2 - EVR 3 (NC).

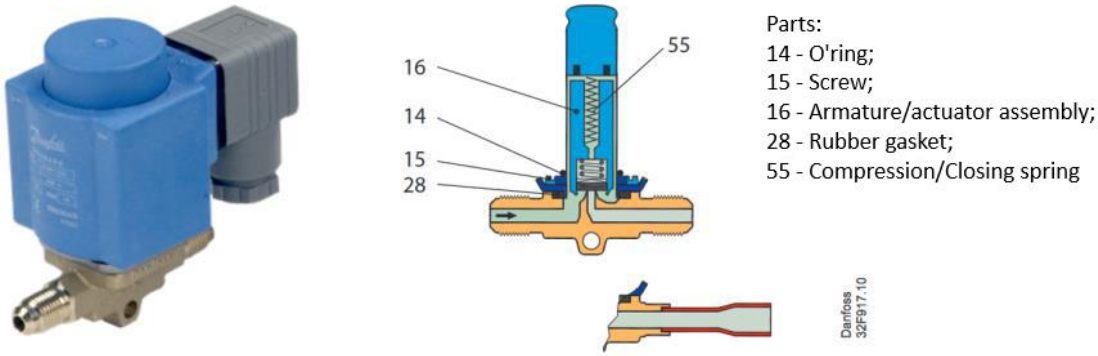

Source: Adapted, Manufacturer Danfoss.

2.3 EXPANSION DEVICE - THERMOSTATIC EXPANSION VALVE

The selected expansion device is the Thermostatic Expansion Valve (TXV) model TXV:T2-X from the manufacturer Danfoss, commercial reference code 068Z3206, with a nominal diameter (ND) of 10, N range (-40°C up to –10°C), MOP-Point of 100psig / 6.9bar (abs) @15°C/60°F, orifice 0X (Danfoss code 068-2002), nominal capacity of 0.982kW, minimum capacity of 0.246kW, TXV charge at 47%, pressure drop (DP) of 15.25bar, inlet velocity of 0.06m/s, 3/8” threaded inlet connection, ½” threaded outlet connection, and no external equalization.

Figure 9. Thermostatic expansion valve with internal equalization TE2, manufacturer Danfoss.

Source: Manufacturer Danfoss.

2.4 EVAPORATOR - COIL PIPING

The piping route was designed as shown in the following figure, where the fluid will flow in a single direction with the evaporator consisting of flexible copper tubing with 99.9% purity, having a commercial outer diameter of 3/8” (9.52mm) and a recommended wall thickness of 1/32” (0.79mm), sold in 'pancakes,' which are rolls approximately 15 meters in length, and has a linear weight of approximately 0.193 kg/m. This tubing is distributed within an area of 0.3m x 0.5m inside the tank with 5 passes of 447mm and 6 bends of 180° with a length of 78.54mm, and two passes (inlet and outlet) of 482mm, totaling 3.67m, arranged as indicated in the figure below.

Figure 10. Flexible copper coil type evaporator 3/8”. type evaporator.3/8”.

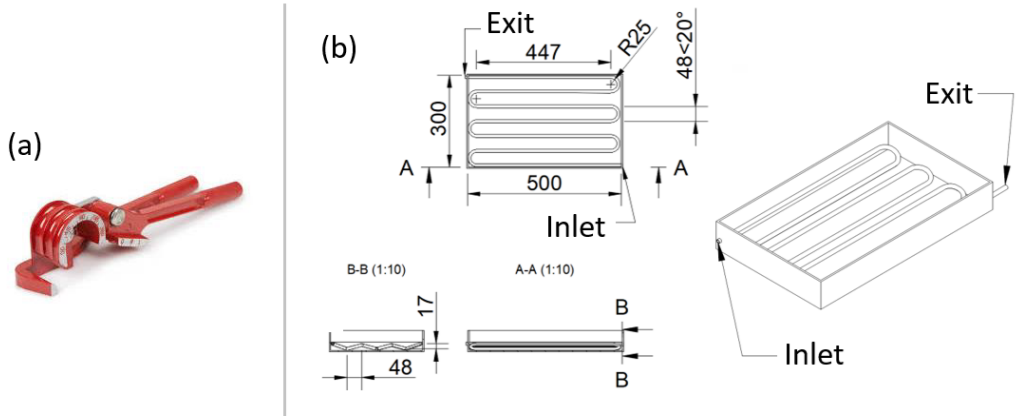

Source: The authors

2.5 SUCTION LINE

The interconnection of the suction pipes, such as the liquid line, will be carried out through brazing or the application of nut-flange type connections.

Figure 11. Flange nut type connection.

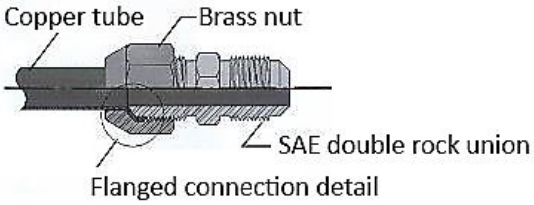

Source: The authors

For the suction line, we will adopt the same piping applied to the evaporator, starting from the insulated ice-rink outlet.

2.5.1 Thermal Insulation

The purpose of thermal insulation is to reduce undesirable thermal exchanges and to maintain the fluid temperature within design limits. It also aims to minimize condensation problems by separating regions with different temperatures.

Thermal insulation is composed of materials with low thermal conductivity (k), mostly porous, which enhances thermal resistance due to the low thermal conductivity of the air contained in the voids.

We selected closed-cell elastomeric foam tubular insulation, type AF/ARMAFLEX® BR with a nominal diameter of 3/8” (~10mm) for copper pipes, with a minimum internal diameter of 11.0mm and a maximum of 12.5mm, reference AFBR M 010, class M (19.0 – 26.0mm), thickness of 19 mm, application range of -50°C to +110°C, thermal conductivity coefficient <0.0033 W/m.K @ 0°C (ASTM C177 and ASTM C518), water vapor diffusion resistance factor μ > 10,000 (ASTM E96), fire reaction class 1 (BS 476: part 7), self-extinguishing, non-dripping, and low flame spread, in black color.

Figure 12. Closed-cell elastomeric foam tubular thermal insulation, type AF/ARMAFLEX® BR.

Source: Manufactorer AF/ARMAFLEX® BR

2.5.2 Suction Accumulator or Liquid Separator

When there is a return of liquid refrigerant or excess oil to the compressor, the most likely result is initially noisy operation, increased intensity and electrical current, and consequently, high energy consumption, mechanical washing of parts, and potential damage to the compressor. The accumulator is installed in the suction line as close as possible to the compressor inlet to prevent this return from occurring. It can also serve an operational function as a temporary storage chamber for refrigerant fluid in specific systems that operate with a reverse cycle or have defrost cycles using superheated steam—'hot gas'. Its internal configuration allows only the suction of gas-phase fluid along with a small amount of oil that enters an internal 'siphon', which is then drawn into the compressor.

Figure 13. Suction accumulator, manufacturer Danfoss.

Source: Manufacturer Danfoss.

We selected the suction accumulator from the manufacturer Danfoss, model ASD015H04 ½", which has a maximum capacity of 7.2 liters, a maximum pressure of 8000kPa(g), an operating temperature range of -15°C up to 50°C, and a pressure vessel hazard level D. The body sheet thickness is 9.3 mm with an allowable tensile strength of 78N/mm², and the thickness of the (top and bottom) caps is 6.2mm with an allowable tensile strength of 130N/mm². The pressure test is 120MPa, and the leak-tightness test pressure is 8.0MPa.

2.6 DRIVE AND CONTROL

The electrical connection of the condenser unit must follow the manufacturer's recommendations, which specify the type of connection to be made for the operation. This operation should account for the control conditions based on the system's application.

The adjustment of the temperature set-point in refrigeration systems directly depends on the type of system and its intended use, such as product preservation or processes. In this case, for an ice-rink system, the set-point temperature should be adjusted to operate the system within the specified range: for our system, it will operate between -5°C and -6°C. To achieve this, we will use the digital temperature controller and indicator shown in Figure 14.

Figure 14. Digital temperature controller and indicator model MT512E, manufacturer FullGauge.

Source: Manufacturer FullGauge Controlls

Considering that the goal of this work is not initially to implement a control system that maximizes efficiency, we opted for a 'pump down system' control. In this system, the digital temperature controller will operate a normally closed solenoid valve in the liquid line, turning it on to allow fluid flow or turning it off to block the line, thereby providing an 'on-off' control. When the valve is turned off, the flow of refrigerant is halted, but the compressor continues to operate, drawing refrigerant from the evaporator and suction line and discharging it to the high-pressure side of the system. This causes the pressure on the low-pressure side to drop to a level where the pressure set-point is reached, and the low-pressure switch deactivates (cut-out) the electrical loads of the condenser unit (compressor and condenser fan).

Figure 15. Combined pressure switch KP15, Danfoss

Source: Manufacturer Danfoss.

From this point on, disregarding the effects of thermal inertia, the temperature of the ice rink surface will tend to rise. Upon reaching the cut-in temperature (activation temperature), which is equivalent to the set-point temperature plus the differential temperature, the digital temperature controller will turn the solenoid valve in the liquid line back on, initiating the flow of fluid through the TXV into the evaporator and suction line. This will increase the pressure at the low-pressure switch pressure point, which, upon observing the adjusted differential pressure, will reactivate the condenser unit's loads, restoring the refrigerating effect of the system until the system's set-point temperature is reached again and a new stop cycle occurs.

Thus, the control will be cyclical, but it must observe the maximum number of compressor starts per hour determined by the manufacturer, which is generally 4 starts per hour.

2.6.1 Temperature controller

A digital controller and indicator for heating or cooling with natural defrost by compressor stop, model MT512E 2HP, was selected. It features a power supply of 230VAC ±10% at a nominal frequency of 50/60Hz, a control range of -50°C to 105°C, an operating temperature range of 0 to +50°C with relative humidity of 10 to 90% RH (non-condensing), a resolution of 0.1°C, and relays rated at 16A for resistive loads and 12A for inductive loads, with a maximum power of 2HP. It has an IP65 protection rating (front) and dimensions of 76mm x 34mm x 77mm.

2.6.2 High and low pressure switches

For the control and protection related to operating and safety pressures of the system, a combined pressure switch (high and low pressure) model KP15 from the manufacturer Danfoss, reference 060-124191, was selected.

This pressure switch allows for adjustment of the low pressure side (left) within the range of -0.20 to 7.50bar (-2.9psig to 108.8psig) with a differential adjustment of 0.70 to 4.00bar (-2.9psi to 58.02psig). For the high pressure side (right), it has an adjustment range of 8.0 to 32.0bar (116.0 psig to 464.1psig) with a fixed differential of 4 bar (58.02psig) and automatic reset. It features SPDT+LP electrical contacts, meaning a switch contact for the low-pressure side with normally closed (NC) in series with the high-pressure contact (identified by A, B, and C).

3. REFRIGERATION CIRCUIT AND ITS COMPONENTS

Once all the components necessary for the functionality of the ice rink system have been selected, we propose the configuration, as shown in Figure 16, of the system based on the refrigeration circuit diagram and its components.

Figure 16. (a) Diagram of the ice rink refrigeration circuit, and (b) Representation, 3D views, of the assembled equipment.

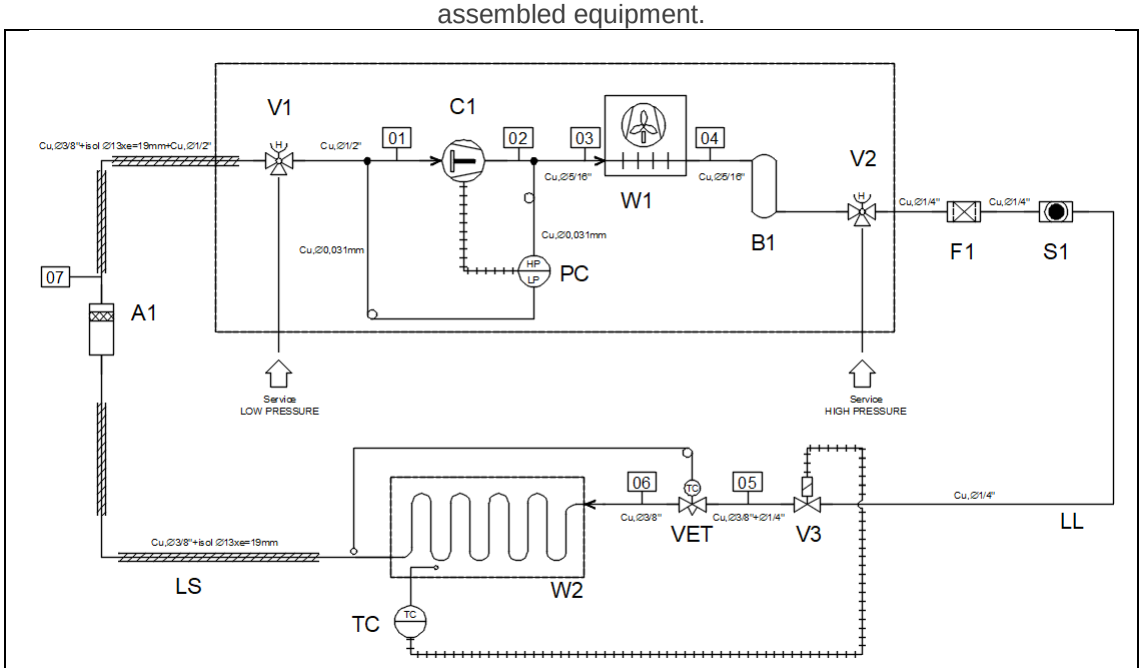

(a) Refrigeration Circuit

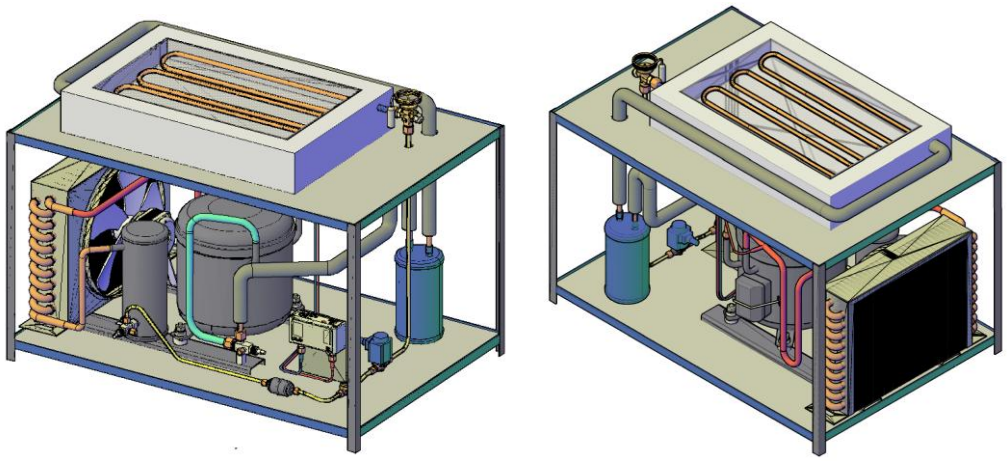

(b) 3D Model

Source: The authors

We present the legend of TAGs (identification labels) of the system components and some of their basic characteristics in table 1 below.

Table 1. System Component Selection Summary

TAG	NOME	Modelo	Fabricante	ØEntrada	∅Saída
V1	3-Way LP Service Valve	3/8”(RM)x3/8” (RM)x1/4” (RM)SAE	Elgin	3/8”R	3/8”R
C1	Hermetic reciprocating compressor	TCM2020E	Elgin	3/8”S	1/4”S
W1	Forced convection finned condenser	45CONDEA2775	Elgin	5/16”S	5/16”S
B1	Liquid tank	259110 1/4HP-700ml	Elgin	¼”S	7/8”R
V2	HP 3-way service valve	7/8”(RF)x1/4” (RM)x1/4” (RM)SAE	Elgin	7/8”R	1/4”R
F1	Filter drier	DML 032	Danfoss	1/4”R	1/4”R
S1	Liquid sight glass with humidity indicator	SGP 6s	Danfoss	1/4”R	1/4”R
V3	NC solenoid valve	EVR 3 v2	Danfoss	1/4”R	1/4”R
VET	EI thermostatic expansion valve	TXV:T2-X	Danfoss	3/8”R	1/2”R
A1	Suction accumulator/Liquid separator	ASD015H04 1/2 in	Danfoss	½”S	½”S
TC	Temperature controller	MT-512E 2HP	FullGauge	NA	NA
PC	High and low pressure combined pressure switch	KP15 SPDT+LP	Danfoss	1/4”R+1/4”R	NA

Source: The authors

4. START-UP, COMMISSIONING AND ADJUSTMENT PROCEDURES

After assembling the system, it is important to follow certain technical procedures to ensure the proper and efficient operation of the assembled components. These procedures can be summarized as follows: leak testing; evacuation and dehydration of the system; refrigerant charging; adjustment of pressure switches; and adjustment of superheat and subcooling.

4.1 LEAK TEST

After assembling the system, it is essential to perform a leak test, as any leakage will result in the loss of refrigerant from the system and a progressive decrease in cooling efficiency until complete shutdown. This leak test is commonly known in the field as a 'leak detection test.'

There are several methods to check for leaks in a refrigeration system, either in the entire system or in specific sections of the circuit. The most common methods are:

(a) Pressurize the system with nitrogen and use soapy foam to check for bubble formation at welded connections or threaded joints; (b) Pressurize the system with nitrogen, record the initial pressure, and after a long period, check if there is a drop in the initial pressure; (c) Pressurize the system with nitrogen, immerse it, if its dimensions allow, in a water tank, and check for bubble formation at welded connections or at nuts and joints; (d) After refrigerant charging, use an electronic leak

detector; (e) In case of leaks, tighten the connections or redo the brazing procedures after purging all the nitrogen used in the test.

To pressurize the system, connect the manifold assembly to the refrigeration circuit, with the red hose to the high-pressure side and the blue hose to the low-pressure side, and the yellow hose (service) to the pressure regulator of the nitrogen (N_2) cylinder. With the regulator valve closed (adjustment screw loosened), open the cylinder's main valve and then adjust the test pressure, usually around 100 to 120 psig. Next, open the manifold valves until the adjusted pressure equalizes with the pressure inside the system, preferably on both the high and low sides.

From there, proceed with the chosen and indicated common procedure from the options listed above (a) up to (e).

4.2 EVACUATION AND DEHYDRATION OF THE SYSTEM

Evacuation refers to the process of creating a vacuum in the refrigeration system by removing non-condensable gases from the system. Dehydration involves removing any moisture particles from the refrigeration system. Refrigeration systems do not operate properly when they contain unacceptable levels of moisture and/or non-condensable gases, as these can alter the physical and chemical properties of the refrigerant and lubricating oil, leading to system failures such as increased condensation pressure and partial or total restriction of the expansion device.

Therefore, it is essential to perform both evacuation and dehydration of the refrigeration system before charging it with refrigerant. To achieve effective evacuation and dehydration, always use an appropriate vacuum pump, specifically high-vacuum pumps, and never use compressors. This is because dehydration relies on lowering the boiling point of water to a temperature below ambient temperature; compressors do not create sufficient vacuum to lower the boiling point below ambient temperature, thus preventing the removal of liquid water from the system.

High-vacuum pumps are those that produce a vacuum below 736mmHg or approximately 28.97inHg. Whenever possible, evacuation should be performed through both the high and low-pressure sides of the system to reduce the time required for this operation and achieve better results. The goal is to reach vacuum levels below 500µHg, with a minimum time of 20 minutes at this level.

The operation time of the pump varies depending on the internal volume of the system, its contamination conditions, and the pump flow rate, measured in liters per minute (l/min) or cubic feet per minute (CFM). Note the equivalence: 1CFM = 1.7m³/h = 28.32 l/min.

To perform evacuation and dehydration of the sealed unit of a refrigeration equipment, follow these steps: (a) Connect the vacuum pump to the system using the manifold assembly, ensuring its valves are in the closed position; (b) Start the pump and open the 'gas ballast' valve for approximately 30 seconds, then close it to open the manual suction valve of the pump; (c) Open the valves on the high and low-pressure sides of the manifold assembly, and wait for the pump to achieve the desired vacuum level; (d) Once the level is below 500μHg and a minimum time of 20 minutes has elapsed, close the manifold valves, close the manual suction valve of the pump, open the 'gas ballast' valve again, and let the pump run for a few minutes to clean its oil; (e) Disconnect the service hose from the pump's suction and proceed with the next start-up steps, which include refrigerant charging.

4.3 REFRIGERANT CHARGE

The correct refrigerant charge is a critical factor in maintaining a refrigeration system, as an incorrect charge can cause various damages. An insufficient refrigerant charge results in reduced system efficiency and consequently, wasted electrical energy. On the other hand, an excess of refrigerant can cause several issues such as: elevated discharge pressure, compressor overheating, increased evaporation pressure, and liquid return to the compressor.

As the first step in charging refrigerant into a system, it is essential to identify the type of refrigerant used in the system. Depending on the refrigerant, the charge can be done in a gaseous or liquid state, or only in the liquid state.

For charging with a gaseous state, which is applicable for R22 as an example, follow these steps:

a) Connect the refrigerant cylinder to the service hose of the manifold;

b) With the manifold valves closed, open the refrigerant cylinder valve;

c) With the system turned off, open the manual valves for low (blue) and high (red) pressure on the manifold. At this point, the refrigerant will flow from the cylinder

to the system. Initially, allow the cylinder pressure to equalize with the system pressure, a process known as "breaking the vacuum," and then close the high and low-pressure valves;

d) Turn on the equipment. The suction pressure will start to decrease, and the high-pressure will begin to increase. Open the low-pressure valve of the manifold to introduce gas until the suction pressure stabilizes at the desired evaporation pressure for the equipment;

e) Simultaneously, measure the electrical current of the compressor motor using a clamp meter. This measurement should be taken at a point in the circuit where only the compressor's total current circulates, typically on the conductor connected to the thermal protector;

f) Compare the measured current with the current rating specified for the compressor in the catalog. The indicated current is obtained under standard laboratory testing conditions, generally at 30°C or 35°C, depending on the manufacturer. If your equipment operates at a different temperature, the measured current may show a slight difference;

g) After completing these steps, evaluate the equipment performance by observing the formation of ice on the evaporator, achieving the temperature for which the equipment was designed, and checking various control parameters and system verification.

4.4 ADJUSTMENT OF PRESSURE SWITCHES

High and low-pressure switches are electromechanical devices used to monitor the pressures on the high and low sides of refrigeration systems. The low-pressure switch is typically used with a pressure port on the suction side of the machine and should shut down the machine if the pressure is too low for proper compressor operation. It should only restart the compressor once the suction pressure reaches a sufficient value for normal operation, without causing continuous cycling, which is known as 'short cycling.'

The high-pressure switch operates with the opposite logic to that of the low-pressure switch. It should shut down the compressor if the discharge pressure is too

high, which could cause overheating of the compressor shell and subsequent carbonization of the compressor oil.

The low-pressure switch has two scales for adjustment on the low side of the system. One scale is labeled 'CUT IN,' which sets the value at which the compressor will restart after stopping due to low pressure. The other scale is labeled 'DIFF,' and it should be adjusted to the difference between the cutoff pressure and the restart pressure of the compressor.

The high-pressure switch has a single adjustment scale labeled 'CUT OUT,' which sets the maximum pressure at which the compressor can operate. This value determines the high-pressure cutoff, typically fixed in relation to the pressure differential. The maximum operating pressure for compressors varies depending on the manufacturer and system (type of refrigerant, compressor, and condenser). For commercial air-cooled units, values between 300 and 400psig are common, depending on the application.

For the low-pressure switch, the 'CUT IN' should be set to 40psig and 'DIFF' to 20psig. With this setting, the system will turn off the compressor at a positive pressure of 20psig, which corresponds to an evaporation temperature of approximately -20°C for R22. This prevents the suction line and compressor from operating under vacuum. It is important to note that this pressure is below the nominal return pressure of the unit and thus not the operational pressure of the system.

The high-pressure switch should be set to a pressure of 300psig, which corresponds to a saturation temperature of R22 at 55°C, an extreme condition assuming the ambient temperature has reached around 40°C.

4.5 SUPERHEAT AND SUBCOOLING ADJUSTMENT

Superheating of the system is commonly used as a parameter to verify the correct refrigerant charge and the balance of thermal load relative to the system. This parameter is divided into two types: useful superheating and total superheating.

Useful superheating is the difference between the saturation temperatures of the refrigerant inside the evaporator, obtained from the saturation pressure measured with the low-pressure gauge, and the temperature of the refrigerant immediately at the

evaporator outlet, considered to be at a distance of 15 to 20cm from the thermodynamic expansion valve bulb sensor installation point.

Total superheating is the difference between the saturation temperatures of the refrigerant inside the evaporator and the temperature of the refrigerant in the suction line immediately before its entry into the compressor, considered to be at a distance of 15 to 20cm from any bend. It is common to measure this temperature before the suction service valve at the condenser unit entry, although the ideal measurement is close to the compressor entry.

Subcooling of the system is also an important parameter, as it involves additional cooling of the saturated liquid to ensure that no vapor reaches the expansion valve, as well as increasing the enthalpy difference in the evaporator, thus enhancing the potential heat transfer.

During the refrigerant charge process, adjustments to superheating and subcooling can be made by adding or removing refrigerant from the system. If the degree of superheating is high and subcooling is low, refrigerant should be added, as this behavior indicates a relatively low mass flow rate through the evaporator compared to a relatively high mass flow rate through the liquid line. Adding refrigerant will decrease the temperature at the evaporator outlet, thus reducing superheating, and the expansion valve will act with proportional closing, reducing the flow in the liquid line. This causes the refrigerant to spend more time releasing heat to the external environment, lowering the temperature at the expansion valve inlet, and consequently increasing subcooling.

Conversely, for low superheating and high subcooling, the procedure would be to remove refrigerant, which will result in the opposite behavior, increasing superheating and decreasing subcooling.

The adjustment of superheating and subcooling via the expansion valve adjustment screw is typically performed once the refrigerant charge is nearly complete, meaning when the condensation pressures, evaporation pressures, electrical current intensity, and process temperatures are close to or at design levels, and the desired parameters are not achieved through mere addition or removal of refrigerant.

Under these conditions, the expansion valve adjustment screw should be turned in increments of ¼ to 1 full turn per adjustment. Turning counterclockwise will reduce

superheating and subcooling, while turning clockwise will increase both superheating and subcooling.

For a well-designed system, this simultaneous adjustment of superheating and subcooling is approximately in the ratio of 1K change in subcooling for every 4 or 5K change in superheating.

After making adjustments to the screw, allow time for the expansion valve to respond and stabilize its control, with an average stabilization time of approximately 20-30 minutes. After this period, remeasure the temperatures and determine the new superheating value. If the desired value has not been achieved, repeat the procedure until the target is reached.

Direct expansion cooling coils are typically designed to operate with around 5K of useful superheating, and thermostatic expansion valves are usually factory-adjusted to maintain a useful superheating range between 0 and 13K, or up to 17K. However, different ranges may be adjusted by the manufacturer and designer according to each project.

If system load variations are high and subject to rapid changes, the valves should be adjusted for useful superheating between 5 and 8K, or the expansion valve bulb sensor can be placed in a well in the suction line for more precise control, should lower superheating settings be adopted.

As specified at the beginning of the operational considerations for this work, the machine should operate with a superheating adjustment of 16K and subcooling of 6K

5. CONCLUSION

The machine to be built has a cooling capacity of 430kcal/h with a set-point temperature of -6°C. According to its operational specifications, it should operate under the following conditions:

Table 2. Operating parameters for the machine

Parameter	Operating value
Evaporation pressure	28.6psig/42.96psia/1.95bar G/2.96bar ABS.
Condensation pressure	249.4psig/ 264.1psia/ 17.2bar G/18.21bar ABS.
Superheating	16K
Subcooling	6K
Ambient temperature	32.2°C
Condenser temperature differential	10 a 15K
UC voltage	220VAC
UC current intensity	2.5A
Apparent power	550VA
Effective power	478.5W

Source: The authors

It is considered that by performing the start-up procedures, commissioning, and adjustments in accordance with what is outlined, it is possible to ensure the operation of the system with the parameters indicated in Table 2, considering that minor variations are admissible as all sizing, no matter how meticulous, is based on approximations. Nevertheless, it is expected that under these conditions, the machine will have a COP of around 3.16.

The executive project drawings are developed based on the definitions contained in this work, parts 1 and 2. They include dimensional layouts for the assembly of the support structure, illustrated in Figure 16.b merely for reference; details of the fixation and assembly of the refrigeration components on the structure, with specifications for the type and position of brazing and threaded-flange connections; electrical connection diagrams along with the selection of auxiliary components for the defined control system, "pump down"; assembly layout of the electrical control box; and a general list of electrical and mechanical components. These were omitted as they are not objectives of this work.

6. FINAL CONSIDERATIONS

The design work for this equipment was presented here without detailing some specific procedures and considerations in selection, as they were deemed not significant to the proposal. Aspects such as checking pressure drops in the lines, determining fluid flow velocities, and implementing technological solutions to reduce their negative effects could be the subject of future studies.

It is also suggested to model and construct two other systems, operating with the same ice formation thermal load, applying simple vapor compression cycles with a

"shell and tube" heat exchanger and secondary fluid, and a simple vapor compression cycle with a flooded evaporator and secondary fluid. This would expand technical knowledge and allow for didactic comparisons of each cycle's configurations and parameterizations.

REFERENCES

ASHRAE. 2014. *ASHRAE Handbook - Refrigeration.* Atlanta: *American Society of Heating, Refrigeration, and Air-conditioning Engineering*, Inc. Atlanta: GA, 2014.

ÇENGEL, YUNUS A.; GHAJAR, AFSHIN J. *Transferência de Calor e Massa: uma abordagem prática*. 4. ed. New York: McGraw-Hill, 2012.

COOLPACK VERSION 1.50. *Software COOLPACK*. 2000-2010. Disponível em: < https://www.ipu.dk/products/coolpack/>. Acesso em: 12 abril.2024.

COOLSELECTOR®2 *Version* 5.4.5.758. Banco de dados 110. *Software* Coolselector®2. 1990-2024. Disponível em: <https://www.danfoss.com/pt-br/service-and-support/downloads/dcs/coolselector-2/>. Acesso em: 12 abril.2024.

COSTA, E.C. *Refrigeração*. São Paulo: Edgard Blücher, 1982.
DANFOSS. *Catálogo de válvulas e controles*. São Paulo: Danfoss, 2015.

ELETROBRAS. *Eficiência energética em sistemas de refrigeração industrial e comercial*. Rio de Janeiro: Eletrobras, 2005.

JUREWICZ, CHRIS. "*OT goal pushes Sweden into semi-final: Eriksson Ek scores to give his team a thrilling 2-1 win over rival Finland*". *International Ice Hochey Federation – IIHF*. *News Article 23 May 2024 (News report)*. Disponível em: <https://www.iihf.com/en/events/2024/wm/news/61371/swe_fin_qf>. Acesso em: 12 julho 2024.

STOECKER, W. F.; SAIZ JABARDO, J. M. *Refrigeração industrial*. São Paulo: McGraw-Hill, 2002.

WIRZ, D. *Refrigeração comercial para técnicos em ar-condicionado*. São Paulo: Cengage Learning, 2011.

CHAPTER 3

ANALYSIS OF PHYSICAL RISKS: NOISE AND VIBRATION IN MANUAL GROUND DRILLER

José Antonio Poletto Filho
PhD in Agronomy, Energy in Agriculture
Institution: Universidade Estadual Paulista (UNESP)
Address: Centro Estadual de Educação Tecnológica Paula Souza
E-mail: jose.poletto@fatec.sp.gov.br

Vanessa Aparecida Sanches Campassi de Oliveira
Master in Teaching and Health
Institution: Faculdade de Medicina de Marília
Address: Centro Estadual de Educação Tecnológica Paula Souza
E-mail: vanessa.oliveira177@etec.sp.gov.br

ABSTRACT: The present study sought to describe the activity of professionals using manual ground driller, considering for this purpose: work methodology, changes in legislation and intensity of physical agents: noise and vibration. To this end, the need to respond to the following research problem has arisen: what is the effectiveness of occupational safety standards in protecting workers when handling equipment that generates noise and vibration? The research has with justification the knowledge and recognition of the lesions provoked by the analyzed agent. It was concluded that the levels of agents in focus are above the limits recommended by the legislation.

KEYWORDS: Safety at work, Unhealthy by noise and vibration, Physical agents, Soil boring machine.

RESUMO: O presente estudo buscou descrever a atividade dos profissionais que utilizam motocoveador manual, considerando para este fim: a metodologia do trabalho, as alterações na legislação e a intensidade dos agentes físicos: ruído e vibração. Com este objetivo, surgiu a necessidade de responder ao seguinte problema de pesquisa: qual a efetividade das normas de segurança no trabalho na proteção do trabalhador ao manusearem equipamento que geram ruído e vibração? A pesquisa tem com justificativa o conhecimento e reconhecimento das lesões provocadas pelo agente analisado. Concluiu-se que os níveis dos agentes em foco estão acima dos limites preconizados pela legislação.

PALAVRAS-CHAVE: Segurança no trabalho, Insalubridade, Agentes físicos, Perfurador de solo.

1. INTRODUCTION

According to studies by the World Health Organization (WHO) and the International Labour Organization (ILO) (2016), which consider 19 occupational risk factors, including noise exposure and ergonomic risks, ILO Convention No. 148, Contamination of the Work Environment by Air, Noise, and Vibration, approved by Legislative Decree No. 56 in 1981, requires Brazil to adopt measures to minimize the risks related to the physical agents noise and vibration (ILO, 1981).

According to Casagrande (2015), legislation concerning Hygiene, Safety, and Occupational Medicine is a matter of constitutional legal order, a social right of workers, whereby they must perform their duties in a safe and healthy environment. The employer must take the necessary measures to eliminate the risks arising from the activity, as stated in Article 7, item XXII of the Federal Constitution, which advocates the reduction of risks inherent to work through health, hygiene, and safety regulations. Articles 196 to 200 of the constitutional charter imply that health is a right of all and a duty of the State, while Article 6 guarantees the right to health, work, safety, and social security. Thus, it is the State's duty to regulate, supervise, and control labor environments. Additionally, the Magna Carta ensures the right to a balanced work environment through the use of techniques, methods, and substances that do not pose risks to the lives of those working there. The Consolidation of Labor Laws (CLT), in Articles 154 to 201, as amended by Law No. 6,514/77, which addresses Regulatory Standards related to Safety and Occupational Medicine, places the responsibility for oversight on the public authorities. Therefore, there is no debate about the State's responsibility to monitor and enforce compliance with workplace quality standards and the obligation of companies to comply with the laws and regulations published by the Ministry of Labor and Employment (Garcia, 2010).

Recently, Law No. 13,467, approved on June 13, 2017, introduced several changes to the CLT. One of these changes concerns the additional pay for unhealthy work conditions, an instrument that integrates the general worker protection system and, according to Porto (2017), contradicts ILO Convention No. 155, which addresses adequate protective measures regarding chemical, physical, and biological agents and substances in the workplace.

Vibration: The changes introduced in August 2014 by Ordinance No. 1,297, which addresses the new legislation on Vibration and amends Regulatory Standard No. 9 (Environmental Risk Prevention Program), in Annex No. 8, may not achieve the previously desired effect. The proposed changes in this ordinance are: 1) Inclusion of Annex 1 (Vibration) in the Environmental Risk Prevention Program; 2) Amendment of Annex 8 (Vibration) of Regulatory Standard No. 15 – Unhealthy Activities and Operations; 3) Item 2.3 of Annex 1 – Vibration of the Environmental Risk Prevention Program will only apply to tools manufactured one year after the publication of this annex, without prejudice to obligations already established in other existing official standards.

Thus, before the publication of this ordinance, there were no parameters to determine whether an activity was unhealthy due to vibration. With the emergence of this new focus, unhealthy conditions caused by vibration are now characterized as follows: daily occupational exposure to Hand-Arm Vibration (HAV) corresponding to a Normalized Exposure Resultant Acceleration (NERA) value of 5 m/s^2. Exposure situations to Hand-Arm Vibration exceeding the occupational exposure limits are classified as moderately unhealthy.

Noise: Agricultural machinery generally exposes workers to noise levels above those allowed by legislation, according to Regulatory Standard No. 15 of Ordinance No. 3,214 of 1978 (Santos, 2004).

According to Delgado (1991), noise levels in the range of 65 to 85 dB(A) cause psycho-physiological effects on workers by affecting the nervous system, potentially causing increased blood pressure and heart rate, interfering with sleep, blood pressure, and causing stress. According to Mendes (2005), noise is typically defined as an undesirable sound, while NIOSH (1998) defines noise as an erratic, intermittent, or statistically random oscillating sound. According to Niosh (1996), occupational hearing loss is one of the most significant current issues, affecting workers in industries, construction, transportation, agriculture, and other activities.

The present study discussed the legal framework related to labor legislation, specifically regarding physical agents: noise and vibration, and the effective protection of workers, reflecting improvements in working conditions and the reduction of diseases and injuries caused by these factors.

2 JUSTIFICATION

According to Saliba (2014), the physical agent vibration is not as widely studied compared to other agents, but its occurrence in workplaces is frequent, and its effects on workers are significant. Therefore, understanding, evaluating, and controlling it is very important. On the other hand, noise, although a more studied and well-known agent, can still have severe consequences for exposed workers.

3 OBJECTIVE

The aim of this study was to analyze the exposure to physical agents—noise and vibration—faced by workers who use motorized soil drillers, also known as manual augers, and to examine the evolution of legislation regarding the tolerance limits found in the Brazilian legal framework on occupational health and safety, specifically in Regulatory Standard No. 15 – Unhealthy Activities and Operations, annexes 1 and 8.

4 BIBLIOGRAPHICAL REVIEW

According to Saliba (2014), the physical agent *vibration* has not been as extensively studied compared to other agents, but its occurrence in workplaces is frequent, and its effects on workers are significant. Therefore, understanding, evaluating, and controlling this agent is crucial. On the other hand, *noise*, although a more studied and well-known agent, can still have severe consequences for exposed workers.

The aim of this study was to analyze the exposure to physical agents—*noise* and *vibration*—that affect workers using motorized soil augers, also known as manual augers, and to examine the evolution of legislation concerning tolerance limits in Brazilian labor law, specifically in Regulatory Standard No. 15 – Unhealthy Activities and Operations, annexes 1 and 8.

Professional activities that expose workers to excessive levels of vibration transmitted to the hand-arm system have caused serious health consequences for laborers, ultimately leading to diseases such as *Reynolds Syndrome* (Mendes, 2005). Considering the expansion of Brazil's agricultural frontier, which has been

accompanied by increased mechanization in the field, driven mainly by productivity demands, various pieces of equipment have become commonplace in this work environment. As a result, concerns have grown for the operators of these agricultural machines, who are exposed to the inherent risks of operating such equipment (Euclides *et al*., 2012). Among these risks, the focus of this work is on *noise* and *vibration*.

According to Vendrame (2005), *vibration* can cause several effects on workers, including loss of balance, alterations in the cardiac system, psychological effects, visual disturbances, gastrointestinal issues, impairment of certain organs, and the gradual degeneration of muscle and nerve tissue. The same author (2009) also noted that eliminating vibration is practically impossible since all mechanical equipment produces vibration at some frequency. Therefore, it is crucial to seek ways to mitigate the effects of this agent.

According to OSHA (2005), the European Agency for Safety and Health at Work, worker exposure to noise levels above tolerance limits can lead to hearing loss, exacerbate stress, cause gastrointestinal problems, insomnia, sexual impotence, depression, and increase the risk of accidents. Thus, protective measures for controlling the agent in question must be implemented to mitigate the potential health risks to workers (Soeiro, 2011). The same author also mentions that the adopted measures may be constructive, considered as collective protection (machine design), organizational (work reorganization), or involve the provision of personal protective equipment.

Vibration: Vascular disorders in individuals exposed to hand-arm vibrations were first observed by Reynaud (1969) in 1862, and described in his work titled *Local Asphyxia and Symmetrical Gangrene of the Extremities*. Italian researchers, in 1911, described vibration syndrome in workers operating jackhammers, correlating it with *Reynaud's phenomenon* (Vendrame, 2005). Furthermore, in 1918, a study described miners using jackhammers experiencing hand anemia, which was also associated with the use of chainsaws in forestry work.

In Brazil, Ministry of Health Ordinance No. 1339 (1999) recognizes localized vibrations as occupational hazards. According to Iida (2005), a repetitive motion at constant intervals can be termed vibration, i.e., the oscillation of a body around a point of equilibrium and the forces or moments associated with it. Mendes (2005) explains

that vibration is a vector quantity with magnitude, direction, and sense. Thus, in addition to these variables, other factors must be considered when dealing with localized vibrations: contact area, contact force, finger, hand, or arm posture, and temperature.

Vibration is a natural phenomenon present in all bodies. Therefore, the human body also has its natural vibration. When this coincides with the frequency of the equipment used by the worker, it amplifies the oscillatory motion, and the vibrational energy is absorbed by the body due to the attenuation provided by tissues and organs (Vendrame, 2005).

Regazzi and Ximenes (2005) state that sensitivity to vibration differs depending on the adopted Cartesian axis: longitudinal vibrations along the spine's z-axis differ from the sensitivity of transversal vibrations, along the arms or through the chest, in the x and y axes. Sensitivity varies with frequency; thus, at certain frequencies, tolerable acceleration differs from that at other frequencies.

According to Saliba (2014), vibrations can be classified as: Whole-body occupational vibration—transmitted to the entire body, usually through support surfaces such as feet, back, or buttocks; Hand-arm occupational vibration, or localized—affecting specific body regions, mainly the hands and arms. Vibration can cause intolerable discomfort depending on the activity performed, and comfort levels vary based on various factors, some of which are subjective.

The evolution of legislation regarding this physical agent began with MTE Ordinance No. 1297 of 08/13/2014 (Brazil, 2014). It is important to note that before 2014, there were no nationally defined regulations for vibration as a physical agent. Only after this date, with the advent of the referred ordinance, could exposure to this agent be defined as hazardous or not (Saliba, 2014).

The verification of exposure is based on the limits set by the standard for hand-arm vibrations (Fundacentro, 2013). This standard defines the direction of movement in three spatial axes: x (sagittal), from back to front; y (transversal), from right to left; and z (vertical), from feet to head (Rocha, 2010).

Table 1, taken from NHO Standard 10, presents the criteria for assessing the level of Occupational Exposure to Hand-Arm Vibrations, according to technical considerations and recommended actions based on the Normalized Exposure

Resultant Acceleration (AREN) found in the assessed exposure condition (Fundacentro, 2013).

Table 1. Judging criteria

arem (m/s²)	Considerations	Recommended performance.
0 2,5	Acceptable	None
2,5 3,5	Above the action level	Preventive measures.
3,5 5,0	Uncertainty	Corrective measures, reduction of exposure.
Above 5,0	Above exposure limit	Corrective measures.

Source: NHO 10, Fundacentro, 2013

Still according to standard NHO 10 (Fundacentro, 2013), to determine the total vibration transmitted to the hand-arm system, (a_hv) during the performance of the activity with the equipment under analysis is determined according to equation I.

$$a_{hv} = \sqrt{{a_{hwx}}^2 + {a_{hwy}}^2 + {a_{hwz}}^2} \qquad (1)$$

where:

$a_{hwx}; a_{hwy}; a_{hwz}$ are the values of the frequency-weighted accelerations for the x, y, and z axes, respectively.

To determine the daily exposure corresponding to 8 hours A(8) of work, equation II is used.

$$A(8) = a_{hv}\sqrt{\frac{T}{T_0}} \qquad (2)$$

where:

T is the total daily duration of exposure to vibrations (hours or minutes)
e T_0 is the reference duration of eight hours (hours or 480 minutes).

Noise: Regarding the physical agent noise, and according to the NHO 01 standard from Fundacentro (2001), for comparison purposes with the tolerance limit (Table 2), the standardized exposure level must be determined using equation III.

$$NEN = NE + 10log\frac{T_e}{480} \qquad (3)$$

where:

NEN is the standardized exposure level [dB];
NE, average level representative of daily occupational exposure [dB];
T_e, daily journey [min].

Table 2. Exposure limit NHO 01

NEM [dB]	**Time [min]**
80	1.523,9
81	1.209,52
82	960,00
83	761,95
84	604,76
85	480,00
90	151,19
95	47,62
100	15,00
115	0,46

Source: NHO 01 – Fundacentro (2001)

Thus, the table above briefly indicates the maximum allowable daily exposure time based on noise levels.

When considering the physical agent *noise*, and referencing Ordinance 3.214/1978 (Brazil, 1978), specifically Regulatory Standard No. 15 in its Annex 1: **Tolerance Limits for Continuous or Intermittent Noise**, the permissible daily exposure levels are shown in Table 3.

Table 3. Exposure limit NR 15

NEM [dB]	Tempo [min]
80	--
81	--
82	--
83	--
84	--
85	480
90	240
95	120
100	60
115	15

Source: Ordinance 3.214/1978, BRAZIL, 1978

To determine the dose (D), equation IV is used, in accordance with Regulatory Standard No. 15 (Brazil, 1978).

$$D = \frac{C_1}{T_1} + \frac{C_2}{T_2} + \frac{C_3}{T_3} + \cdots \frac{C_N}{T_N} \qquad (4)$$

When the result exceeds one (D>1), the exposure will be above the tolerance limit.

The Representative Average Level of Daily Exposure (NE) according to Regulatory Standard No. 15 can be determined using Equation V:

$$NE = 10\ log\left(\frac{480}{T_e} + \frac{D}{100}\right) + 85 \qquad (5)$$

where:

NE - Representative Average Daily Exposure Level [dB];
T_e - Worker's exposure time to noise [min];
D – dose [%];

Also according to ordinance 3,214/1978 (Brazil, 1978), the determination of the Standardized Exposure Level (NEN) is calculated using equation (VI).

$$NEN = NE + 16{,}61\ log\left(\frac{T_e}{480}\right) \quad (6)$$

where:

NEN - Normalized Exposure Level [dB];
NE - Representative Average Daily Exposure Level [dB];
T_e - Worker exposure time to noise [min].

Ordinance No. 3.214/78 (Brazil, 1978), in Regulatory Standard No. 15, defines the **Tolerance Limit** as: "the maximum or minimum concentration or intensity, related to the nature and duration of exposure to the agent, which will not cause harm to the worker's health during their working life.

5 METHODOLOGY

The procedures of this research were submitted to the Ethics Committee, and an Informed Consent Form was used.

With the advent of technological advancements in modern agriculture, cost reduction and increased productivity in the field have become possible. The main characteristics of this new phase of agrarian development involve the modernization of machinery, genetics, digitization, and data management, which have enabled greater control over agricultural processes.

In this new concept of agriculture, equipment plays a key role, from land preparation to fertilizer distribution, sowing, and other operations. The mechanization of agricultural processes ranges from the use of large machines and implements, which incorporate all ergonomic concepts, to small tools that facilitate landwork.

Thus, this growing mechanization of the agricultural sector, especially in small rural properties where farmers use equipment powered by internal combustion engines, has led to increased productivity, efficiency, and improved performance of the tasks performed. However, it also brings health risks to the operator, primarily due to the hazards involved in operating these tools. Among these risks are noise and vibration, chemical hazards from combustion gases, and ergonomic risks.

This study does not address ergonomic issues or chemical risks; instead, it focuses solely on assessing the physical agents of localized vibration, transmitted to workers' upper limbs, and noise during the operation of manual motorized hole diggers.

Noise from agricultural equipment can cause auditory problems in operators. According to the Regulatory Standards of the Ministry of Labor and Employment, specifically NR No. 15 – Unhealthy Activities and Operations, in its Annex 1, the maximum daily exposure allowed during an 8-hour workday is 85 decibels. Therefore, this study aimed to evaluate the noise emitted by a manual motorized hole digger. Sound pressure measurements were taken near the operator's auditory system.

The values found were compared to the tolerance limits established by current legislation and previous regulations.

In semi-mechanized hole digging activities, the worker must transport the equipment to the work site and move around the terrain performing perforations, carrying a load of approximately 20 kg. This situation is aggravated by the high physical workload, noise levels, the need for awkward postures, and the generation of both noise and vibration, with the latter two agents being the focus of this study.

For the tests, three motorized hole diggers from different manufacturers were used, with the characteristics described below (Table 4).

Table 4. description of equipment used

Equipment	Power (CV)	Displacement (cm^3)	Drill diameter (m)
1	2,0	52,0	0,15
2	2,0	53,0	0,20
3	2,2	51,7	0,20

Source: Author

The operator drilled three holes with an approximate depth of 0.8 m with each piece of equipment, that is, a total of nine holes, in terrain with similar characteristics, with each drilling lasting approximately 120 s (2 minutes).

6 RESULTS AND DISCUSSIONS

Vibration: For the quantitative assessment of the vibration agent, measurements were taken along the three orthogonal axes—x, y, and z. This methodology is adopted by current standards to determine the overall severity of the vibration.

Thus, considering the importance of the agricultural sector and the health and safety of the operators of this type of equipment, the measurements were carried out using a vibration analyzer with the sensor mounted on the handle of the equipment (Figure 1).

Figure 1. vibration sensor assembly

Source: the author

The reference point for the measurements was the palm of the hand, the area that comes into contact with the handle of the auger, and the acceleration was measured along the three axes: x, y, and z. The equipment used to assess the vibration was a three-axis accelerometer (X, Y & Z), the HVM-200, manufactured by Larson Davis, which allows simultaneous triaxial readings. The worker operated the equipment using gloves and other personal protective equipment (PPE), and the procedures for the test followed the standards established by Fundacentro's NHO 10 (2013).

By applying Equation (I), the weighted acceleration transmitted to the hand-arm system (a_{hv}). was determined. Since 120 readings were generated for each drilling, only the three most representative readings from each axis were tabulated, as shown in Table 5. The final vibration for each piece of equipment and each drilling ($a_{hv}^{x\_y}$), is presented, where the index "x" refers to the equipment and "y" to the drilling.

Table 5. tabulated results according to equation (I)

	First drilling				Second drilling				Third drilling			
Equipment 1	a_{hwx}	a_{hwy}	a_{hwz}	a_{hv}	a_{hwx}	a_{hwy}	a_{hwz}	a_{hv}	a_{hwx}	a_{hwy}	a_{hwz}	a_{hv}
	13,48	5,11	4,89	15,22	10,33	4,72	10,02	27,00	11,92	7,34	16,54	16,54
	13,30	4,92	5,66	15,27	10,31	4,65	10,93	25,03	11,31	5,65	16,42	16,42
	12,57	4,80	5,70	14,62	9,61	4,80	12,23	21,92	8,65	8,90	16,74	16,74
	$a_{hv}^{1\_1}$			14,99	$a_{hv}^{1\_2}$			24,65	$a_{hv}^{1\_3}$			16,56
	First drilling				Second drilling				Third drilling			
Equipment 2	a_{hwx}	a_{hwy}	a_{hwz}	a_{hv}	a_{hwx}	a_{hwy}	a_{hwz}	a_{hv}	a_{hwx}	a_{hwy}	a_{hwz}	a_{hv}
	8,37	4,08	2,90	9,75	8,47	4,42	11,26	24,54	8,47	4,42	14,02	14,02
	8,01	3,86	2,75	9,31	7,27	3,35	8,057	16,81	7,70	2,30	12,72	12,72
	7,45	3,84	3,02	8,92	7,70	3,71	7,461	18,09	7,70	3,71	12,03	12,03
	$a_{hv}^{2\_1}$			9,17	$a_{hv}^{2\_2}$			19,44	$a_{hv}^{2\_3}$			12,57

Equipment 3	First drilling				Second drilling				Third drilling			
	a_{hwx}	a_{hwy}	a_{hwz}	a_{hv}	a_{hwx}	a_{hwy}	a_{hwz}	a_{hv}	a_{hwx}	a_{hwy}	a_{hwz}	a_{hv}
	7,17	3,46	2,60	8,37	6,57	3,55	12,87	17,76	6,57	3,55	14,88	14,88
	8,13	4,91	5,12	10,80	6,70	4,04	9,82	18,34	6,71	3,03	12,28	12,28
	8,24	5,52	4,67	10,96	6,37	3,68	10,78	16,82	7,37	4,65	13,06	15,70
	$a_{hv}^{3\_1}$			10,04	$a_{hv}^{3\_2}$			17,64	$a_{hv}^{3\_3}$			14,28

Source: the author

The acceleration values for each piece of equipment were determined in the same way, that is, the sum of the vibration values for each piece of equipment.($a_{hv}^{x\_y}$) and dividing Poe 3 and are transcribed in Table 6.

Table 6. Vibration level for each equipment

	Equipament 1	Equipament 2	Equipament 3
Vibration (m/s²)	18,73	13,90	13,98

Source: the author

Applying equation (I), the total vibration transmitted to the hand-arm system was determined. (a_{hv}) for equipment and drilling, with the average of the three drillings for each equipment ($a_{hv}^{x\_y}$) is: 207,19 m/s². To determine the daily exposure, corresponding to 8 hours (A(8)), equation (II) was used, considering that the effective working time (T) was two hours. The results are presented in Table 7.

Table 7. Results

Equipament	$\boldsymbol{a_{hv}}$(m/s²)	A(8) (m/s²)
1	18,73	9,36
2	13,90	6,95
3	13,98	6,99

Source: the author

After applying the relevant equations, the results obtained were analyzed considering the permissible vibration values according to the Fundacentro NHO 10 standard, which stipulates the action levels and exposure limits for total vibration transmitted to the hand-arm system (a_hv) of daily exposure, corresponding to 8 hours A(8), as per Table 8.

Tabla 8. result - physical agent vibration

Drilling	a_{hv} (m/s²)	a_{hv} máx.(m/s²)	A(8) (m/s²)
First	18,73	15,27	9,36
Second	13,90	27,00	6,95
Third	13,98	16,74	6,99
Average		19,67	7,76

Source: the author

A variation in the vibration detected by the operator's hand was observed, with a maximum peak of 27.00 m/s² and a daily exposure for an 8-hour period, A(8), of 7.76 m/s², which does not comply with Fundacentro's NHO 10 standard. Considering the maximum acceptable level of 2.5 m/s², the use of the auger begins to cause harm to the operator after just 40 minutes of operation, exceeding the action limit and requiring preventive measures.

Noise: For the evaluations of this agent, an integrator meter manufactured by Instrutherm (DOS-600) was used, with the microphone positioned near the operator's right ear, in accordance with the procedures outlined in Fundacentro's NHO 01 standard. The noise and vibration tests were conducted simultaneously. Table 9 presents the projected sound pressure levels for an 8-hour workday, that is, the noise dose (A(8)).

Table 9. noise dose

	Dose – A(8) %		
	First drilling	Second drilling	Third drilling
Equipament 1	120,7	122,0	142,5
Equipament 2	106,8	104,9	109,4
Equipament 3	98,4	103,2	102,0

Source: the author

Considering that the tolerance limit for the noise agent, according to Regulatory Standard No. 15, is 85 dB (A) for an exposure of 8 hours, it can be seen from the data in the table above that the daily dose was exceeded in all tests, which could cause harm to the worker's health.

7 CONCLUSION

The evaluations conducted and presented in this article provided insights into the vibration and noise phenomena associated with augers, identifying the high levels generated by these devices and indicating that workers should not be exposed to such equipment for extended periods.

It is crucial for manufacturers to adhere to Fundacentro's NHO 10 standard, which establishes action levels and exposure limits based on the vibration transmitted to the operator's hand-arm system. This is essential to prevent health issues for workers using these machines. The findings suggest that advancements in occupational health and safety legislation are insufficient to fully protect machine operators from the high levels of noise and vibration demonstrated. Thus, the maximum exposure time to these agents should be properly defined and adhered to in order to prevent health problems for the operators. Equally important are the workers around the machine operator, who are also exposed to these agents and deserve the same level of protection.

It is known that control of the studied agents begins with the machine design, including factors such as ease of handling, size, design, and mass, which should be optimized to mitigate the harmful effects transmitted to equipment operators. The findings indicate a need for a reengineering process of the equipment to comply with safety and comfort standards. Other agents and situations not addressed in this study should be considered for future research.

In conclusion, the risks associated with exposure to mechanical vibrations and occupational noise should follow the principle of prevention in Safety, Hygiene, and Health at Work, which is to eliminate the risk at the source or reduce it to the minimum.

REFERENCES

OIT, DECRETO LEGISLATIVO Nº 56, DE 1981, disponível em: https://www.trt2.jus.br/geral/tribunal2/LEGIS/CLT/OIT/OIT_148.html, 1981

OIT**,** Joint Estimates of the Work-related Burden of Disease and Injury, 2000-2016: Global Monitoring Report, disponível em : https://www.ilo.org/pt-pt/resource/news/omsoit-quase-2-milhoes-de-pessoas-morrem-cada-ano-de-causas-relacionadas-ao#:~:text=Les%C3%B5es%20ocupacionais%20causaram%2019%25%20das,riscos%20ergon%C3%B4micos%20e%20a%20ru%C3%ADdo, 2016

BRASIL**,** Portaria 1339 G*M* de novembro de 1999, disponível em <http://bvsms.saude.gov.br/bvs/publicacoes/doencas_relacionadas_trabalho_2ed_p1.pdf>, acesso em junho 2017.

BRASIL**,** Portaria MTE nº 1297 de 13/08/2014, *Aprova o Anexo 1 - Vibração - da Norma Regulamentadora nº 9 - Programas de Prevenção de Riscos Ambientais (PPRA), altera o Anexo 8 - Vibração - da Norma Regulamentadora nº 15 - Atividades e Operações Insalubres, e dá outras providências., acesso em janeiro 2018, disponível em* <https://www.legisweb.com.br/legislacao/?id=273605>;

CASAGRANDE, R, 2015, O adicional de insalubridade: um direito constitucional trabalhista, disponível em <https://www.direitonet.com.br/artigos/exibir/9195/O-adicional-de-insalubridade-um-direito-constitucional-trabalhista>, acesso em janeiro/2018.

EUCLIDES Filho, K.,FONTES, R. R., CONTINI, E., Campos, F. A. A., 2012, Revista Política Agrícola, Papel da ciência e da tecnologia na agricultura do futuro; disponível em <https://www.alice.cnptia.embrapa.br/bitstream /doc/930906/1/Opapeldaciencia.pdf>, acesso em janeiro 2018.

FUNDACENTRO 2013, Avaliação da Exposição Ocupacional a Vibrações em Mãos e Braços, NHO 10.

GARCIA, Gustavo Filipe Barbosa. Meio Ambiente do Trabalho e Direitos Fundamentais: Responsabilidade Civil do Empregador por Acidentes do Trabalho, Doenças Ocupacionais e Danos Ambientais. **Revista IOB Trabalhista e Previdenciária**, IOB, 2010.

IIDA, I**.,**Ergonomia Projeto e Pro*dução* , Editora Edgard Blucher, 2005.
ISO - INTERNATIONAL ORGANIZATION FOR STANDARDZATION (ISO 5349) - Mechanical Vibration - Measurement and Evaluation of Human Exposure to Hand Transmitted Vibration.Part 1: General Requirements. Part 2: Practical Guidance for Measurement at the Workplace. Genebra, 2001.

MENDES, R., Patologia do Trabalho, Editora Atheneu, 2005

PORTO, Noemia, Associação Nacional dos Magistrados da Justiça do Trabalho, Direitos em Debate, Revista Cipa, n 455,

RAYNAUD, M., On Local AsphyxiaAndSummetricalGengreneof The Extremities, 1969, disponível em <http://archneur.ama-assn.org/>, acesso em junho 2017.

REGAZZI, R. D., XIMENES, G. M., A Importância da Avaliação da Vibração no Corpo Human,. IMETRO, Rio de Janeiro, Brasil, 2005;

SALIBA, T., M., Manual Prático de Avaliação e Controle de Vibração, **PPRA, 3ª Edição, Ed. LTr, 2014**

SCHUTZER, V. M.; SANTOS, J. E. G.; PASCHOARELLI, L. C., Roçadeiras Costais Motorizadas: Análises Estatísticas Das Variáveis Ergonômicas Avaliadas, 2015, 15 ºErgoDesign

SOEIRO, N. S. Vibração e o Corpo Humano: uma avaliação ocupacional. In: 1o Workshop de vibração e acústica, 2011.

VENDRAME, A., C. Vibração Operacional. Revista Proteção. 2009.

VENDRAME, A., C., "Aposentadoria Especial: Como Elaborar O PPP E LTCAT – As novidades do Manual editado pela Resolução INSS nº 600/2017", 2017

VENDRAME, A., C., Vibrações Ocupacionais**,** 2005, disponível em**<**http://www.higieneocupacional.com.br/download/vibracoes_vendrame.pdf**>,** acesso em Junho de 2017.

OSHA, 2005, O impacto do ruído no trabalho, disponível em <https://osha.europa.eu/pt/tools-and-publications/publications/factsheets/57>, acesso em janeiro 2019

CHAPTER 4

ORDERED NONLINEAR SYSTEMS AND APPLICATION IN SHAPE DETECTION

Emerson Vitor Castelani
Doctor in Applied Mathematics
Institution: Department of Mathematics, Universidade Estadual de Maringá (UEM)
Address: Colombo Avenue 5790, Maringá, Paraná, Brazil
E-mail: evcastelani@uem.br

Wesley V. I. Shirabayashi
Doctor in Applied Mathematics
Institution: Department of Mathematics, Universidade Estadual de Maringá (UEM)
Address: Colombo Avenue 5790, Maringá, Paraná, Brazil
E-mail: wvishirabayashi@uem.br

Jesus M. Camargo
Doctor in Applied Mathematics
Institution: Universidade Estadual do Oeste do Paraná (Unioeste)
Address: R. Universitária, 1619, Cascavel, Paraná, Brazil
E-mail: marco.s.camargo@hotmail.com

Jair da Silva
Doctor in Applied Mathematics
Institution: Universidade Federal do Paraná (UFPR), Campus Avançado de Jandaia do Sul
Address: R. Dr. João Maximiano, Centro, Jandaia do Sul, Paraná, Brazil
E-mail: jairmt@gmail.com

André L. M. Martinez
Doctor in Applied Mathematics
Institution: Department of Mathematics, Universidade Tecnológica Federal do Paraná (UTFPR)
Address: Alberto Carazzai Avenue, 1640, Cornélio Procópio, Paraná, Brazil
E-mail: andrelmmartinez@yahoo.com.br

ABSTRACT: This work introduces a novel model for nonlinear systems based on LOVO-type functions, as proposed by Andreani *et al*. [1]. For this model, we present an algorithm that adapts the classical Newton's method for solving nonlinear systems. Typically, Newton's method requires differentiability of the system, but LOVO-based systems are non-differentiable, necessitating this adaptation. Our approach also includes an application in geometric shape detection within binarized images. The primary advantage of this new method is that, for problem classes where the optimal solution of the LOVO problem is zero, our formulation provides the global minimizer of

the LOVO problem. We also present numerical comparisons between our algorithm and existing methods for solving the LOVO problem in the context of shape detection.
KEYWORDS: LOVO functions, nonlinear systems, shape detection.

RESUMO: Este trabalho introduz um novo modelo para sistemas não lineares baseado em funções do tipo LOVO, conforme proposto por Andreani *et al*. [1]. Para este modelo, apresentamos um algoritmo que adapta o método clássico de Newton para resolver sistemas não lineares. Normalmente, o método de Newton requer diferenciabilidade do sistema, mas sistemas baseados em LOVO são não diferenciáveis, necessitando desta adaptação. Nossa abordagem também inclui uma aplicação em detecção de formas geométricas dentro de imagens binarizadas. A principal vantagem deste novo método é que, para classes de problemas onde a solução ótima do problema LOVO é zero, nossa formulação fornece o minimizador global do problema LOVO. Também apresentamos comparações numéricas entre nosso algoritmo e métodos existentes para resolver o problema LOVO no contexto de detecção de formas.

PALAVRAS-CHAVE: Funções LOVO, sistemas não lineares, detecção de formas.

1. INTRODUCTION

Problems of LOVO type (Low Order Value Optimization) constitute an important class of problems in continuous optimization with several applications involved. This class, as well as its variations, are widely studied in [1,2,3,4] and more recent applications are explored in [5] and [6]. LOVO problems can be formulated as follows. Consider $F_i: R^n \to R$, $i = 1, \dots, m$ as continuous functions with continuous derivatives. To each $x \in R^n$, we can order the set $\{F_i(x), i = 1, \dots, m\}$ incrementally. Thus, if the indexes $\{i_k(x), k = 1, \dots, m\}$ denote such order, we have:

$$F_{i_1(x)}(x) \leq F_{i_2(x)}(x) \leq \dots \leq F_{i_m(x)}(x).$$

Given $p \leq m$, the LOVO function is defined by:

$$\bar{S}_p(x) = \sum_{k=1}^{p} F_{i_k(x)}(x), \qquad (1)$$

and the LOVO problem consists in minimizing such function, that is:

$$\min \bar{S}_p(x). \qquad (2)$$

Theoretical results, algorithms and properties related to the problem (2) can be found in [4], are well established in literature and will therefore be omitted here.

We are interested in relating LOVO problem (2) with nonlinear systems represented by functions of LOVO type. Such system will be called *Ordered Nonlinear System (ONS)* and it is defined as follows.

Definition 1. Consider $\Delta_j \subset \{1,2, \dots, p\}, j = 1, \dots, n$ *(naturally* $p \geq n$*), with* $\Delta_k \cap \Delta_j = \emptyset$ *if* $k \neq j$ *and* $\cup_{j=1}^{n} \Delta_j = \{1, \dots, p\}$. *Denoting* $\{i_k(x), k = 1, \dots, m\}$ *ordering mentioned above, we have the following problem:*

$$S_p^1(x) = \sum_{k\,\epsilon\,\Delta_1} F_{i_k(x)}(x) = 0\ S_p^2(x) = \sum_{k\,\epsilon\,\Delta_2} F_{i_k(x)}(x) = 0\ \vdots\ S_p^n(x) = \sum_{k\,\epsilon\,\Delta_n} F_{i_k(x)}(x) = 0 \quad (3)$$

There are important reasons that justify the introduction of this nonlinear system even losing minimizing structure:

- To a class with problems ONS solution corresponds to global minimize to LOVO problem;
- There are no conditions of weak optimality in this type of problem;
- Nonlinear systems do not require, normally, second order derivatives;
- As functions S_p^j are not differentiable, it is possible to approach Quasi-Newton methods and omit the calculus of first derivatives.

The aim of this paper, besides the definition of this class of nonlinear systems, is to present an algorithm based on Newton's method in order to solve this problem as well presenting the potential of this formulation in shape detection. We complement this work with comparisons between our method, the LOVO method presented in [7] and free derivatives methods like Nelder-Mead [8] and Particle Swarm [9].

2. THE ONS MODEL AND LOVO MODEL

A direct examination on the definitions presented shows that $\underline{S_p}(x) = S_p^1(x) + S_p^2(x) + \cdots + S_p^n(x)$. Besides, according to [4], the formulation of the LOVO problem is related to the generalized least square problem. In this context, the ONS formulation can be related to the notion of interpolation. Let us see an example to illustrate the context.

Example 1. Take a set of points $D = \{(t_i, y_i), i = 1, \ldots, 21\}$ so that $t_1 = -1, t_i = t_{i-1} + 0.1, i = 2, \ldots, 21$ and $y_i = 0.85t^2$. Naturally, an interpolation function for this point set is given by $g(t) = 0.85t^2$. Let us suppose that we perturb some of those points, for example, $y_1 = 0.12$, $y_3 = 0.6$, $y_4 = 0.0$, $y_5 = 0.43$, $y_9 = 0.01$, $y_{11} = 0.05$, $y_{14} = 0.38$, $y_{15} = 0.4$, $y_{17} = 0.61$ and $y_{19} = 0.2$. Figure 1 represents this data set.

Figure 1. Scatterplot of perturbed D set

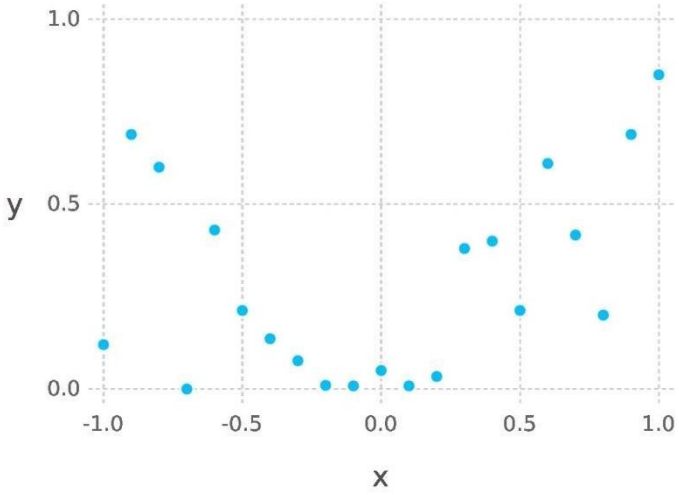

Source: The authors

Note that, as we perturbed 10 points there are 11 of them left to secure the interpolation. This way, in terms given to that moment, we have $m = 21$ and $p = 11$. Presuming that the interpolation function to be determined has the form $\underline{g}(x,t) = xt^2$, we want to find $x \in R$ such that $\underline{g}(x,t_i) = y_i, i \in \{i_1(x), \dots, i_{11}(x)\}$.

Defining $F_i(x) = \left(\underline{g}(x,t_i) - y_i\right)^2$, $i = 1, \dots, m$ and noting that $n = 1$, we have $\Delta_1 = \{1, \dots, p\}$ and consequently the system to be solved consists in an unknown (x) and an equation $(S_p^1(x) = 0)$ where:

$$S_p^1(x) = \sum_{i \in I(x)} \nabla F_i(x) = \sum_{k=1}^{p} \nabla F_{i_k(x)}(x) = \sum_{k \in \Delta_1} \nabla F_{i_k(x)}(x) = 0.$$

In Figure 2 we have the function graphic of $S_p^1(x)$. Note that, in such case, $\underline{S}_p(x) = S_p^1(x)$ and its graphic has many singular points and some possible local minima. When we consider the problem from the viewpoint of the optimization (LOVO model) we are subject to find one of those local minima. When we consider the viewpoint of ONS model, we are interested in finding the intersection of function S_p^1 with the axis x ($s = 0.85$, is the intersection searched for) and therefore, we find out the global minimize of LOVO problems and, also, the interpolator parabola in 11 points with the vertex in the origin.

Figure 2. Graphic of $S_p^1(x)$,

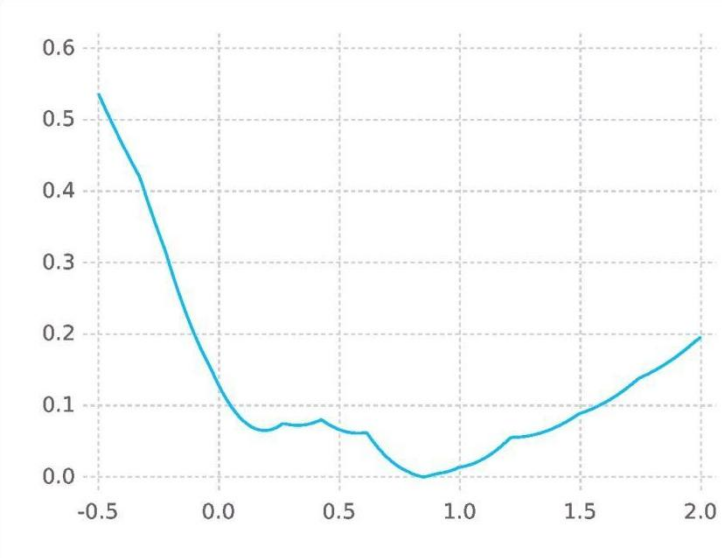

Source: The authors

Figure 2, clarifies two of the aspects mentioned before: the solution of ONS model corresponds to the minimizer of LOVO model and in the ONS solution there is no condition for weak solution.

3. NEW PROPOSAL

To fix ideas, suppose $x = (x_1, x_2)$ and set $\Delta_1 = \{k \in \{1, \dots, p\}; k = 0 \; mod \; 2\}$ and $\Delta_2 = \{k \in \{1, \dots, p\}; k = 1 \; mod \; 2\}$. Thus, the ONS problem is defined by:

$$S_2^1(x) = \sum_{k \in \Delta_1} F_{i_k(x)}(x) = 0 \; S_2^2(x) = \sum_{k \in \Delta_2} F_{i_k(x)}(x) = 0. \tag{4}$$

Note that the nonlinear system above is obtained by considering functions S_1^1 and S_2^2 defined by the ordinations of even and odd sub index (parity in k not in $i_k(x)$, respectively). Denoting $S_2(x) = \left(S_2^1(x), S_2^2(x)\right)$, even if each $F_i(x)$ is differentiable, we may have that S_2 will not be. Thus, an approximation for Jacobian matrix of S_2 will be used.

The method we will explore uses the matrix defined by the Jacobian of fixed sorting as an approximation for the Jacobian matrix. In other words, when we evaluate the function S_p in x, an order is fixed $I(x) = \{i_k(x), k = 1, \dots, p\}$. Thus, in the case of S_2, the approximation for the Jacobian matrix is given by:

$$J^a S_2(x) = [\nabla^a S_2^1(x)\ \nabla^a S_2^2(x)\ ] = [\sum_{k\in\Delta_1} \nabla F_{i_k(x)}(x)\ \sum_{k\in\Delta_2} \nabla F_{i_k(x)}(x)\ ], \quad (5)$$

and in the general case:

$$J^a S_p(x) = [\nabla^a S_p^1(x)\ \nabla^a S_p^2(x)\ \vdots\ \nabla^a S_p^n(x)\ ] = [\sum_{k\in\Delta_1} \nabla F_{i_k(x)}(x)\ \sum_{k\in\Delta_2} \nabla F_{i_k(x)}(x)\ \vdots\ \sum_{k\in\Delta_n} \nabla F_{i_k(x)}(x)\ ].$$

(6)

With this approximation, we can define the ONS method by the following algorithm.

Algorithm 1. Given $x_0 \in R^n, k = 0$ do:

While $\|S_p(x_k)\| \neq 0$ do

Step 1: Calculate $S_p(x_k)$ and $J^a S_p(x_k)$

Step 2: If $J^a S_p(x_k)$ is nonsingular then solve $J^a S_p(x_k)d = -S_p(x_k)$. Else, $d = -S_p(x_k)$.

Step 3: $x_{k+1} = x_k + d$

Step 4: $k = k + 1$

Evidently, the above method corresponds to an adaptation of Newton's method for ONS problem. A good review on Newton's method and variations can be found in [10]. In general, the Step 2 can be solved by different algorithms and it depends on the number of variables. In our context we use Gauss Elimination.

4. NUMERICAL STUDIES

A potential use of ONS model is related to shape detection. In this sense, we concentrate our experiments in this direction. By simplicity, we are presenting the shape detection problems in the context of circles but it can be extended for any shape without big changes.

Circle detection problem. This problem consists in finding a circle in a given binarized image. From mathematical point of view, there is a set $Im =$

$\{(a_i, b_i) \in R^2, i = 1, \dots, m\}$ and we want to find a circle with center $(x_1, x_2) \in R^2$ and radius $x_3 \in R$ that contains *p* of these m points ($p < m$) in Im. From a computer point of view, acclaimed works allow resolving this type of problem via voting strategies, we recommend [11, 12, 13, 14, 15, 16] and [17]. However, this kind of strategy depends on the discretization of the search space, which can be a complicating factor in situations in which there are several parameters to be determined. Consequently, problems shaped by the point of view of optimization or nonlinear systems can represent an alternative. In this sense, an optimization model using LOVO functions was introduced in [7]. This model is defined as follows. Consider $F_i(x) = ((a_i - x_1)^2 + (b_i - x_2)^2 - x_3^2)^2, i = 1, \dots, m.$ If there is a point $C = (c_1, c_2, c_3) \in R^3$ such that for p points in Im, we have $F_i(C) \approx 0$, a circle was detected. Consequently, it is easy to see that the solution C is a global minimize of the LOVO problem:

$$\underline{S}_p(x) = \sum_{k=1}^{p} F_{i_k(x)}(x) = \sum_{k=1}^{p} ((\left(a_{i_{k(x)}} - x_1\right)^2 + \left(b_{i_k(x)} - x_2^2\right)^2 - x_3)^2.$$

In order to validate our approach, an implementation related to Algorithm 1 was compared with an adaptation of Gauss-Newton Method for LOVO problems introduced in [7] which will be called here by Algorithm 2.

Algorithms 1 and 2 were implemented in Julia Language [20] and the derivatives involved in these algorithms were evaluated by automatic differentiation package FowardDiff.jl [21].

Since LOVO problems are non-differentiable, it makes sense to apply algorithms based on free derivative ideas. Consequently, we consider the following algorithms to compare with Algorithm 1.

Algorithm 3. (Nelder-Mead) See, [8].

Algorithm 4. (Pattern Swarm) See, [9].

Both implementation details of Algorithm 3 and 4 can be found in [18], they are implemented in Julia Language and distributed by Optim.jl package [19].

For evaluate and compare the methods we consider a class of test problems artificially generated. These problems were built considering noisy and cluster simulations. The code to generate these problems and the dataset used in tests can be found in https://github.com/evcastelani/ONSmethod.

The implementations were performed using a CPU Intel Pentium(R), G3240 with 3.10GHz and 4Gb RAM memory with Linux Ubuntu Mate 16.04, 64bits. In Table 1, we summarize the results considering the percentage of solved problems (PSP), the percentage of faster solved problem (PFSP), best (Best CPU) and worst (Worst CPU) CPU time in seconds.

Table 1. Numerical results.

Algorithm	PSP	PFSP	Best CPU	Worst CPU
1	97,67%	13,95%	0,021 (s)	0,67 (s)
2	95,35%	23,25%	0,002 (s)	1,50 (s)
3	16,28%	62,8%	0,006 (s)	0,18 (s)
4	67,44%	0%	0,004 (s)	0,45 (s)

Source: The authors

In Figure 3 we highlight the CPU time for each method in each problem until it satisfies the stop criteria. In Figure 4, we show the detection, using Algorithm 1, of a circle with 100 points where 10% were perturbed and 300 outliers were added.

Figure 3. CPU time by problem

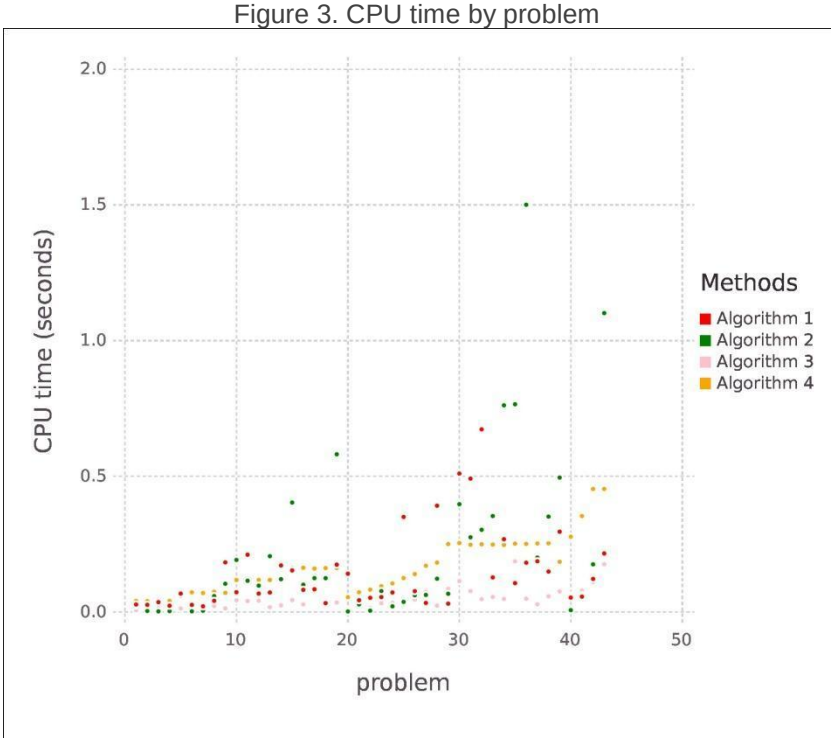

Source: The authors

Figure 4. Example of circle detection using Algorithm 1

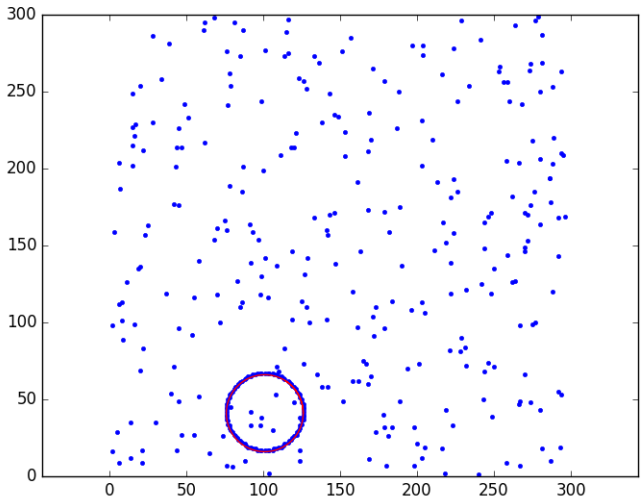

Source: The authors

5. FINAL REMARKS

A direct analysis of the numerical results presented, suggest that the method used is quite promising, since it behaved stably in all tests and was also the most robust. However, we emphasize that the main objective was not to propose a method of solving problems of detection of geometric forms to replace methods consolidated in the literature, but to present nonlinear systems based on LOVO-like functions as well as an adaptation of Newton's method to solve them.

ACKNOWLEDGEMENTS

The authors are grateful to the financial support of the State University of Maringá and Federal University of Paraná.

SUPPLEMENTARY MATERIAL AND/OR ADDITIONAL INFORMATION

Material related to implementation of Algorithm 1 and 2 and all numerical experiments can be found in github repository: https://github.com/evcastelani/ONSmethod.

REFERENCES

[1] ANDREANI, R., DUNDER, C. and MARTÍNEZ, J. M. (2003). Order-Value Optimization: formulation and solution by means of a primal Cauchy method. Mathematical Methods of Operations Research, 58(3): 387-399.

[2] ANDREANI, R., DUNDER C. and MARTÍNEZ, J. M. (2005). Nonlinear programming reformulation of the order-value optimization problem. Mathematical Methods and Operations Research, 61 (3): 365-384.

[3] ANDREANI, R. MARTÍNEZ, J. M., MARTÍNEZ, L. and YANO, F. S. (2008). Continuous optimization methods for structure alignments. Mathematical Programming, 112 (1) : 93-124.

[4] ANDREANI, R., MARTÍNEZ, J. M., MARTÍNEZ, L. and YANO, F. S. (2009). Low Order Value Optimization and applications. Journal of Global Optimization, 43 (1): 1-22.

[5] CARVALHO, E. P., PISNITCHENKO, F., MEZZOMO, N., FERREIRA, S. R. S., MARTÍNEZ, J. M. and MARTÍNEZ L. (2012). Low Order –Value Multiple Fitting for supercritical fluid extraction models. Computers and Chemical Engineering, 40(5): 148-156.

[6] Martínez, J. M. (2012). Generalized order-value optimization. Top, 20(1): 75-98.

[7] ANDREANI, R., CESAR, G., CESAR-JR, R. M., MARTINEZ, J. M., & SILVA, P. J. S. (2007, October). Efficient curve detection using a Gauss-Newton method with applications in agriculture. In Proc. 1st International Workshop on Computer Vision Applications for Developing Regions in Conjunction with ICCV 2007-CVDR-ICCV07.

[8] NELDER, JOHN A. and R. MEAD (1965). "A simplex method for function minimization". Computer Journal 7: 308–313. doi:10.1093/comjnl/7.4.308.

[9] ZHAN, ZHANG, and CHUNG. Adaptive particle swarm optimization, IEEE Transactions on Systems, Man, and Cybernetics, Part B: CyberneticsVolume 39, Issue 6, 2009, Pages 1362-1381 (2009)

[10] DEUFLHARD, P. (2011). Newton methods for nonlinear problems: affine invariance and adaptive algorithms (Vol. 35). Springer Science & Business Media.

[11] DUDA, R. O., & HART, P. E. (1972). Use of the Hough transformation to detect lines and curves in pictures. Communications of the ACM, 15(1), 11-15.

[12] COWART, A. E., SNYDER, W. E., & RUEDGER, W. H. (1983). The detection of unresolved targets using the Hough transform. Computer Vision, Graphics, and Image Processing, 21(2), 222-238.

[13] MURPHY, L. M. (1986). Linear feature detection and enhancement in noisy images via the Radon transform. Pattern recognition letters, 4(4), 279-284.

[14] ILLINGWORTH, J., & KITTLER, J. (1988). A survey of the Hough transform. Computer vision, graphics, and image processing, 44(1), 87-116.

[15] ZIOU, D. (1991). Line detection using an optimal IIR filter. Pattern Recognition, 24(6), 465-478.

[16] CHUTATAPE, O., & GUO, L. (1999). A modified Hough transform for line detection and its performance. Pattern Recognition, 32(2), 181-192.

[17] CHA, J., COFER, R. H., & KOZAITIS, S. P. (2006). Extended Hough transform for linear feature detection. Pattern Recognition, 39(6), 1034-1043.

[18] MOGENSEN *et al*., (2018). Optim: A mathematical optimization package for Julia. Journal of Open Source Software, 3(24), 615, https://doi.org/10.21105/joss.00615.

[19] MOGENSEN *et al*., (2018). Optim.j. JuliaNLSolvers/Optim.jl: Julia v1.0 only release (Version v0.17.0). Zenodo. http://doi.org/10.5281/zenodo.1401127

[20] BEZANSON, J., EDELMAN, A., KARPINSKI, S., & SHAH, V. B. (2017). Julia: A fresh approach to numerical computing. SIAM review, 59(1), 65-98.
[21] Revels, J., Lubin, M., & Papamarkou, T. (2016). Forward-mode automatic differentiation in Julia. arXiv preprint arXiv:1607.07892.

CHAPTER 5

USE OF GRAPHENE AS AN ADDITIVE TO IMPROVE THE MECHANICAL PROPERTIES OF GYPSUM

Adller Ernesto de Lima Ferreira
Master in Materials Science from Universidade Federal do Triângulo Mineiro (UFTM)
Institution: Centro Federal de Educação Tecnológica de Minas Gerais (CEFET-MG)
Address: Araxá, Minas Gerais, Brazil
E-mail: adller.ferreira@cefetmg.br
Orcid: https://orcid.org/0009-0006-1675-1222

Felipe Silva Lima
Master in Aeronautical Infrastructure
Institution: Instituto Tecnológico de Aeronáutica (ITA)
Address: São José dos Campos, São Paulo, Brazil
E-mail: felipe_silvalima@hotmail.com

Paulo de Castro Guetti
Doctor in Structural Engineering from the Universidade Federal de Minas Gerais (UFMG)
Institution: Universidade Federal do Triângulo Mineiro (UFTM)
Address: Uberaba, Minas Gerais, Brazil
E-mail: guettipc@gmail.com

Mario da Luz
Doctor in Materials Engineering from Universidade de São Paulo (USP)
Institution: Universidade Federal do Triângulo Mineiro (UFTM)
Address: Uberaba, Minas Gerais, Brazil
E-mail: mario.luz@uftm.edu.br

Jeferson Aparecido Moreto
Doctor in Materials Engineering
Institution: Universidade de São Paulo (USP)
Address: São Carlos, São Paulo, Brazil
E-mail: jamoreto@usp.br

Rogério Valentim Gelamo
Doctor in Physics from the Universidade Estadual de Campinas (UNICAMP)
Institution: Universidade Federal do Triângulo Mineiro (UFTM)
Address: Uberaba, Minas Gerais, Brazil
E-mail: rogerio.gelamo@uftm.edu.br

ABSTRACT: The aim of this study was to investigate the effects of combining graphene nanoparticles (GNPs) with foundry plaster on the mechanical and morphological properties of mortars. Samples were made from pure gypsum paste (GC - Control Group) and multilayer graphene (MLG). The samples were prepared with

a water/gypsum factor (a/g) of 0.5 and graphene dosages between 0.015 and 0.025% in relation to the mass of gypsum powder. Cubic specimens were made for compression and hardness tests, as well as for diametrical compression tensile tests. The mechanical tests indicated that the dosage with 0.02% graphene showed increases of around 120% in compression and tensile strength at 7 days. The increase can be attributed to the dissipation of internal heat promoted by the graphene, a consequence of the greater production of crystallization nuclei through the increased solubility of the gypsum, in addition to the action of the graphene as a nucleus through the reactivity of its surface with calcium ions, increasing the saturation of the solution. Setting times, consistency, loss of mass due to submersion in water were also analyzed, as well as FTIR and XRD to check for possible chemical alterations. SEM and optical micrographs were used to characterize the morphology and dispersion analysis of the MLG in paste. The results relating to tolerance to the presence of water indicated that the higher the dosage of graphene, the greater the resistance to water, with the best result at a dosage of 0.025% MLG.

KEYWORDS: plaster, gypsum, graphene.

RESUMO: Este trabalho tem como objetivo investigar os efeitos da combinação de nanopartículas de grafeno (MLG) com o gesso de fundição nas propriedades mecânicas e morfológicas de argamassas. Foram confeccionadas amostras de pasta de gesso puro (GC – Grupo Controle) e com multicamadas de grafeno (MLG). As amostras foram preparadas com fator água/gesso (a/g) de 0,5 com dosagens de grafeno entre 0,015 e 0,025% em relação à massa de gesso em pó. Foram confeccionados corpos de prova cúbicos para ensaios de compressão e dureza, bem como para ensaios de tração por compressão diametral. Os ensaios mecânicos indicaram que na dosagem com 0,02% de grafeno, apresentando aos 7 dias aumentos na ordem de 120% para compressão e tração por compressão diametral. O aumento pode ser atribuído a dissipação de calor interno promovida pelo grafeno, consequência da maior produção de núcleos de cristalização através do aumento da solubilidade do gesso, além da atuação do grafeno como núcleo através da reatividade de sua superfície com íons de cálcio aumentando a saturação da solução. Também foram analisados tempos de pega, consistência, perda de massa por submersão em água, além de FTIR e DRX para verificação de possíveis alterações químicas. MEV e micrografias ópticas para caracterização de morfologia e análise de dispersão do MLG em pasta. Os resultados relacionados à tolerância à presença de água indicaram que quanto maior a dosagem de grafeno maior resistência à água é observada, com melhor resultado na dosagem de 0,025% de MLG.

PALAVRAS-CHAVE: pasta, gesso, grafeno.

1. INTRODUCTION

Gypsum has been widely employed in civil construction as pre-molded boards *(drywall*), sealing blocks, coatings, trailers, finishes and details such as sancas and three-dimensional plates [1]. Among the various advantages that gypsum presents can be highlighted its practicality, speed of application, lightness and low production of waste in the construction sites. Despite all the above-mentioned characteristics, the plaster still presents a very low cost when compared to conventional sealing and coatings systems. In addition, gypsum sealing walls and *drywall* plates can be up to 7 times lighter than ceramic block walls, which allows scaling of slimmer structures and foundations, generating savings in cement and steel consumption, which means lower environmental impact [2]. Whereas the cement production process accounts for more than 6% of all CO_2 emitted in the world [3]However, the use of gypsum in the area of civil construction emerges as a possibility of reducing the environmental impact.

Gypsum is a material produced mainly from the calcination of the mineral rock of gypsum, a process in which the raw material (calcium sulfate dihydrate - $CaSO_4.2H_2O$) is pulverized and submitted to temperatures close to 140°C, releasing steam from water into the environment and giving rise to commercial gypsum (calcium sulfate hemihydrate - CaSO4. 1/2H2O) [4]. The hardening (rehydration) process takes place after mixing the commercial plaster with water, in this time interval the plaster becomes temporarily plastic and during the drying process returns to its original form (dihydrate). In this way, it is a reversible process, provided that there is the breaking of the chemical bonds of its crystals and the decontamination of the material, this process has been the object of a study in recycling [5]. Such characteristics mentioned above guarantee the plaster interesting sustainable and recyclable potential. However, despite the advantages of using gypsum, its fragility and intolerance to water discourage its use.

The hydration reaction of the gypsum is exothermic, releasing a large amount of energy in the form of heat. However, the plaster has low thermal conductivity [6] and as the hydration reactions occur, there is the accumulation of heat in the central regions of the paste promoting different conditions of crystallization between the central and peripheral regions of the sample. Thus, the released energy changes the solubility of the plaster, influencing the hydration kinetics [7.8]crystallographic density and

mechanical performance of the material. In other words, it can be considered that the relationship between temperature and solubility of the gypsum alters negatively the crystalline homogeneity, promoting the formation of crystals of different sizes. In order to improve the specific properties of gypsum, such as: absorption into water, adhesiveness, increase and delay in the time of harvesting, chemical additives are used [4]. Recent studies show the influence of cellulose fibers [9.10], TiO_2-based nanoparticulate systems [10], expanded polystyrene, carbonate and silica minerals [11] the mechanical properties of gypsum. Literature [12-14], reported the influence of the incorporation of carbon-based nanoparticles in ceramic agglomerants, revealing an increase in their mechanical resistance and the optimization of their electrical and thermal properties [15.16].

As reported by Silva *et al* [12] and Gdoutos [17]However, the incorporation of nanostructured systems, such as nanofibers, carbon nanotubes and multi-layer graphene, considerably optimizes the mechanical resistance of cement composites. However, the use of graphene in multilayers in systems that receive water as a catalyst is quite challenging. This is due to the fact that graphene exhibits a hydrophobic behavior, which ends up hindering its dispersion and promoting a tendency to agglomerate. The agglomeration process is probably due to the interaction between the multi-layers by Van der Waals forces [18]. The use of surfactants appears as an alternative for the optimization of dispersion, however, they negatively affect the elasticity and tensile strength module of the material [19].

Nanostructured systems based on multi-layers of graphene (MLG) have extraordinary properties, such as high tensile strength, compression strength, high thermal and electrical conductivity [20-22]. For this reason, graphene has been studied in Physics, Chemistry, Materials Science and Engineering, Medicine etc. [23-25]. Furthermore, research shows that the incorporation of MLG into ceramic matrices generates modifications in the crystallization mechanisms, produces denser nuclei and the production of more mechanically and durably resistant mortars.

In this study, we propose to conduct an innovative and applied research to study the influence of the addition of MLG on the mechanical properties of gypsum. The system was characterized morphologically and structurally via scanning electron microscopy (SEM), optical microscopy (OM), Fourier transform infrared spectroscopy (FTIR) and X-ray diffraction (DRX). The objective of this study was also to verify the

consistency of the plaster containing LCM and the initial and final gripping times by means of Vicat assays. Resistance of the MLG-containing gypsum to water was verified via mass loss analysis after the submersion process.

2. EXPERIMENTAL

2.1 MATERIALS

In the present work, the casting gypsum, type β, with fineness module of 1.11, unit mass of 713.06 kg/m³ and multi-layers of graphene (MLG) was used. The multilayers of MLG were obtained via synthesization by exfoliation of natural graphite flakes donated by the Brazilian company of Grafite Ltda and according to the reference [26] of which the thickness is in the range of 1 to 10 nm [27.28]The MLG powder was dispersed in ultrasonic bath for a period of 2 h in deionised water. Afterwards, the MLG dispersed in water was added to the plaster, by means of a mixing process. It is important to mention that the amount of water used to disperse the MLG was discounted in the amount of kneading water, thus keeping the water/gypsum factor constant at 0.50.

2.2 PREPARATION OF TEST PIECES

Six different tracks of gypsum pulp were made, according to the methodology proposed by Brazilian Standard ABNT/NBR-12129:2019 "Plaster for civil construction - Determination of mechanical properties". Percentages of 0% of MLG were adopted, i.e., reference sample (GC), 0.15% (150MLG), 0.175% (175MLG), 0.2% (200MLG) and 0.25% (250MLG) in relation to the mass of the gypsum powder. For all samples the water/gypsum ratio (a/g) was 0.5. The MLG dispersed in deionised water (see *section 2.1*) was incorporated into the kneading water, adding together the a/g factor of 0.5 at a temperature of 25 oC. Cubic test bodies with 50 mm edge were obtained for the compression tests according to ABNT/NBR-12129:2019. For the diametral compression tensile strength tests (see Standard ABNT/NBR7222:2011), the test pieces were made in cylindrical form with a diameter of 5 cm and a height of 10 cm.

The samples were obtained at room temperature, unmolded after 3 h and conditioned under room temperature and humidity until the date of breakage.

2.3 ANALYSIS OF NORMAL CONSISTENCY AND START AND END TIMES OF HARVESTING

The normal consistency analyzes and the start and end times of harvesting were performed according to ASTM-C472 - "Standard Test Methods for Physical Testing of Gypsum, Gypsum Plasters and Gypsum Concrete". The hydration curves were obtained from temperature measurements of samples allocated in an adiabatic box. For this, a system composed of a thermocouple and Arduino was used and the measurements took place for a period of 3 h.

2.4 MASS LOSS TESTS

The mass loss tests were carried out in order to verify the influence of the hydrophobic properties of the LCM on the resistance of the gypsum in relation to the action of the water. To do so, the samples were submerged in distilled water and room temperature for a period of 2 hours. In the first instance, the samples were dried in an oven at a temperature of 80 °C for a period of 24 hours. After this procedure, the masses were measured using a balance (BEL/M-503) and submerged in distilled water again. After 2 hours of submersion, the samples were re-dried in an oven at a temperature of 80 °C until stabilization. After the stabilization of their masses, measured at room temperature, the difference was made between the initial and final dry masses, measured as a percentage.

2.5 MORPHOLOGICAL ANALYSIS

The morphological properties of gypsum containing different amounts of MLG were verified via scanning electron microscopy, using an EGF-SEM JEOL 7001F microscope equipped with an Oxford EDX element detector of the Technological Institute of Aeronautics, Brazil. The optical microscopy technique (TESCAN/VEGA-3) was used to check the distribution of MLG particles in the gypsum paste.

2.6 STRUCTURAL ANALYSIS

To investigate the chemical structure of the prepared composites, infrared Fourier Transform (FTIR) spectroscopy was used. The FTIR spectra were obtained using the Agilent Cary 640 spectrometer using the diffuse reflection mode with Pike Veemax II accessory. The spectra were performed in the range of 4000 to 500 cm^{-1}, with resolution of 4 cm^{-1}. The samples used for FTIR analyzes were obtained from fragments taken from the inside of mechanically tested test specimens and aged over 120 days. X-ray diffraction (DRX) analyzes were performed using a Shimadzu XRD-6100 diffractometer in the range of - 6° to 80° (2θ) with scanning speed of 1°/min. Both analyzes were carried out at the Federal University of the Minas Gerais Triangle (UFTM), Uberaba, Brazil.

2.7 TENSILE STRENGTH AND COMPRESSION TESTS

The compression and tensile strength tests were carried out using digital servo-hydraulic press (Contenco/HD200T), with a maximum load capacity of 2000 kN. The compression tests were determined following the protocols described by the Regulatory Agency ABNT/NBR-12129:2019 "Plaster for civil construction - Determination of mechanical properties", using a loading rate of 0.2 ± 0.1 MPa/s; The tensile strength was measured following the procedures described by ABNT/NBR7222:2011 "Concrete and mortar - Determination of the tensile strength by diametrical compression of cylindrical test bodies" with a loading rate of 0.05 ± 02 MPa/s. Compression resistance was analyzed at ages 1, 3 and 7 days and tensile strength at ages 1 and 7 days. Following the guidance of adopted standards, at least 3 test pieces were tested for each batch in each age range, and the resistance considered was the average of these samples. The maximum allowed variation between the individual mechanical resistance of each sample and the mean of the results was 15%.

3. RESULTS & DISCUSSIONS

3.1 MORPHOLOGICAL ANALYSIS

Figures 1 (a- c) show the images that were obtained via MO for the reference sample (GC), 225MLG and 250MLG, respectively. It is noted that there was no significant difference in the amount and size of the pores. As regards the distribution of MLG, a trend of agglomeration in the 250MLG sample can be observed. As described in the *material & methods* section, in the present study, low concentrations of MLG were chosen to facilitate their dispersion in water. Probably, the agglomeration visualized at 250MLG is due to the inefficiency of the ultrasound system for this concentration, since for all samples the amount of water used in the solution was 200g.

Figure 1. Images obtained via optical microscopy (500 x magnification), **a)** GC sample, **b)**[1] **Sample 225MLG with good dispersion, (450 x magnification)Astra 250MLG with cluster.** The black arrows indicate MLG and clusters, respectively.

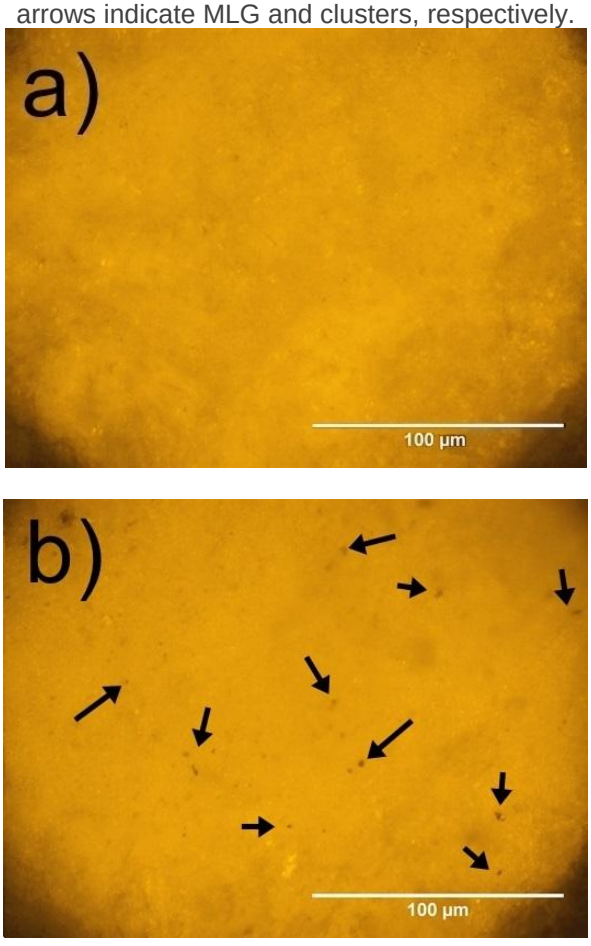

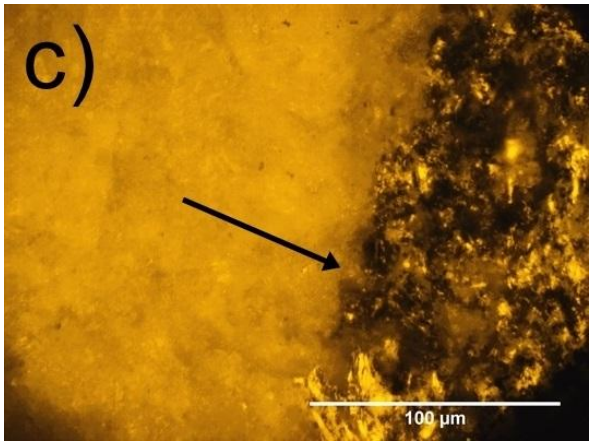

Source: The authors.

Figures 2 (a - c) show the micrographs obtained via MEV for the GC, 225MLG and 250MLG samples. A difference in the size of the crystals and the porosity of the samples is perceived. The GC sample (see Fig. 2 (a)) had average dimensions of 1.46 µm and length 5.45 µm. The sample 225MLG (Fig. 2 (b)) showed a higher density of crystals with smaller unit dimensions (mean diameter of 0.95 µm and length 4.94 µm). As reported by the literature [29.30], the increase in the density of crystals is directly related to the improvement of mechanical properties [31] and a decrease in water absorption [30]. The sample 250MLG (Fig. 2 (c)) showed crystals of similar diameters to GC (~1.3 µm) and average length of 8.23 µm.

Figure 2. Images obtained via VME with a magnification of 5kx, **a)** GC sample, **b)** Sample 225MLG and c)Astra 250MLG.

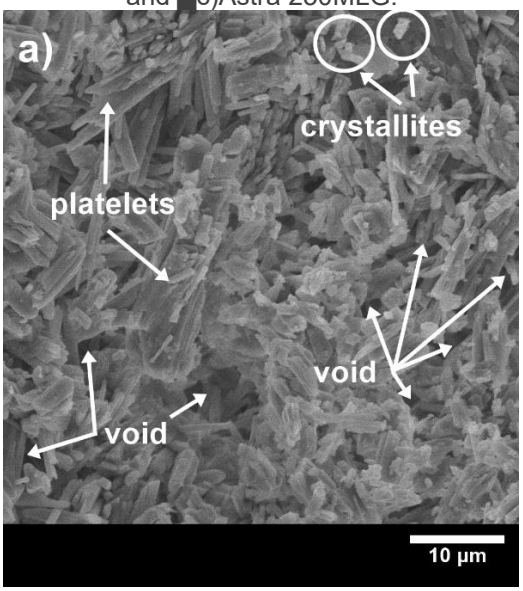

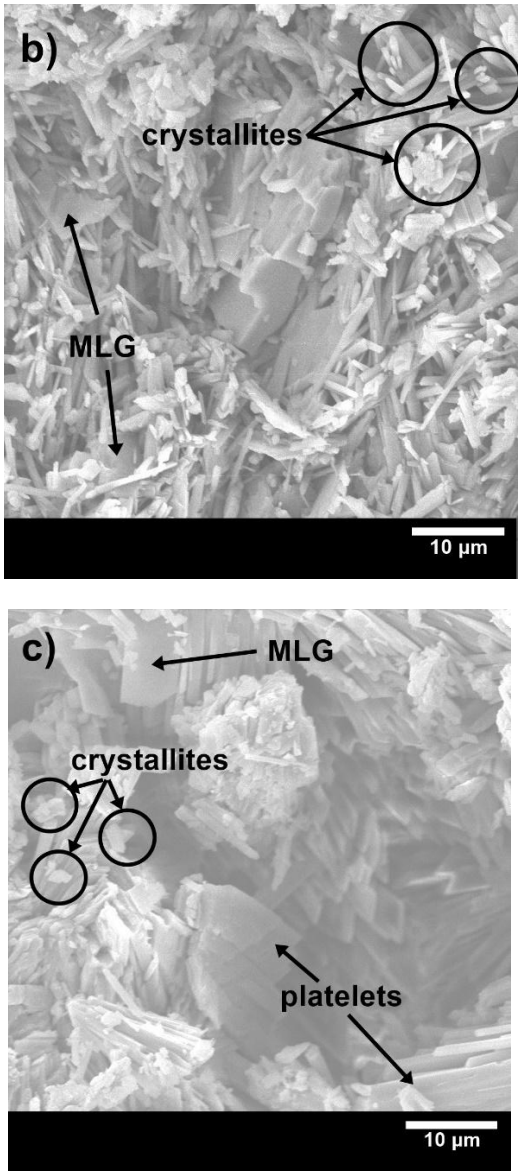

Source: The authors.

3.2 CONSISTENCY, CATCH TIMES AND CALORIMETRY

Table 1 presents the start and end grip times for the GC, 150MLG, 175MLG, 200MLG, 225MLG, and 250MLG samples, respectively. As can be verified, with the exception of the sample 225MLG, all the others had start and end times of grip lower than GC. As reported in other studies [32.33] the decrease in the time of catching is an indication of greater nucleation and crystalline activity. In this way, the more crystallization nuclei, the greater the number of crystals and the smaller their unit dimensions [34].

Table 1. Initial and final gripping times for the samples considered in this paper.

	Pick-up times (h:min:s)		
Samples	Start of Handle (T1)	End of handle (T2)	Q2-Q1
GC	12:16:35 a.m.	12:21:20 a.m.	12:04:45 a.m.
150MLG	12:11:40 a.m.	12:17:28 a.m.	12:05:47 a.m.
175MLG	12:13:05 a.m.	12:21:15 a.m.	12:08:10 a.m.
200MLG	12:11:30 a.m.	12:17:20 a.m.	12:05:50 a.m.
225MLG	12:19:35 a.m.	12:26:20 a.m.	12:06:45 a.m.
250MLG	12:12:23 a.m.	12:16:45 a.m.	12:04:22 a.m.

Source: The authors.

The 225MLG sample presented start and end times higher than GC, indicating a slower crystallization, which can be explained by the solubility of the gypsum related to the hydration temperature. Simply put, the amount of energy that is injected into the system ends up acting as a catalyst for hydration reactions.

Optimizing material crystallization rate and increasing the solubility of gypsum [35.36]. However, this phenomenon is observed up to a temperature of approximately 50 °c. From this temperature value the solubility of the gypsum decreases. Thus, it is suggested that the 225mlg sample distributed trapped energy to the gypsum pulp, allowing mobility of the ca^{+2} so_4^{2} ions and slowing the handle. Figure 3 shows the hydration curve for gc, 175mlg, 225mlg and 250mlg samples, respectively. It is noted that the 225mlg and 250mlg samples showed lower temperature values in the calorimetric analyzes, suggesting that the mlg acts as an energy sink and, in fact, the graphene acts as a good thermal conductor [37]. Considering the end of the handle, the samples containing MLG show higher values of temperature, between 60-65 ºC, indicating greater crystalline activity in the period. It is emphasized that the method has different gripping times than the Vicat apparatus method due to pseudoadiabatic conditions, which alter the solubility of the material, in this case the times serve to determine the periods of the curve.

Figure 3. Hydration curve for GC, 175MLG, 225MLG and 250MLG samples.

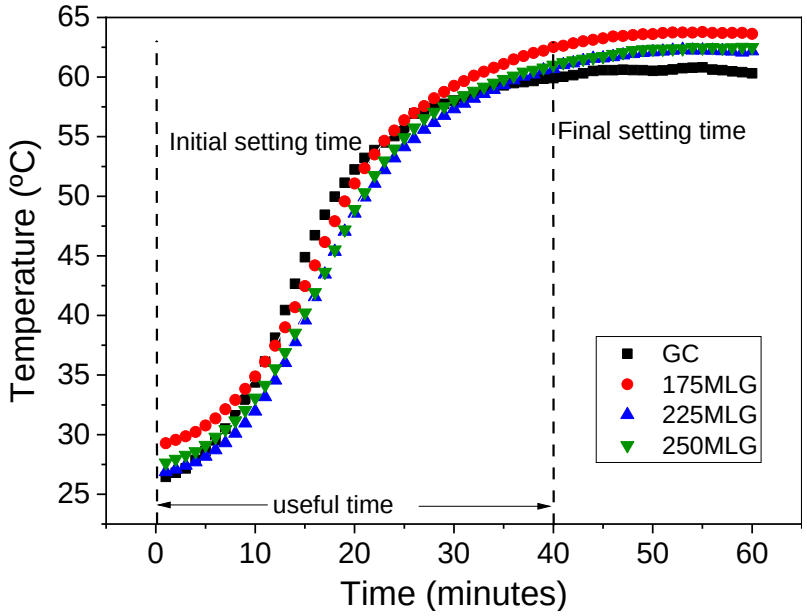

Source: The authors.

3.3 FTIR RESULTS

FTIR spectra for GC and GC containing MLG, in the range of 4000 to 500 cm^{-1} are shown in Figure 4. At the first moment, one can observe a very great similarity between the spectra of the samples studied, indicating that the addition of graphene did not interfere in the physical-chemical properties of the specimens. In addition, bands referring to the sulfate group are noted and centered at 1250 cm-1, 1005 cm-1, 600 cm^{-1}, 670 cm-1, 450 cm-1 and 420 cm-1 [38-41]. The bands centered on 3620 cm^{-1} and 3640 cm^{-1} [38.42], 1620 cm^{-1} [43] and 3200 cm^{-1} refer to water. Light bands centered at 1460, 2850 and 2915 cm^{-1} are associated with C-H [38], identified in the experimental tracks possibly by the presence of LCM.

Figure 4. FTIR spectra for GC and GC containing MLG, in the ranges (a) 4000 to 2000 cm^{-1} and (b) 2000 to 500 cm^{-1}.

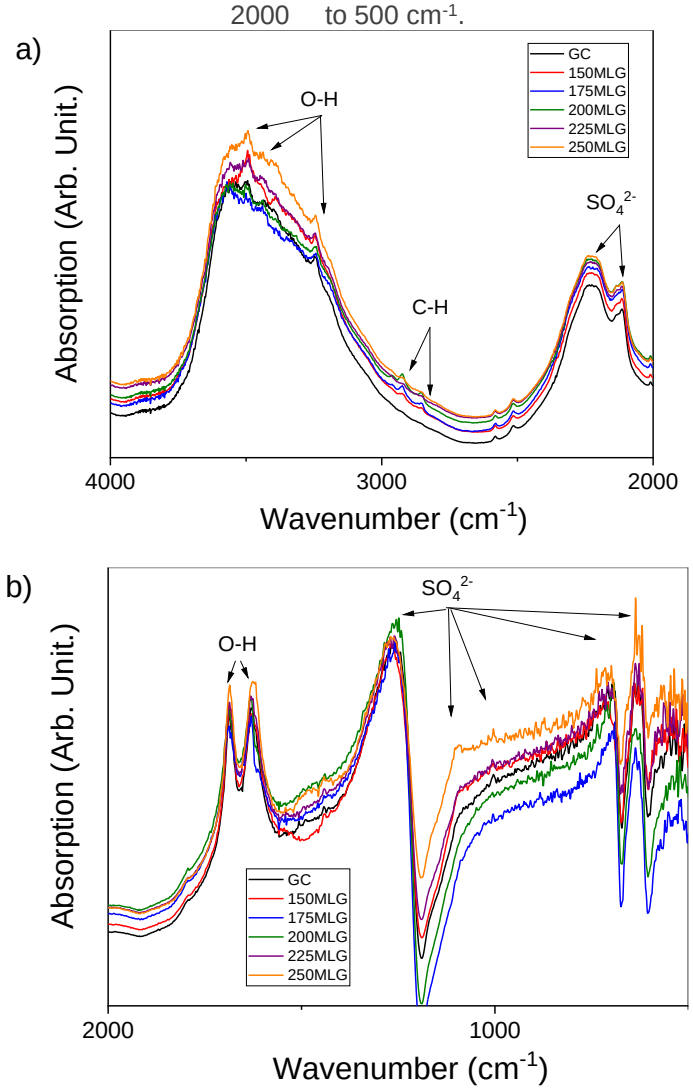

Source: The authors.

3.4 DRX RESULTS

The DRX technique was used in the characterization of the GC, 150MLG, 175MLG, 200MLG, 225MLG and 250MLG samples. The experimental and simulated spectra are shown in **Figure 5**. The simulated spectrum corresponds to phase $CaSO_4 \cdot 2H_2O$[44.45] , also known as gypsum and with a monoclinic structure (space group C12/c1). As can be verified in **Figure 5**, the gypsum phase is present in all the specimens studied. All the peaks present can be related to the monoclinic phase, with the exception of one single reflection observed at $2\theta \sim 25°$ for samples containing MLG. This peak was indexed as belonging to phase β-$CaSO_4$ [46]. Transformations between these phases are common in hydration reactions of gypsum [47]. However,

as this phase is not present in the control sample (GC), it may be suggested that the presence of LCM may interfere with the hydration mechanisms of the plaster in question. As the concentrations of MLG used in the present study are extremely small and are below the detection limit of the equipment used, no peak was observed. No variation in the network parameters was observed for the $CaSO_4 \cdot 2H_2O$ phase, which leads to the conclusion that there is no chemical reaction between this phase and the MLG, which is acting only as an aggregate to the composite material.

Figure 5. Control group (GC) X-ray diffratograms and for composites containing MLG. The spectrum also shows the simulated diffraction for the gypsum phase ($CaSO_4 \cdot 2H_2O$) [1], predominant in the gypsum used. The black arrow shows the presence of phase β-$CaSO_4$.

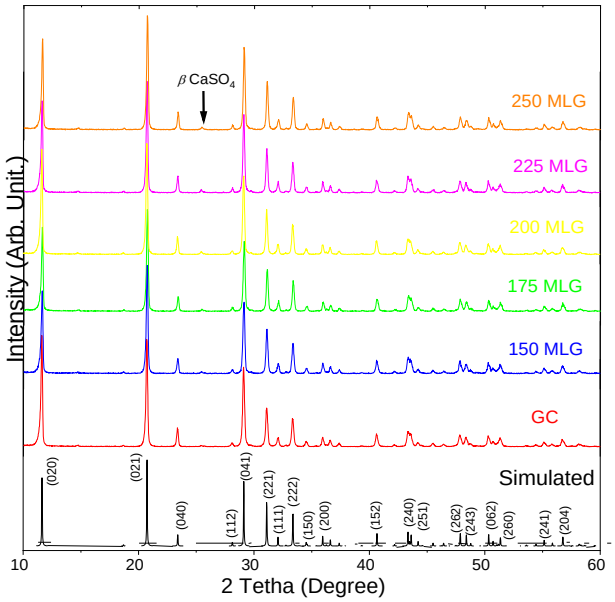

Source: The authors.

3.5 LOSS OF MASS THROUGH SUBMERSION IN WATER AND CONSISTENCY

Plaster is a soluble material, and when exposed to water tends to incorporate it, weakening the bonds between the crystals by capillary pressure. The more intense the interactions between the surfaces of the crystals and the smaller the porosity of the solid body, the more resistant to the action of the water the material will be [30.48]. The process of hydrating the gypsum during the so-called induction period also has an influence on the water tolerance of the hardened material [49]. It was observed that the higher the graphene dosage used in the gypsum paste, the lower the average mass loss (see **Figure 6(a)**). The 250MLG sample lost about 36.4% less mass than the sample made without the additive. Samples containing MLG may be suggested to have

higher crystalline density and higher intergranular interaction than the GC sample, which led to lower mass loss. The hydrophobicity of graphene can make it difficult for water to penetrate the pores of the gypsum and, in this way, keeps its structure more aggregated in comparison with the reference material, preventing the detachment of material.

As for consistency, it was observed that the MLG did not influence the properties of the folder (Figure 6(b)).

Figure 6. a) Results of mass loss by total submersion in water and **b)** Consistency results.

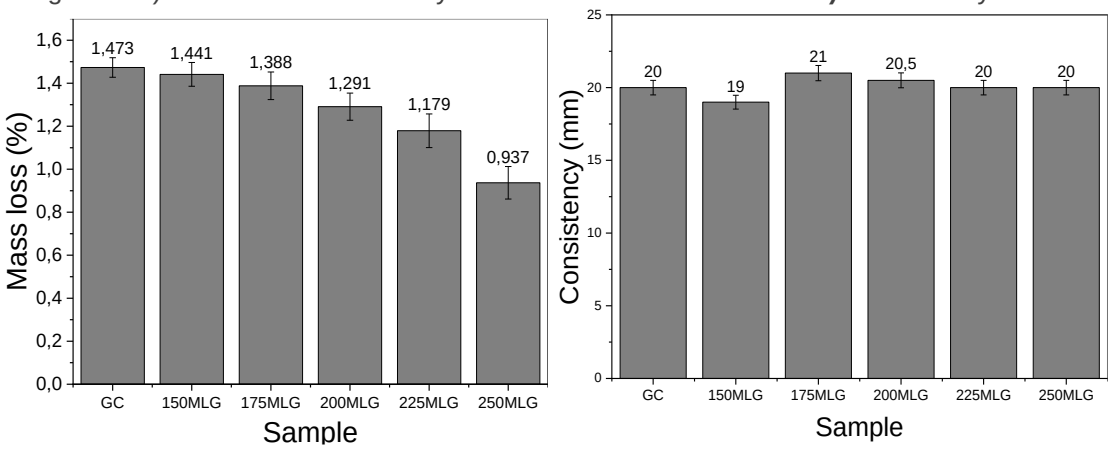

Source: The authors.

3.6 TENSILE AND COMPRESSION TESTS

The results of compressive and tensile strength at the age of 1, 3 and 7 days are presented in Table 2 and in Figure 7.

Table 2. Mean resistance to axial compression (MPa) ± standard deviation

Age (days)	GC	150MLG	175MLG	200MLG	225MLG	250MLG
1.	2.87±0.14	2.87±0.14	2.47±0.12	2.37±0.12	2.20±0.11	3.35±0.17
3.	2.83±0.14	2.90±0.15	3.07±0.15	3.45±0.17	2.45±0.12	3.33±0.17
7	3.03±0.15	3.03±0.15	3.17±0.16	6.73±0.34	5.10±0.26	5.37±0.27

Source: The authors.

Figure 7. Axial compressive strength for pastes with different MLG dosages as a function of time (top plot), and relative variation from the sample without MLG (σ_{co}).

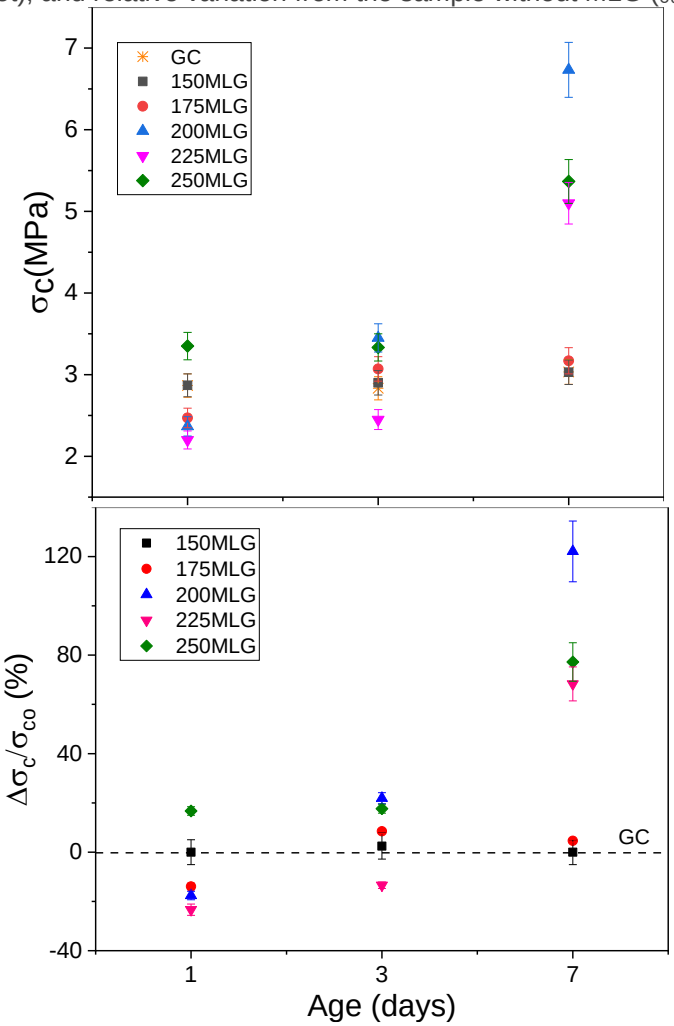

Source: The authors.

From the results of the compression resistance, it is noted that the amount of graphene in the proportion of 0.015% (150MLG) does not affect the process of crystallization of the gypsum and, consequently, in its resistance to compression at the ages considered. The values shown in Figure 7 are consistent with the results obtained in the fresh state of the gypsum samples, which indicated a similar behavior between 150MLG and sample GC. In the 0.0175% MLG dosage (sample 175MLG), one can suggest modest influence of graphene on the mechanical behavior of the plaster.

At the first age tested, samples 175MLG, 200MLG and 225MLG showed lower performance than GC. In the MEV images (Figure 2), one can observe crystals with smoother surfaces and well-defined corners in the samples with MLG. These features may indicate that the crystals were formed in greater time, providing greater unit density, which contributes to ultimate mechanical strength [50]. On the other hand,

crystals formed in small spaces of time are porous and appear spongy[50], similar to the crystals of the GC reference sample (Figure 2(a)). In this context, it may be suggested that the performance observed in the early age is due to the higher rate of GC crystallization at that time, since its crystals developed in shorter time. It may also be suggested that the heat distribution promoted by graphene may have affected the degree of solubility of the gypsum, since the action of temperature alters the material's catching time, and above 50º C the solubility ratio of the hemihydrate and dihydrate diminishes, causing the delay of the catching time and crystallization, increasing the mobility of calcium and sulfate ions as the temperature of the medium increases [7.35,36]. Resumption of resistance gains is observed in experimental samples from 3 days of age, which indicates long-term crystalline activity, which is consistent with the hydration curve (Figure 3), where higher temperatures can be observed after the end of sampling with LGM. As for the results at 7 days, it is observed for the sample 200MLG high performance, about 122% higher than GC at the same age. The 225MLG sample showed a performance 38.13% higher than the GC at 7 days of age, and the lowest performance among all samples at the first age tested (23.25% lower than GC). These results are consistent with the observed catch time for this sample, since the experimental 225MLG band was the only one to present start and end times of catch higher than the control sample, indicating slower crystallization than the other bands.

The 250MLG sample showed higher compression resistance than the others at the age of 1 day, this may have occurred due to the influence of agglomerated graphene, as can be observed in metallographic microscopy (Figure 1(c)). It can be inferred that the graphene cluster may have acted like a crystal, which aided in the gain of resistance at the age of 1 day, and that the heat dissipation effects promoted by the MLG were attenuated due to poor dispersion. The 250MLG sample presented 76.92% better performance than the GC at 7 days, performance lower than the 225MLG. It is believed that the trend of MLG clumping has affected the results, since the dispersion of MLG in paste has been compromised.

Table 3: Mean tensile strength by diametral compression (MPa) ± standard deviation

Age (days)	GC	150MLG	175MLG	200MLG	225MLG	250MLG
1.	1.6±0.08	1.7±0.09	1.75±0.09	1.55±0.08	1±0.05	1.7±0.09
7	1.6±0.08	1.6±0.08	3.3±0.17	3.55±0.18	3.1±0.16	3.03±0.15

Source: The authors.

Figure 8. Diameter compression tensile strength for pastes with different MLG dosages as a function of time (top plot), and relative variation with respect to the sample without MLG (σ_{TO}).

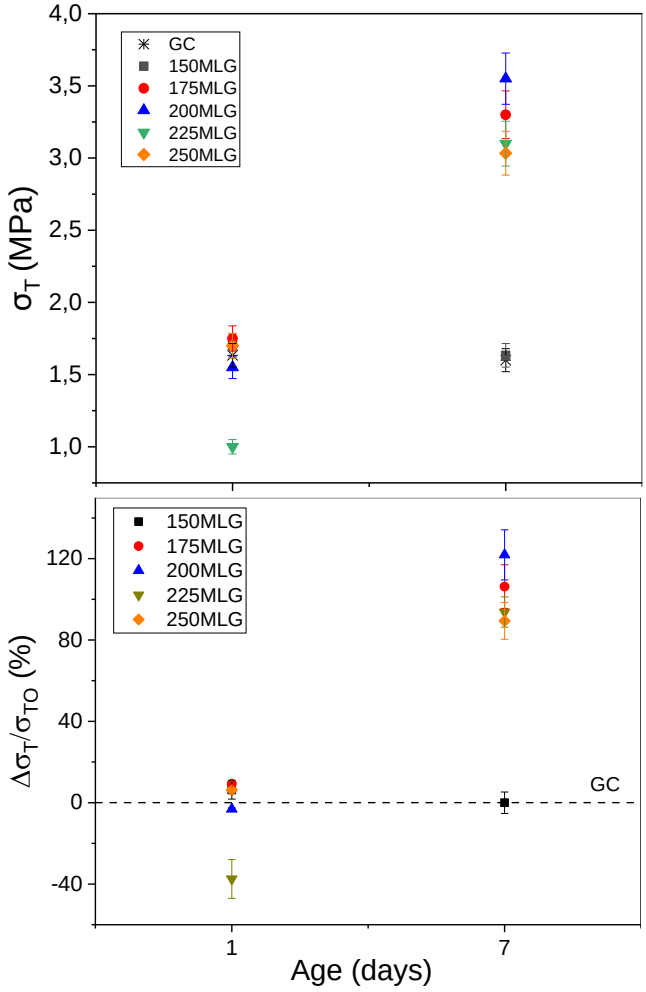

Source: The authors.

At traction, it is observed that at the first age, of 1 day, all tracks performed similar results, except 225MLG, which is in line with the idea of slow crystallization. It is noted by the graph of Figure 8, that the 150MLG sample presented results practically identical to the reference sample GC, as well as occurring in the results of compression and consistency, which reinforces the theory that in this dosage the MLG does not influence in any significant way the fluidity and the mechanical properties of the material. At 175MLG, different from the one observed in the compression results, 106.25% better performance was noted than the GC at 7 days, indicating that this

dosage of MLG acted as an amplifier of tensile strength at this age. Although the compression performance was not significantly higher than the GC to 175MLG, a reduction in grip times was observed, indicating a change in crystal activities. Graphene may be suggested to have a greater influence on tensile strength than on the compression of plaster.

The 200MLG sampling range showed at 7 days performance about 120% superior to GC, as seen in the axial compression results.

The 225MLG and 250MLG samples showed similar resistance at 7 days, being higher than GC and lower than 200MLG.

4. CONCLUSIONS

The use of graphene associated with gypsum proved to be efficient, optimizing its mechanical resistance to traction and compression by about 120% at 7 days in the dosage of 0.02% in relation to the mass of gypsum powder. Graphene is believed to have promoted internal heat dissipation, allowing for a higher degree of hydration in peripheral regions of the paste, promoting higher crystalline density and crystals with better morphological properties. The MLG may also have acted as a crystallization nucleus, increasing the saturation of Ca^{2+} ions through reactivity with the graphene surface.

The MLG used, obtained from natural graphite, has a low cost and production time and is used in extremely low quantities. In this way, starting from a low added value additive, it is possible to encourage the use of gypsum on a larger scale as an option to cement-based compounds, contributing towards sustainability through the reduction of energy consumption and the emission of gases produced by the cement industry.

REFERENCES

[1] R.X. Magallanes-Rivera, C.A. Juarez-Alvarado, P. Valdez, J.M. Mendoza-Rangel, Modified gypsum compounds: An ecological-economical choice to improve traditional plasters, Constr. Build. Mater! 37(2012) 591-596. https://doi.org/10.1016/J.CONBUILDMAT.2012.07.054.

[2] M. V Borrachero, J. Payá, M. Bonilla, J. Monzó, The use of thermogravimetric analysis technique for the characterization of construction materials, J. Therm. Anal. Calorim. 91(2008) 503-509. https://doi.org/10.1007/s10973-006-7739-3.

[3] G.C. Isaia, A.L.G. Gastaldini, Environmental an economic perspectives of concrete with high mineral addition content: a case study, Ambient. Built. 4 (2004) 19-30. https://doi.org/14158876.

[4] C.A.M. Baltar, F. de F. Bastos, A.B. Luz, Gipsita, in: F.A.F. Lins (Ed.), Mineral Rocks Ind. Uses and Specifications, 2nd ed., Rio de Janeiro, 2008: pp. 1689-1699.

[5] H.R. Geraldo, SM Pinheiro, J.S. Silva, H.M.C. Andrade, J. Dweck, J.P. Gonçalves, G. Camarini, Gypsum plaster waste recycling: A potential environmental and industrial solution, J. Clean. Prod 164(2017) 288-300. https://doi.org/10.1016/J.JCLEPRO.2017.06.188.

[6] AJ. De Korte, H.J.H. Brouwers, A.C.J. De, Calculation of thermal conductivity of gypsum plasterboards at ambient and elevated temperature, FIRE Mater. Fire Mater. 34 (2010) 55-75. https://doi.org/10.1002/fam.1009.

[7] G.A. Hulett, L.E. Allen, THE SOLUBILITY OF GYPSUM., J. Am. Chem. Soc. 24 (1902) 667-679. https://doi.org/10.1021/ja02021a007.

[8] A.E. Charola, J. Pühringer, M. Steiger, Gypsum: a review of its role in the deterioration of building materials, Environ. Geol. 52(2007) 339-352. https://doi.org/10.1007/s00254-006-0566-9.

[9] L. Senff, G. Ascensão, V. Ferreira, M. Seabra, J.A. Labrincha, Development of multifunctional plaster using nano-TiO 2 and distinct particle size cellulose fibers, Energy Build. 158 (2017). https://doi.org/10.1016/j.enbuild.2017.10.060.

[10] L. Rosato, M. Stefanidou, G. Milazzo, F. Fernandez, P. Livreri, N. Muratore, L.M. Terranova, Study and evaluation of nano-structured cellulose fibers as additive for restoration of historical mortars and plasters, Mater. Today Proc. 4 (2017) 6954-6965. https://doi.org/10.1016/j.matpr.2017.07.025.

[11] E. Perlova, M. Platonova, E. Bondarenko, I. Togo, A. Tereshchenko, A. Fikfak, Nano Filled Façade Plasters to Increase Durability of Building and Structures, Mater. Sci. Forum. 871(2016) 76-83. https://doi.org/10.4028/www.scientific.net/MSF.871.76.

[12] A.R. Silva, P. de Castro Guetti, M.S. da Luz, F. Nightingale, R.V. Gelamo, Enhanced properties of cement mortars with multilayer graphene nanoparticles, Constr. Build. Mater! 149(2017) 378-385. https://doi.org/10.1016/j.conbuildmat.2017.05.146.

[13] K. Gong, Z. Pan, A. Habibnejad Korayem, L. Qiu, D. Li, F. Collins, C. Wang, W. Duan, Reinforcing Effects of Graphene Oxide on Portland Cement Paste, J. Mater. Civ. Eng. 27 (2015) A4014010. https://doi.org/10.1061/(ASCE)MT.1943-5533.0001125.

[14] M.S. Morsy, S.H. Alsayed, M. Aqel, Hybrid effect of carbon nanotube and nano-clay on physico-mechanical properties of cement mortar, Constr. Build. Mater! 25 (2011) 145-149. https://doi.org/10.1016/J.CONBUILDMAT.2010.06.046.

[15] D.D.L. Chung, Carbon materials for structural self-sensing, electromagnetic shielding and thermal interfacing, Carbon N. Y. 50(2012) 3342-3353. https://doi.org/https://doi.org/10.1016/j.carbon.2012.01.031.

[16] L. Hou, J. Li, Z. Lu, Y. Niu, J. Jiang, T. Li, Effect of nanoparticles on foaming agent and the foamed concrete, Constr. Build. Mater! 227 (2019) 116698. https://doi.org/10.1016/j.conbuildmat.2019.116698.

[17] E.E. Gdoutos, M.S. Konsta-Gdoutos, P.A. Danoglidis, S.P. Shah, Advanced cement based nanocomposites reinforced with MWCNTs and CNFs, Front. Struct? Civ. Eng. 10(2016) 142-149. https://doi.org/10.1007/s11709-016-0342-1.

[18] S. Parveen, S. Rana, R. Fangueiro, A Review on Nanomaterial Dispersion, Microstructure, and Mechanical Properties of Carbon Nanotube and Nanofiber Reinforced Cementitious Composites, J. Nanomater. 2013 (2013). https://doi.org/10.1155/2013/710175.

[19] D.G. Papageorgiou, I.A. Kinloch, R.J. Young, Graphene/elastomer nanocomposites, Carbon N.Y. 95 (2015) 460-484. https://doi.org/10.1016/J.CARBON.2015.08.055.

[20] (D) Chen, L. Tang, J. Li, Graphene-based materials in electrochemistry, Chem. Soc. Rev. 39 (2010) 3157-3180. https://doi.org/10.1039/b923596e.

[21] C. Lee, X. Wei, J. Kysar, J. Hone, Measurement of the Elastic Properties and Intrinsic Strength of Monolayer Graphene, Science. 321(2008) 385-388. https://doi.org/10.1126/science.1157996.

[22] W. Extraordinary Physical Properties of Functionalized Graphene, Small. 8 (2012) 2138-2151. https://doi.org/10.1002/smll.201200104.

[23] K. Novoselov, A. Geim, S. Morozov, D. Jiang, Y. Zhang, S. Dubonos, I. Grigorieva, A. Firsov, Electric Field Effect in Atomically Thin Carbon Films, Nat. Mater! 6 (2004)

[24] D.A.C. Brownson, D.K. Kampouris, C.E. Banks, Graphene electrochemistry: fundamental concepts through to prominent applications, Chem. Soc. Rev. 41 (2012) 6944-6976. https://doi.org/10.1039/C2CS35105F.

[25] G. Lota, T.A. Centeno, E. Frackowiak, F. Stoeckli, Improvement of the structural and chemical properties of a commercial activated carbon for its application

in electrochemical capacitors, Electrochim. Minutes. 53(2008) 2210-2216. https://doi.org/https://doi.org/10.1016/j.electacta.2007.09.028.

[26] L.G.B. Machuno, A.R. Oliveira, R.H. Furlan, A.B. Lima, L.C. Morais, R.V. Gelamo, Multilayer graphene films obtained by dip coating technique, Mater. Res. 18 (2015) 775-780. https://doi.org/10.1590/1516-1439.005415.

[27] F. Nightingale, R. Gelamo, R. Amici, A. Rodrigues Vaz, S. Moshkalev, Low contact resistivity and strain in suspended multilayer graphene, Appl. Phys! Hey, Lett. 97(2010) 253104. https://doi.org/10.1063/1.3528354.

[28] R. Khare, R. Gelamo, M. More, D. Late, C. Rout, Enhanced field emission of plasma treated multilayer graphene, Appl. Phys! Hey, Lett. 107 (2015) 123503. https://doi.org/10.1063/1.4931626.

[29] A.M. Hincaipe, M.A. Cincotto, Effect of grip retarders on the hydration mechanism and the microstructure of construction plaster, Ambient. Built. 1 (1997) 7-16.

[30] H. Ahmadi Moghadam, A. Mirzaei, Comparing the effects of a retarder and accelerator on properties of gypsum building plaster, J. Build. Eng. 28 (2020) 101075. https://doi.org/https://doi.org/10.1016/j.jobe.2019.101075.

[31] E.M. Gartner, Cohesion and expansion in polycrystalline solids formed by hydration reactions — The case of gypsum plasters, Cem. Comp. Res. 39 (2009) 289-295. https://doi.org/10.1016/J.CEMCONRES.2009.01.008.

[32] A.J. Lewry, J. Williamson, The setting of gypsum plaster, J. Mater. Sci. 29 (1994) 6085-6090. https://doi.org/10.1007/BF00354546.

[33] (J) Hao, G. Cheng, T. Hu, B. Guo, X. Li, Preparation of high-performance building gypsum by calcining FGD gypsum adding CaO as crystal modifier, Constr. Build. Mater! 306 (2021) 124910. https://doi.org/https://doi.org/10.1016/j.conbuildmat.2021.124910.

[34] M. Uchymiak, E. Lyster, J. Glater, Y. Cohen, Kinetics of gypsum crystal growth on a reverse osmosis membrane, J. Memb. Sci. 314 (2008) 163-172. https://doi.org/https://doi.org/10.1016/j.memsci.2008.01.041.

[35] W.L. Marshall, R. Slusher, Thermodynamics of Calcium Sulfate Dihydrate in Aqueous Sodium Chloride Solutions, 0-110°1,2, J. Phys. Chem. 70 (1966) 4015-4027. https://doi.org/10.1021/j100884a044.

[36] Q. Coquard, R. Boistelle, L. Amathieu, P. Barriac, Hardness, elasticity modulus and flexion strength of dry set plaster, J. Mater. Sci. 29 (1994) 4611-4617. https://doi.org/10.1007/BF00376285.

[37] (A) Dey, A. Chroneos, N.S.J. Braithwaite, R.P. Gandhiraman, S. Krishnamurthy, Plasma engineering of graphene, Appl. Phys! Rev. 3 (2016) 21301. https://doi.org/10.1063/1.4947188.

[38] G. Anbalagan, S. Mukundakumari, K. Murugesan, S. Gunasekaran, Infrared, optical absorption, and EPR spectroscopic studies on natural gypsum, Vib. Spectrosc. 50 (2009) 226-230. https://doi.org/10.1016/j.vibspec.2008.12.004.

[39] H.H. Adler, P.F. Kerr, Variations in infrared spectra, molecular symmetry and site symmetry of sulfate minerals, Am. Mineral. 50 (1965) 132-147.

[40] (D) Blaney, T. Mccord, Indications of sulfate minerals in the Martian soil from Earth-based spectroscopy, J. Geophys. Res. 100(1995) 14433-14441. https://doi.org/10.1029/95JE00224.

[41] C. Cooper, J. Mustard, Spectroscopy of Loose and Cemented Sulfate-Bearing Soils: Implications for Duricrust on Mars, Icarus. 158 (2002) 42-55. https://doi.org/10.1006/icar.2002.6874.

[42] Y.I. Ryskin, The Vibrations of Protons in Minerals: hydroxyl, water and ammonium, Infrared Spectra Miner. 4 (1974) 0. https://doi.org/10.1180/mono-4.9.

[43] V. Seidl, O. Knop, M. Falk, Infrared studies of water in crystalline hydrates: gypsum, CaSO4·2H2O, Can. Mr. Chem. 47 (1969) 1361-1368. https://doi.org/10.1139/v69-223.

[44] M. Atoji, R.E. Rundle, Neutron Diffraction Study of Gypsum, CaSO42H2O, J. Chem. Phys! 29 (1958) 1306-1311. https://doi.org/10.1063/1.1744713.

[45] (J) Boeyens, V. Icharam, Redetermination of the crystal structure of calcium sulphate dihydrate, CaSO4.2H2O, Zeitschrift Für Krist. 217 (2002) 9-10. https://doi.org/10.1524/ncrs.2002.217.jg.9.

[46] F. Hawthorne, R.B. Ferguson, Anhydrous sulphates. II. Refinement of the crystal structure of anhydrite. Miner. 13 (1975) 289-292.

[47] L. Ritterbach, P. Becker, Temperature and humidity dependent formation of CaSO4·xH2O (x = 0...2) phases, Glob. Planet. Change. 187(2020) 103132. https://doi.org/10.1016/j.gloplacha.2020.103132.

[48] M. Singh, M. Garg, Relationship between mechanical properties and porosity of water-resistant gypsum binder, Cem. Comp. Res. 26 (1996) 449-456. https://doi.org/10.1016/S0008-8846(96)85032-0.

[49] W.M. Kanno, Mechanical properties of high strength gypsum, University of São Paulo, 2009.

[50] A.A Barbosa, A. V. Ferraz, G.A. Santos, Chemical, mechanical and morphological characterization of gypsum obtained at Araripe, PE, Brazil, Ceramica. 60(2014) 501-508. https://doi.org/10.1590/s0366-69132014000400007.

CHAPTER 6

COMBINED EFFECT OF STRESSORS ON LEARNING EFFICIENCY

Alexsandro dos Santos Silveira
Doctor in Knowledge Engineering
Institution: POLO Laboratórios, Departamento de Engenharia Mecânica, Universidade Federal de Santa Catarina
Address: Florianópolis, Santa Catarina, Brazil
E-mail: alex@polo.ufsc.br

Gertrudes Aparecida Dandolini
Doctor in Production Engineering
Institution: IGTI Laboratório, Departamento de Engenharia do Conhecimento, Universidade Federal de Santa Catarina
Address: Florianópolis, Santa Catarina, Brazil
E-mail: gertrudes.dandolini@ufsc.br

João Artur de Souza
Doctor in Production Engineering
Institution: IGTI Laboratório, Departamento de Engenharia do Conhecimento, Universidade Federal de Santa Catarina
Address: Florianópolis, Santa Catarina, Brazil
E-mail: jartur@gmail.com

Christian Johann Losso Hermes
Doctor in Mechanical Engineering
Institution: POLO Laboratórios, Departamento de Engenharia Mecânica, Universidade Federal de Santa Catarina
Address: Florianópolis, Santa Catarina, Brazil
E-mail: hermes@polo.ufsc.br

ABSTRACT: The present paper is aimed at assessing the combined effect of different stressors (e.g., carbon dioxide, temperature, illuminance and noise) on the quality of learning environments. The combined effects caused by the stressors present in the environment were evaluated in terms of two response variables, namely the loss in the knowledge flow and the learning efficiency, where the latter estimates the learning performance by means of the time spent on a given intellectual activity compared to the same task performed in an ideal environment. A fully controlled experimental environment was designed and constructed to carry out tests and correlate individual and combined effects through a factor analysis. In total, 24 different rooms were evaluated to validate this study. For each room, it was possible to evaluate and classify the impact of stressors on the knowledge flow and learning efficiency. The largest loss of knowledge flow observed was 35%, which represents 21 minutes of time lost in a 60-minute task.

KEYWORDS: learning environment, stressors, carbon dioxide, temperature, illuminance, noise.

RESUMO: Este artigo apresenta uma avaliação do efeito combinado de diferentes agentes estressores (*e.g.*, dióxido de carbono, temperatura, iluminância e ruído) sobre a qualidade de ambientes de aprendizagem. Os efeitos combinados causados pelos estressores presentes no ambiente foram avaliados em termos de duas variáveis resposta: a perda no fluxo de conhecimento e a eficiência de aprendizagem, a qual estima o desempenho dos ocupantes através do tempo gasto em determinada atividade intelectual em comparação com a mesma tarefa quando realizada em um ambiente ideal de referência. Um ambiente experimental totalmente controlado foi projetado e construído para a realização dos testes e correlação dos efeitos individuais e combinados por meio de uma análise fatorial. No total, foram avaliadas 24 salas diferentes para validar o estudo. Para cada sala foi possível avaliar e classificar o impacto dos agentes estressores no fluxo de conhecimento e na eficiência de aprendizagem dos ocupantes. Verificou-se que a maior perda de fluxo de conhecimento observada foi de 35%, o que representa 21 min de tempo perdido em uma tarefa de 60 min de duração.

PALAVRAS-CHAVE: ambiente de aprendizagem, agentes estressores, dióxido de carbono, temperatura, iluminância, ruído.

1. INTRODUCTION

Effective learning and innovation environments must provide their occupants with the conditions to reach their full potential as apprentices. Therefore, the maximum learning efficiency depends not only on the initial knowledge, the learning rate or the motivation of the sender to transmit knowledge, but also on the quality of the environment where the learners are inserted. For example, (Lorsch and Abdou, 1994), evaluated the impact of temperature by looking at the productivity of the occupants of a given environment, with an increase of up to 15% in productivity when the ambient air conditioner was turned on. In general, the literature indicates that productivity decreases by about 2% for each 1°C above 25°C, which confirms that thermal comfort has a strong influence on the occupant's performance. The relevance of this theme is explored by Lippman (2010) in his work at the *Center for Effective Learning Environments (CELE*), which seeks to answer the following question: "Can the physical environment impact the learning environment?" According to the author, it is necessary to understand the value of creating learning and innovation environments that are not only aesthetically pleasing, but also meet satisfactory levels of quality. For (Kamarulzaman *et al.,* 2011), occupants more satisfied with the physical environment are more likely to produce better results at work. In the same vein, (Lan *et al*., 2011) state that an enabling working environment is a fundamental requirement for occupants to perform their activities more effectively. These authors also emphasize that the quality of indoor environments has a significant effect on user comfort and performance in performing a given task, noting that the determination of the optimal degree of environment quality is still unknown. *Thus, evaluating the influences of environmental stressors and their combined effects on the quality of learning can provide many benefits to the organization.* According to (Been de *et al.,* 2014), among the stressors that affect cognitive performance, working memory and productivity, temperature, noise and lighting can be highlighted.

Furthermore, it is mandatory to understand the phenomena involved by means of experimental analyzes followed by scientific proof, in order to assist professionals, such as engineers and architects, in the design of suitable rooms, having as priority the learning efficiency of the occupants. In the same direction, it is possible to point to some bodies, such as the GBC (*Green Building Council*) as part of a global movement

aiming at an adequate assessment of well-being and health in buildings, as pointed out in the works of (Fisk, 2012; Ambrose, 2016). In addition, as noted by (Lipczynska *et al.,* 2018), occupants reporting complaints of thermal discomfort have low productivity.

Another important fatora in this analysis is the concentration of carbon dioxide present in the environment. According to (Satish *et al*., 2012), through testing at concentration levels of 600, 1,000, and 2500 ppm, they found a significant decrease in decision-making-related employee performance as the CO_2 level increases. In turn, (Garcia Neto *et al.,* 2019), evaluated different levels of CO_2 concentration in a classroom, pointing out the need for air renewal during classes, even with partial occupancy capacity, to values that exceed the limit of 1000 ppm. Also according to these authors, an excess concentration of CO_2, with values around 1600 ppm, can jeopardize the quality of the lessons, as well as the learning of the pupils, who tend to lose their concentration and disperse with greater ease. Such a result was endorsed by (Lee *et al.,* 2022), who evaluated such an effect through neural responses, concluding that the increased concentration of CO_2 seriously affects activities related to the central lobe and thus productivity, working memory, as well as vision. Such observations are corroborated by an alarming fact, obtained from the ENEM statistics published in the Brasindoor Schools Forum in 2024, which shows that polluted air has reduced student performance by approximately 2%.

In general, studies found in open literature treat the effects of stressors in isolation, without considering their interactions. In addition, there is a lack of a consistent and properly validated mathematical correlation against reliable experimental data obtained through controlled experiment, which is able to predict the individual and combined effects of stressors, CO_2 concentration, temperature, illuminance and noise on learning efficiency and knowledge flow. Presenting such a correlation is the objective of this study.

2. METHODS

The experiment was conducted at an educational and innovation institution located in the southern region of Brazil. The experimental trials were conducted in a controlled environment, as shown in Figure 1, where a measuring station (1) was

installed in the geometric center of the room with the function of monitoring and recording the variables of interest. In addition, the environment was built in order to allow the monitoring and control of noise (2), temperature (3) and illuminance (4) at different levels. Furthermore, it is possible to monitor and control the level of CO_2 within this environment through the air renewal system (5 and 6).

The environment consists of a cooling system, an air circulation system (fans and *dampers*), a heating system (electrical resistors) and a water reservoir for humidity control. The internal ambient temperature is measured through five temperature sensors through the measuring station (1). The control is performed through a PI controller (proportional and integral), which acts on the electrical resistances positioned at the output of the air conditioning system, which is operating continuously. Air velocity at any point within the room does not exceed 0.25 m/s, emulating a typical natural convection situation. A specific data acquisition system was developed for this application, as well as supervisory *software* to monitor and record variables of interest. The instrument, now at the functional stage, also makes it possible to store all the variables of interest for analyzing and postprocessing the data.

Figure 1. Schematic representation of the experimental apparatus.

Source: Authors

The tests were carried out with specialists from different areas of knowledge, such as engineers from the area of automation, electrical and mechanical. The group was submitted to performing activities of the daily work itself under different environmental conditions, previously defined through a factorial project, as illustrated

in Table 1, in order to evaluate the effect of the internal environment on the performance of the user in terms of time spent per activity.

Five dimensions of analysis were chosen from a meeting with the specialists with the intention of capturing the main means of search for knowledge (knowledge node) in the execution of activities related to the development of a given project within the unit, namely: use of computational tools; reading activity; writing activity; experimental activity and interpersonal interaction.

The pre-defined exposure limits determined by the existing standards have been respected, avoiding any unhealthy conditions for the occupants. In all, eight experiments were carried out, comprising different levels of temperature, noise and illuminance and the five dimensions of analysis mentioned, totaling 40 experimental trials. It is important to note that the first condition corresponds to an ideal environment, henceforth represented by k_{ideal}, which indicates zero interference of the environment in the learning of the occupant.

Table 1. Experimental Matrix.

Experiments [indexes]	**Temperature [°C]**	**Noise [dB]**	**Illuminance [Lux]**
1.	1.	1.	1.
2.	1.	1.	0
3.	1.	0	1.
4.	1.	0	0
5	0	1.	1.
6	0	1.	0
7	0	0	1.
8	0	0	0
		Levels assessed → 2	
	Temperature	1.	20 °C
		0	35 °C
	Noise	1.	40 dB
		0	100 dB
	Illuminance	1.	500 Lux
		0	30 Lux

Source: Authors

The adopted method is illustrated by the flowchart shown in Figure 2, which starts with the choice of the internal environment, and continues with the measurement and normalization of the independent variables, so that they can be included in the correlation obtained through the processing of the factorial experiment presented in Table 1.

The data was then processed to calculate the combined effect of temperature, noise, illuminance and CO_2 so as to obtain two dependent variables, x_1^{tni} and x_2^{cd} the former being responsible for concatenating the effects of temperature, noise and illuminance, while the latter introduces the effect of CO_2 into the formulation. These variables were later grouped into the form of the factor K_s, which represents the combined effect of variables independent of the internal environment. With the value of K_s at hand, the next step is to calculate the learning efficiency η_l, which indicates how much the environment is affecting the learning process compared to an ideal environment. Finally, a control logic for the independent variables can be activated to mitigate the stressor agent by correcting the reference error in order to reclassify the environment.

Figure 2. Methodology for assessing a given internal environment.

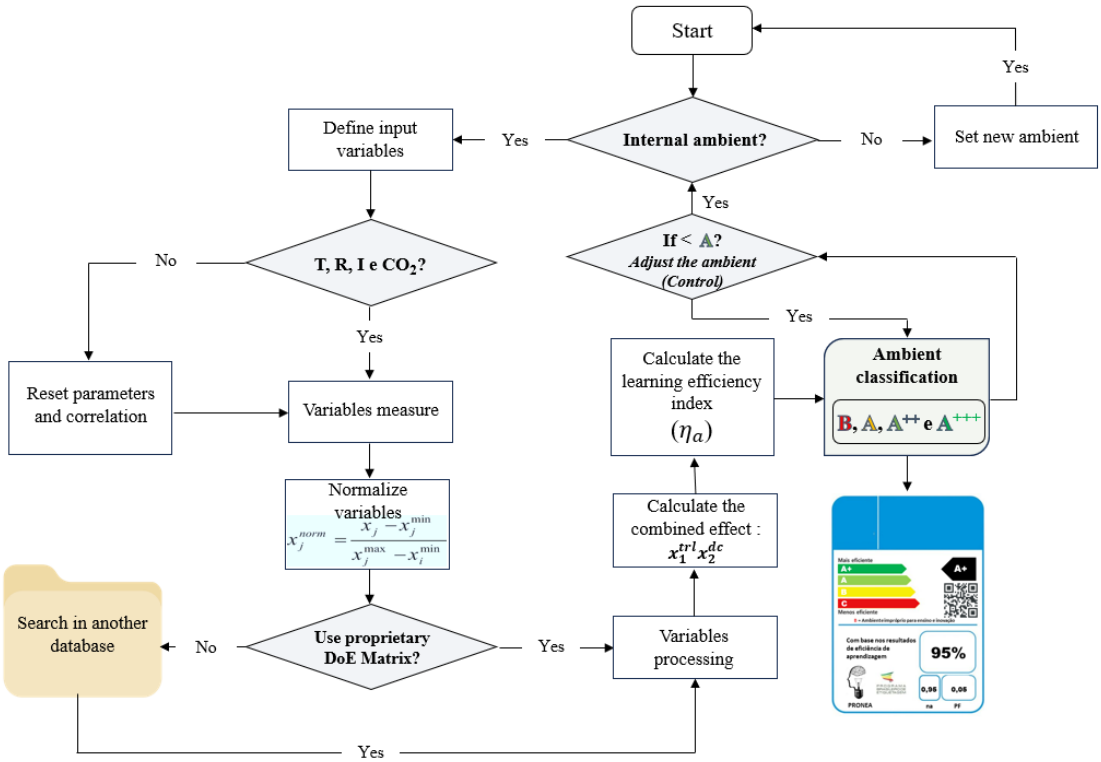

Source: Authors

The variable x_1^{tni} represents, in the proposed model, an environmental quality index responsible for synthesizing the combined effect of temperature, noise and illuminance on learning efficiency and knowledge flow through a single indicator. For this parameter, the maximum value indicates an optimal environment. On the other hand, the reduction of this index can be considered proportional to the increase in

losses caused by non-idealities resulting from the variation of the independent parameters. In order to evaluate the combined effect of temperature, noise and illuminance on learning efficiency and knowledge flow, considering a constant-valued sample for each independent variable, the following adjustment was obtained from the factorial design:

$$x_1^{tni} = j_0 + j_1 T + j_2 N + j_3 I - j_4 TN - j_5 TI - j_6 IN + j_7 TNI \qquad (1)$$

where terms with indices 4 to 7 indicate the combined effects of temperature, illuminance and noise.

The term x_2^{cd} in turn evaluates the effect of carbon dioxide concentration in the environment and is calculated using the following equation:

$$x_2^{cd} = -j_8\, CO2 + j_9 \qquad (2)$$

The effects of x_1^{tni} and x_2^{cd} were grouped into the factor K_s, which expresses the combined effects of the independent variables:

$$K_s = x_1^{tni}\, x_2^{cd} \qquad (3)$$

In order to evaluate the influence of K_s the system on the learning curve, the following exponential model was adopted (Anzanello, 2004):

$$C(t) = 1 - exp(-K_s t) \qquad (4)$$

For this particular case, C_i=0 (Initial Knowledge is null) and C_{max}=1 (Maximum Unitary Knowledge) were adopted. It should be noted that equation (4) describes the behavior of a first-order system, represented by:

$$C(t) = 1 - exp(-t/\tau) \qquad (5)$$

In this type of system, it τ has an interpretation of mathematical nature, receiving the nickname of "time constant", to the point that, when it t assumes a value equal to

τ, the dependent variable, $C(t)$, reaches 63.2% of the maximum admitted value. Thus, by comparing equations (4) and (5), one realizes that, for the particular case analyzed, the time constant is given by:

$$\tau = \frac{1}{K_s} \qquad (6)$$

Such an interpretation allows a visualization of the effect of the environment on the learning curve through the time spent on a given task. In other words, the execution time of an activity in a real environment will always be longer than in an ideal environment. In order to develop a consistent metric, it is important to take as a reference an ideal condition, where it K_s^{ideal}represents the combined effect of losses from the ideal environment $(K_s^{ideal} = 1)$, while K_s^{real}indicating the combined effect of losses from the real environment $(0 \leq K_s^{real} < 1)$. Figure 3 illustrates the behavior of the ideal environment (curve in blue, $K_s = 1$) and a hypothetical real environment (curve in red, $K_s = 0{,}4$) in a comparative way through the analytical model developed.

Figure 3. Comparison of learning efficiency in an ideal and real environment.

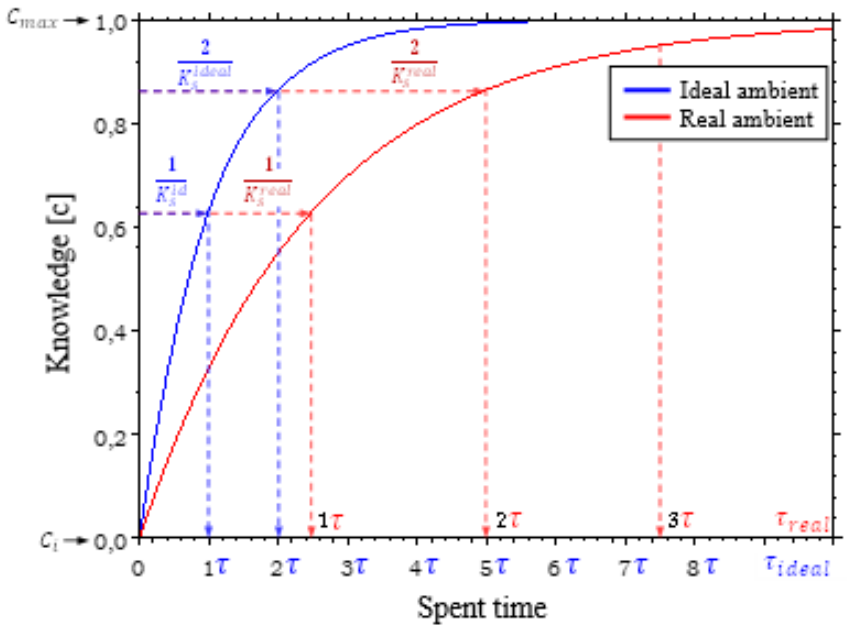

Source: Authors

According to the behavior observed in Figure 3, as an example, considering a period of 2τ for both environments, i.e. a knowledge retention of 86.4%, it is possible

to observe that, in the real environment, the time to acquire the same amount of knowledge is greater, which occurs due to the effect of the losses caused by the environmental stressors. Additionally, the values obtained for the parameters $K_s^{ideal}$and K_s^{real}can be used to calculate knowledge flows under the respective conditions using the following equations:

$$\dot{C}_{ideal} = K_s^{ideal}(C_{max} - C) \qquad (7)$$

$$\dot{C}_{real} = K_s^{real}(C_{max} - C) \qquad (8)$$

With both ideal and real flow, it is possible to calculate the loss in the knowledge flow, represented by the indicator φ_s, as follows:

$$\varphi_s = \frac{\dot{C}_{ideal} - \dot{C}_{real}}{\dot{C}_{ideal}} = 1 - \frac{\dot{C}_{real}}{\dot{C}_{ideal}} = 1 - \frac{K_s^{real}}{K_s^{ideal}} \qquad (9)$$

Finally, to represent the influence of the quality of the environment on learning, a learning efficiency was introduced from the following expression:

$$\eta_l = \frac{\tau_{ideal}}{\tau_{real}} \qquad (10)$$

Learning efficiency can be understood as the percentage of time actually spent learning, to the point that values below the unit indicate that a portion of time has been added to the process due to the combined effects of environmental stressors. With the calculated knowledge flow loss and learning efficiency values, it is possible to classify the environment on a discrete scale (specifically developed for this research) ranging from A^{+++} to B, with A^{++} rating being equivalent to an environment where the user can achieve maximum learning efficiency, while B rating indicates that the environment is unsuitable for learning. Classifications between A^{+++} and B need adjustment, and can be corrected through the adaptive controller developed in this work, incorporated in the supervisory software and shipped in the measuring station.

3. RESULTS AND DISCUSSION

In all, 24 rooms were evaluated. The indicator of loss of knowledge flow, represented by φ_s, denotes in percentage terms the waste of time in each activity caused by the impact of stressors on the environment. In other words, this indicator can show the organization the additional time spent performing the activities as compared to the time that would be required for the same activity in an ideal environment.

Figure 4 quantifies the impact of stressors for each room analyzed. Using the methodology presented, it is possible to observe that the 1L room was classified as unsuitable for learning activities, indicating that the measured values extrapolated the limits established in the model. The 2L room, in turn, received a B rating index, as a loss of knowledge flow in the order of 35% (21 min of time wasted on a 1 h activity) was observed. In addition, it can be noted that 1D, 2D, 3L, 4L, 4D, 9, 11, 12, 13, 14, 15, and 17 rooms obtained type A classification, which indicates a loss of knowledge flow in the order of 25%, while 3D, 5, 6, 7, 10, 16, 18, and 19 rooms were rated A^{++}, with a loss of knowledge flow of about 10%. Finally, the best classifications, with A^{+++}, or that is to say, those that show the least influence of the environment on the flow of knowledge, were rooms 8 and 20.

In relation to the influence of each stressor agent on the environments, it is possible to observe the predominance of the noise in the majority of the evaluated rooms. The CO_2 index also stands out in rooms 2L, 12, 13, 15 and 17, being observed a direct correlation with the reduction in area and the increase in the number of occupants, which is aggravated due to the absence of a suitable system for air renewal. The temperature showed higher values in rooms 5, 9, 12, 19 and 20, which are mainly attributed to the generation of thermal load by the equipment (*hardware*) present in the room. Finally, illuminance was the stressor agent with the least impact in most of the rooms analyzed, as shown in Figure 4.

Figure 4. Assessment of the impact of environmental stressors on each of the 24 evaluated environments.

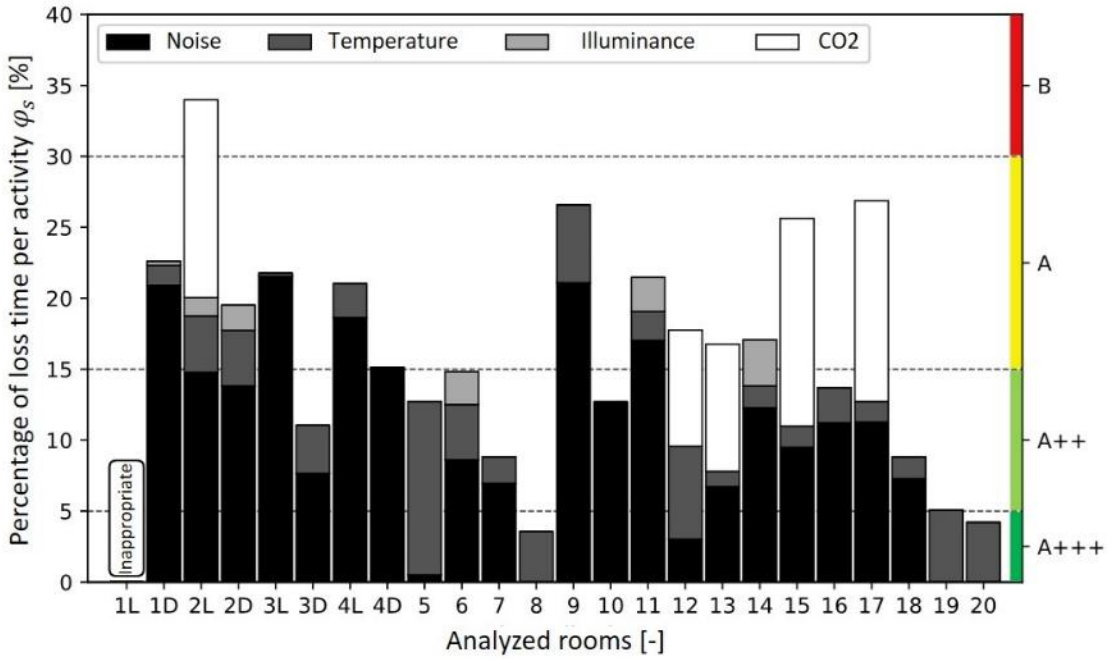

Source: Authors

In relation to the general classification of the rooms analyzed, Figure 5 presents, in descending order, the values of the learning efficiencies (η_l) obtained for each environment. It is observed that only two rooms obtained the maximum rating (A^{+++}), with values above 95%. Next, eight rooms were classified as A^{++}, 12 rooms as A, while only one was classified as B. From the point of view of the application, it is possible to observe that the scale presents sufficient resolution to distinguish and qualify the different environments of the same organization.

Figure 5. Map of learning efficiency considering the 24 environments assessed.

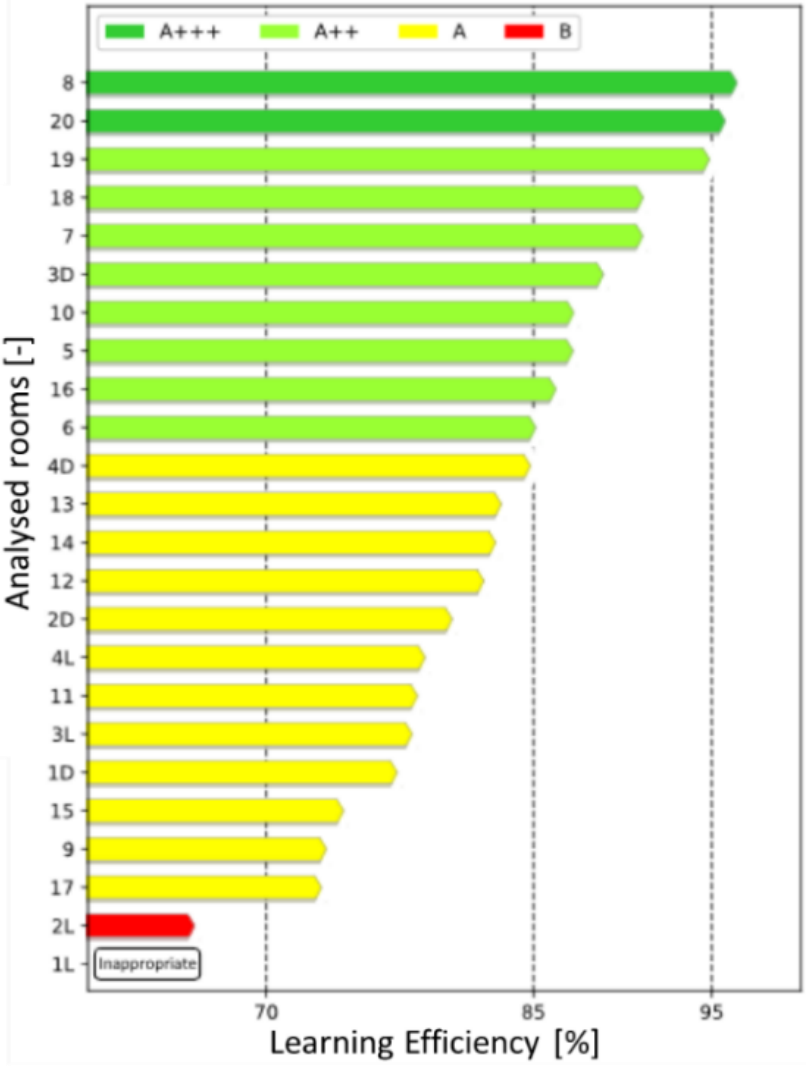

Source: Authors

4. CONCLUSIONS

A complete mapping of the impact of environmental stressors in 24 rooms of a teaching and innovation organization, with approximately 130 collaborators, was obtained by means of a semi-empirical mathematical model adjusted from experimental data. Through the experiments, it was possible to quantify the loss of knowledge flow (φ_s) and learning efficiency (η_l) in the environments analyzed by means of the method proposed in this study. The largest losses in knowledge flow were ~35%, which would culminate in an increase of nearly 3h in an 8h workday to accomplish the same task.

Analyzes have shown that both metrics employed are equivalent, although the loss in knowledge flow provides more detail than learning efficiency, this being a global indicator. Given the above, it is recommended that the method be employed to classify environments for learning efficiency and loss in the knowledge flow in order to make organizations more productive while contributing not only to user comfort but also to the learning process.

With regard to the limitations of the research, each occupant was assessed without distinction, disregarding any internal effects, on a personal level, such as stress and psychological and physical health. Although the present work was focused on a laboratory facility, the proposed method can be extended to various types of environment, such as classrooms, commercial and industrial offices, *coworking* environments, gyms, among others.

ACKNOWLEDGMENTS

The authors are grateful for the support of the IGTI (Center for Research in Intelligence, Management and Technology for Innovation) and POLO (Research Laboratories in Refrigeration and Thermophysics), both from the Federal University of Santa Catarina, Florianópolis, SC, Brazil.

REFERENCES

Ambrose, B. Building the business case: health, welfare and productivity in green offices, London, UK, Oct. 2016.

Anzanello, M. J. Learning curves as markers for the allocation of product models to workers' teams, Master's Dissertation, UFRGS, Porto Alegre, RS, Brazil, 2004.

Been, by I., and Beijer, M. The influence of office type on satisfaction and perceived productivity support, Journal of Facilities Management, vol. 12, no. 2, pp. 142-157, Apr. 2014, doi: 10.1108/JFM-02-2013-0011.

Fisk, W. J., Black, D., and Brunner, G., Changing ventilation rates in U.S. offices: Implications for health, work performance, energy, and associated economics, Build Environ, vol. 47, no. 1, pp. 368-372, doi: 10.1016/j.buildenv.2011.07.001, Jan. 2012.

Fisk, W. J., Health and productivity gains from better indoor environments and their relationship with building energy efficiency, Annu. Rev. Energy Environ, vol. 25, pp. 537-66, 2000, [Online]. Available: www.annualreviews.org.

Brasindoor Schools Forum, Brasindoor. Air care is as important as water, Available at: https://www.brasindoor.com.br/evento_forum_brasindoor_escolas.php. Accessed: 26 September 2024.

Green building council. Supporting occupant health means prioritizing indoor air quality, Available at: https://www.gbcbrasil.org.br/apoiar-a-saude-dos-ocupantes-significa-priorizar-a-qualidade-do-ar-interno/. Accessed: 24 September 2024.

Kamarulzaman, N., Saleh, A. A., Hashim, S. Z., Hashim, H. and Abdul-Ghani, A. A. An overview of the influence of physical office environments towards employees, Procedia Eng, vol. 20, pp. 262-268, doi: 10.1016/j.proeng.2011.11.164, 2011.

Lan, L., Wargocki, P., Wyon, D.P., and Lian, Z. Effects of thermal discomfort in an office on perceived air quality, SBS symptoms, physiological responses, and human performance, Indoor Air, vol. 21, no. 5, pp. 376-390, Oct. doi: 10.1111/j.1600-0668.2011.00714.x, 2.

Lee, J., Tae, Kim, W., Chansik, L., Koo, C., and Asce, A. M. Integrated Approach to Evaluating the Effect of Indoor CO 2 Concentration on Human Cognitive Performance and Neural Responses in Office Environment, 2021, doi: 10.1061/(ASCE)ME.1943.

Lippman, P. C., Architecture, J. and York, N. Can the physical environment have an impact on the learning environment?, 2010.

Lipczynska, A., Schiavon, S., Graham, L.T. Thermal comfort and self-reported productivity in an office with ceiling fans in the tropics, Build Environ, vol. 135, pp. 202-212, doi: 10.1016/j.buildenv.2018.03.013, May 2018.

Lorsch, H.G., and Abdou, O. A. The impact of the building indoor environment on occupant productivity—part 1: recent studies, measures, and costs, ASHRAE Transactions-American Society of Heating Refrigerating Airconditioning Engin, vol. 100, no. 2, pp. 741-749, 1994.

Satish, Usha *et al*. Is CO2 an indoor pollutant? direct effects of low-to-moderate CO2 concentrations on human decision-making performance, Environ Health Perspect, vol. 120, no. 12, pp. 1671-1677, 2012, doi: 10.1289/ehp.1104789.

Spengler, J.D., Samet, J.M., Mccarthy, J.F., Hill, M., and Fisk, W, J. Estimates of potential nationwide productivity and health benefits from better indoor environments: an update, in Indoor Air Quality Handbook, 2001st ed., J. D. Spengler, J. M. Samet, and J. F. McCarthy, Eds. McGraw-Hill Education, 2001.

CHAPTER 7

THE IMPACT OF COSMETIC PLASTIC SURGERY ON WOMEN

Bianka Vitaliano Zad
Graduated in Nursing
Institution: Universidade Paulista (UNIP)
Address: São Paulo, São Paulo, Brazil
E-mail: biankazad@gmail.com

Juliana Ferreira de Alencar
Graduated in Nursing
Institution: Centro Universitário Maurício de Nassau (UNINASSAU)
Address: Juazeiro do Norte, Ceará, Brazil
E-mail: juliana_senador@hotmail.com

Juliana Fogaça Maricato
Graduated in Nursing
Institution: Centro Universitário Luterano de Palmas
Address: Palmas, Tocantins, Brazil
E-mail: jufogacamaricato@gmail.com

Gislaine Alves da Silva
Graduated in Nursing
Institution: Universidade Regional de Blumenau (FURB)
Address: Blumenau, Santa Catarina, Brazil
E-mail: gienfcuidado@gmail.com

Kaline Silva Meneses
Graduated in Nursing
Institution: Centro Universitário Dom Pedro II
Address: Salvador, Bahia, Brazil
E-mail: kalinesilvameneses@hotmail.com

ABSTRACT: Plastic surgery can have several purposes, such as restoring a part of the body, or reestablishing the function and shape of parts of the body affected by acquired or congenital problems. Cosmetic plastic surgery models parts of the body with the aim of improving self-esteem and beauty. Therefore, this study will address the impact that cosmetic plastic surgeries have on women's self-esteem. This is an integrative literature review that consists of critical summaries of a given topic with relevance to the research area, to synthesize previous research in order to understand and suggest improvements on a given subject. The most sought-after cosmetic procedures by women arise from dissatisfaction with their own bodies, which can be linked to pregnancy, excess fat and excess abdominal skin, which affects self-esteem, among other factors. Since these are procedures that achieve the desired result in a

short time, they generate satisfaction with appearance, which improves self-image and provides feelings of happiness. Given the facts exposed and analyzed, cosmetic plastic surgery influences women's self-esteem and social relationships.

KEYWORDS: esthetics, self concept, surgery plastic.

RESUMO: A cirurgia plástica pode ter várias finalidades, como por exemplo restaurar alguma parte do corpo, ou reestabelecer a função e forma de partes do corpo afetados por problemas adquiridos ou congênito. A cirurgia plástica estética modela partes do corpo com o objetivo de melhorar a autoestima e beleza. Sendo assim, esse estudo irá abordar o impacto que as cirurgias plásticas estéticas tem na autoestima da mulher. Trata-se de uma revisão integrativa da literatura que consiste em resumos críticos de determinado tema com relevância na área de pesquisa, para sintetizar pesquisas anteriores a fim de conhecer e sugerir melhorias sobre determinado assunto. Os procedimentos estéticos mais procurados pelas mulheres nascem da insatisfação com o próprio corpo, que podem ser atrelados a gravidez, excesso de gordura e excesso de pele abdominal, o que afeta dentre outros fatores, a autoestima. Por se tratar de procedimentos que se obtém o resultado desejado em pouco tempo, gera satisfação com a aparência, o que melhora a autoimagem e proporciona sentimentos de felicidade. Dado os fatos expostos e analisados, a cirurgia plástica estética influencia a autoestima da mulher e relações sociais.

PALAVRAS-CHAVE: estética, autoimagem, cirurgia plástica.

1 INTRODUCTION

Plastic surgery can have various purposes, such as restoring some part of the body, or re-establishing the function and shape of parts of the body affected by acquired or congenital problems. Aesthetic plastic surgery shapes parts of the body with the aim of improving self-esteem and beauty. According to the International Society of Aesthetic Plastic Surgery (ISAPS), in Brazil the most performed aesthetic surgical procedures in 2019 were liposuction, breast augmentation, abdominoplasty, eyelid surgery and buttock augmentation (Correa, Sousa and Oliveira, 2021).

The first reports of plastic surgery date back to antiquity, practiced over 4000 years ago. Techniques advanced during the First World War, when soldiers with serious wounds needed to recover, and techniques have been perfected up to the present day. Brazil leads the world in the number of cosmetic procedures, with approximately 1.5 million plastic surgeries performed in 2019, according to the International Society for Aesthetic Plastic Surgery. There was also an increase in the number of doctors specializing in plastic surgery between 2016 and 2018, as well as an 18.3% increase in the total number of surgical procedures in Brazil over the same period (Gomes *et al*., 2021).

The “perfect” standard of beauty is something that contemporary society is under a lot of pressure to achieve, and the media, mainly through advertisements, bring models with standards demanded by society, thus influencing individuals to seek external change in order to fit in. However, cosmetic plastic surgery can also contribute to rehabilitation and restore a woman's self-esteem, while also promoting quality of life, such as breast reconstruction surgery, giving women back their physical and psychological integrity. Research has shown that breast reconstruction surgery improves women's self-esteem and their relationship with their partner (Marinho, 2022; Vaz *et al*., 2023; Lima, Gasparin, Gregório, 2024).

Therefore, this study will address the impact that cosmetic plastic surgery has on women's self-esteem.

2. METHODOLOGY

This is an integrative literature review that consists of critical summaries of a given topic with relevance in the research area, to synthesize previous research in order to learn about and suggest improvements on a given subject. This type of review follows a number of steps: choosing the topic and formulating the guiding question, collecting data or defining the literature search, evaluating the data, analyzing the data and presenting and interpreting the results (Crossetti, 2012).

The research was carried out between April and May 2024, in the Scientific Electronic Library Online (SCIELO) virtual library and in the following databases: Online Medical Literature Search and Analysis System (MEDLINE), Latin American and Caribbean Health Sciences Literature (LILACS) due to the credibility, variety and ease of finding articles in Portuguese and available in full for online access, using the Health Sciences Descriptors (DeCS): “Aesthetics”, “Self-image” and “Plastic Surgery”. The following inclusion criteria were used: original articles in Portuguese, Spanish and English that fit the proposed theme and studies published between 2018 and 2024, in order to find the most recent studies on the subject. The exclusion criteria were: letter to the reader, articles unrelated to the subject of this study, review articles and duplicates.

Fifty articles were found, of which 20 were excluded after reading the title. Of the remaining 30, 6 were excluded after reading the abstract, 5 because they were theses and dissertations, 7 did not answer the research problem, 5 were excluded because of the type of methodology, and in the end the reviewers decided to include 7 articles. In order to show the sample of this research, a table was made of the 7 articles selected, with the main relevant information.

Table 1. Sample of selected articles

Título	Autor/Ano	Tipo de Estudo	Conclusão
Aesthetic plastic surgery in women and self-esteem: a qualitative study	AGUIAR, K. G. M., & SOUSA, J. A., 2023	Cross-sectional, qualitative and exploratory study.	Plastic surgery improves the perception of self-esteem, but it was not the determining factor for the participants to undergo the surgical procedure.
Evaluation of the interest of women assisted by the Rio do Sul Women's Care Center in intimate cosmetic surgeries	FRITSCHE, E., *et al*., 2022.	Cross-sectional observational study.	Intimate aesthetics generate physical, psychosocial, sexual and daily interference, with an important impact on the quality of life of these people.
Quality of life and self-esteem in elderly women undergoing and not undergoing cosmetic surgery	SPADONI-PACHECO, L. M., CARVALHO, G. A., 2018.	A descriptive, case-control study,	When analyzing the elderly women who underwent cosmetic surgery, high levels of personal satisfaction and social life were demonstrated.
Quality of life and aesthetic results after mastectomy and breast reconstruction	CAMMAROTA, M. C., *et al*., 2021.	A retrospective longitudinal observational study using a review of patient records.	The quality of life of patients after breast reconstruction with breast implants is higher than before the surgical procedure.
The impact of cosmetic mammoplasty on the self-esteem of women in a northeastern capital.	SANTOS, G. R., *et al*., 2019.	A prospective, longitudinal, analytical, qualitative and quantitative study of 40 patients undergoing primary aesthetic mammoplasty.	There was an average increase in the self-esteem of patients who underwent mammoplasty and the three types of surgery produced the same results in terms of changes in self-esteem.
Relationship between Aesthetic Procedures and Satisfaction with Body Self-Image and Self-Esteem in Women	PINHEIRO, T., PIOVEZAN, N., BATISTA, H., MUNER, L., 2020.	Qualitative research.	The study identified a positive and significant association between self-esteem and satisfaction with body image, so that the more satisfied women are with their weight, the higher their levels of self-esteem tend to be.
Contributions of aesthetics to quality of life	CARVALHO, M. L., FIGUEIREDO F. C., 2020.	Qualitative research.	Quality of life is proving to be an important parameter to be considered in people's way of life, and its scope has already reached the interdisciplinary level, so that knowledge about the problems faced in people's day-to-day lives is present based on their perception.

Fonte: Elaborado pelas autoras

3. DISCUSSION

The aesthetic procedures most sought after by women stem from dissatisfaction with their own bodies, which can be linked to pregnancy, excess fat and excess abdominal skin, which affects self-esteem, among other factors. As these are

procedures that achieve the desired result in a short space of time, they generate satisfaction with one's appearance, which improves one's self-image and provides feelings of happiness. Although human beings always seek to adapt to live in society, there is also a search for personal satisfaction, and plastic surgery has helped by providing positive effects when it comes to self-esteem (Aguiar and Sousa, 2023).

When it comes to surgical procedures for aesthetic purposes, the first types of surgery that come to mind are those mentioned above. However, according to the American Society for Aesthetic Plastic Surgery, female vulvar and vaginal plastic surgery procedures have been on the rise in recent years and are practiced by more than 25% of plastic surgeons. The reason why women seek this type of surgery is embarrassment about their intimate aesthetics, usually related to wearing bikinis, panties and leggings. Women's sociability is intrinsically linked to their self-esteem and is therefore an extremely important factor (Fritsche and Mendes, 2022).

A study carried out in 2018 with elderly patients who had undergone a cosmetic procedure found that in addition to dissatisfaction with their own image, social relationships were a factor that motivated patients to have surgery. This study shows that plastic surgery influences women's sociability, making them feel confident and self-assured. In the same study, it was noted that there was a slight difference in the increase in self-esteem of patients who had undergone surgery when compared to patients who had not undergone an aesthetic procedure (Spadoni-Pacheco and Carvaho, 2018).

Breast plastic surgery for women who have had breast cancer and need breast reconstruction, for example, has achieved positive results for women's psychosocial health. In addition, it improves sexuality, self-image and reduces depression rates, showing that aesthetics can positively alter women's psychology, leaving them satisfied with the result, restoring self-esteem and promoting quality of life (Cammarota *et al*., 2019).

A study carried out in private plastic surgery clinics located in Aracajú showed that more than half of the patients were satisfied with the result of their surgery. The study also used the Rosenberg Self-Esteem Scale in the post-surgery period, and as a result, patients who had low self-esteem moved to medium to high self-esteem, with an overall increase of 13.3% in the self-esteem of patients who underwent cosmetic

mammoplasty. In addition, for 74.4% of patients, the surgery had a positive influence on their social life in different ways (Santos *et al*., 2019; Carvalho and Figueiredo, 2020).

Another survey of 120 women aged between 18 and 60 to verify the relationship between cosmetic procedures and the degree of satisfaction and self-esteem of women revealed that there is an association between self-esteem and satisfaction with body image. The more satisfied women are with their weight, the higher their level of self-esteem. Another interesting point is that the study participants who said they were not influenced by the opinions of others had a higher level of self-esteem. This result suggests that negative body image is associated with low levels of self-esteem and may indicate a psychological disorder, making it important to have a thorough medical assessment before any procedure (Pinheiro *et al*., 2020; Santos *et al*., 2019).

4. CONCLUSION

Given the facts exposed and analyzed, cosmetic plastic surgery influences women's self-esteem and social relationships. The findings of this study do not encourage or discriminate against plastic surgery, but aim to demonstrate that when performed in a controlled environment and with trained professionals, the results in women's lives are generally positive.

In addition, it was possible to observe that the field of aesthetics is constantly expanding, which requires trained and up-to-date professionals to offer a quality service, reducing possible risks and complications.

REFERENCES

AGUIAR, K. G. M., & SOUSA, J. A. Cirurgia plástica estética em mulheres e autoestima: um estudo qualitativo. **Revista Psicologia, Diversidade e Saúde**, v. 12, 2023. Disponível em: http://dx.doi.org/10.17267/2317-3394rpds.2023.e5277. Acesso em: 01 jun. 2024.

CAMMAROTA, M. C., *et al*. Qualidade de vida e resultado estético após mastectomia e reconstrução mamária. **Rev. Bras. Cir. Plást**., v. 34, n. 1, p. 45-57, 2019. Disponível em: https://www.scielo.br/j/rbcp/a/CZnWMnZn4zwY8dW7yxbcYtR/?format=pdf&lang=pt. Acesso em: 01 jun. 2024.

CARVALHO, M. L., FIGUEIREDO, F. C. Contribuições da estética para a qualidade de vida. **Braz. J. of Develop**., v. 6, n. 6, p.39459-39473, 2020. Disponível em: https://ojs.brazilianjournals.com.br/ojs/index.php/BRJD/article/view/11979/10023. Acesso em: 20 jun. 2024.

CORREA, L. N.; SOUSA, E. B.; OLIVEIRA, N. P. C. O uso do taping no pós-operatório de cirurgia plástica. **Research, Society and Development**, v. 10, n.15, 2021. Disponível em: https://rsdjournal.org/index.php/rsd/article/view/22868/19942. Acesso em: 1 jun 2024.

CROSSETTI, M.G.O. Revisão integrativa de pesquisa na enfermagem o rigor cientifico que lhe é exigido [editorial]. **Rev Gaúcha Enfermagem**, v. 33, n. 2, p.8-9, 2012.

FRITSCHE, E., *et al*. Avaliação do interesse das mulheres assistidas pelo centro de atenção à mulher de Rio do Sul em cirurgias estéticas íntimas. **Rev. Bras. Cir. Plást**., v. 37, n. 3, p. 326-331,2022. Disponível em: https://www.scielo.br/j/rbcp/a/VzMRxnXH76wWNYbNSKzY5mG/?format=pdf&lang=pt. Acesso em: 1 jun. 2024.

GOMES, O. S., *et al*. Cirurgia plástica no Brasil: uma análise epidemiológica. **Revista Eletrônica Acervo Científico**, v. 24, p. e73752021, 2021. Disponível em: https://doi.org/10.25248/reac.e7375.2021. Acesso em: 1 jun 2024.

LIMA, B. C. M., GASPARIN, C. C., GREGÓRIO, P. C. Procedimentos Estéticos: uma Abordagem Psicológica. **Brazilian Journal of Implantology and Health Sciences**, v. 6, n. 3, p. 2601-2626, 2024. Disponível em: https://bjihs.emnuvens.com.br/bjihs/article/view/1766/1991. Acesso em: 1 jun. 2024.

MARINHO, D. S. A influência dos padrões de beleza socialmente impostos na autoestima das mulheres. **Repositório Institucional Unicambury**, v.1, n.1, 2021. Disponível em: https://www.revistaleiacambury.com.br/index.php/repositorio/article/view/47/46. Aceso em: 01 jun 2024.

PINHEIRO, T., PIOVEZAN, N., BATISTA, H., MUNER, L. Relação dos Procedimentos Estéticos com Satisfação da Autoimagem Corporal e Autoestima de Mulheres. **Revista Cathedral**, v.2, n.1, 2020. Disponível em: http://cathedral.ojs.galoa.com.br/index.php/cathedral/article/view/106. Acesso em: 1 jun. 2024.

SANTOS, G. R., *et al*. Impacto da mamoplastia estética na autoestima de mulheres de uma capital nordestina. **Rev. Bras. Cir. Plást**., v. 34, n. 1, p. 58-64, 2019. Disponível em: https://www.scielo.br/j/rbcp/a/Z48XJp8x5cjTFR3YFK37CkC/?format=pdf&lang=pt. Acesso em: 1 jun 2024.

SPADONI-PACHECO, L. M., CARVALHO, G. A. Qualidade de vida e autoestima em idosas submetidas e não submetidas à cirurgia estética. **Rev. Bras. Cir. Plást**., v. 33, n. 4, p. 528-535, 2018. Disponível em: https://www.scielo.br/j/rbcp/a/MqX3WN4SC97kMwhMtJKfj6j/?format=pdf&lang=pt. Acesso em: 1 jun 2024.

VAZ, S. R., *et al*. Cirurgia Plástica e a Autoestima: Uma Análise do Impacto de Cirurgias Estéticas sobre a Autoimagem do Paciente. **Revista Ibero-Americana de Humanidades, Ciências e Educação**, v.1, n.01. jun, [Edição Especial], 2023. Disponível em: https://periodicorease.pro.br/rease/article/view/10506/4307. Acesso em: 1 jun 2024.

Agência Brasileira ISBN
ISBN: 978-65-6016-072-9